A search for periodic low-energy gamma-ray emission from pulsar PSR0531+21

Kevin Kam Ching Yau

A SEARCH FOR PERIODIC LOW-ENERGY GAMMA-RAY EMISSION FROM PULSAR PSR0531+21

BY

KEVIN KAM CHING YAU

A THESIS SUBMITTED TO

THE UNIVERSITY OF DURHAM

FOR THE DEGREE OF

MASTER OF SCIENCE

FEBRUARY 1984

To my parents

A search for Periodic Low-energy Gamma-ray Emission from Pulsar PSR0531+21

ABSTRACT

The observation on 6th June 1981 of the Crab Nebula by the Durham high resolution low-energy gamma-ray spectrometer has produced evidence for line features at energies of 404.4 keV and 1049.6 keV with intensities at the top of the atmosphere of $(7.2 \pm 2.1) \times 10^{-3}$ and $(1.9 \pm 0.4) \times 10^{-3}$ photons cm^{-2} s^{-1} respectively. A transient line feature at 78.9 keV has also been detected. This thesis reports on a search for low-energy gamma-ray pulsed emission from the Crab pulsar which has yielded positive results. The period of the Crab pulsar has been correctly determined and its light curve deconvolved. The results on the Crab pulsar spectral analysis agree with a power law $\sim E^{-2.2}$. No evidence has been found for pulsed line emission from the Crab pulsar.

CONTENTS

LIST OF FIGURES

N.B. (The page number given is referred to the page number of the text immediately before the figure)

LIST OF TABLES

N.B. (The page number given is referred to the page number of the text immediately before the table)

LIST OF SYMBOLS

Unless otherwise stated the symbols used in this thesis carry the following interpretations.

A_{Eff}	Effective area of the telescope
B	Magnetic field
B_o	Surface magnetic field strength
c	Velocity of light $2.997924562 \times 10^{8}\ ms^{-1}$
dp/dr	Pressure gradient
e	Eccentricity
E	Electric field, energy of a particle
$E_{\|\|}$	Component of electric field parallel to the magnetic field
f	Flattening of the Earth
f	Ratio of 'time on' to 'time off' $=T_{on}/T_{off}$,
G	Gravitational constant
h	Scale height, height
I	Moment of inertia
k	Boltzmann's constant $1.38062 \times 10^{-23}\ JK^{-1}$
l	Mean anomally
ly	Light year
m	Magnetic-dipole moment
m_H	Mass of Hydrogen
m(r)	Mass within radius r
M	Mass of a neutron star
$M_\odot$	Solar mass
n	Number of bins
n_e	Charge number density
n_p	Number of periods in the total observation interval
$\hat{n}$	A unit vector

N_{on}	Number of 'on source' counts
N_{off}	Number of 'off source' counts
$\langle N \rangle$	Expected number of counts per bin
P	Period
$\dot{P}$	Period first derivative
$\ddot{P}$	Period second derivative
Pr	Probability
P(r)	Pressure at r
POS	Position of an event within a frame
PSR	Pulsar Clock
r	Radius
R	Radius of neutron star
$\underline{R}$	Vector from Solar System Barycentre to balloon
R_L	Radius of the light-cylinder
R_P	Radius of polar cap region
S	Significance of a feature
$S\Omega$	Spectrometer acceptance factor
t_B	Arrival time at the Barycentre
t_b	Arrival time at the balloon
t_r	Recorded arrival time at the ground receiving station
T	Absolute temperature
T_F	Time recorded at the start of a frame
T_{Obs}	Total observation period
T_{on}	Time on
T_{off}	Time off
x,y,z	Geocentric rectangular coordinates
w	Width
α	Angle between the magnetic and rotation axes
α	Right ascension

β	v/c, duty cycle
γ	Lorentz factor $(1-\beta^2)^{-1/2}$
δ	Declination
δP	Error on P
ΔP	Range of scanning for the period
Δt	Photon arrival times correction term
Δt_{rel}	Correction term due to relativistic effects
$\Delta\varphi$	Potential difference
θ	Angle between rotation axis and field line
θ	Angle between source direction and telescope axis
θ_{FWHM}	Acceptance angle at full width half maximum
θ_M	Maximum angle off the telescope axis
θ_p	Angular distance from the pole
λ	Longitude, wavelength
ν	Number of degrees of freedom
ρ_c	Radius of curvature of a magnetic field line
ρ_e	Charge density
$\rho(r)$	Density at r
σ	Sigma (standard deviation)
σ^2	Variance
τ	Magnetic torque
φ	Latitude
φ	Quadrupolar electrostatic potential
Φ	Pulsar phase
χ^2	Chi-square
ω_c	Angular characteristic frequency
Ω	Rotation frequency
$\underline{\Omega}$	Vector angular velocity

CHAPTER 1

INTRODUCTION

1.1 The Discovery Of Pulsars

The discovery of pulsars, together with the 3°K microwave background radiation and the quasars certainly would rank as three of the most exciting astronomical phenomena discovered in the last two decades. As with many significant discoveries the first detection of pulsars was rather fortuitous. In 1964, Cambridge radio astronomers had found that certain compact radio sources (those with an angular diameter less than a second of arc), exhibited rapid fluctuations in intensity. These variations of compact radio sources known as 'scintillations' were thought to have been due to the scattering of radio waves by irregularities in the solar wind. In order to study this new phenomenon, a large radio telescope was specially designed by the Cambridge radio astronomy group under the direction of Hewish. (Ref. 1) The telescope is a rectangular array containing 2,Ø48 full-wave dipoles operating at 81.5 MHz (λ=3.7m) and covering nearly five acres of land. As the object of the search was to detect scintillations, a short response time and a repetitive observing routine were employed. Neither of these features were used in the earlier surveys with radio telescopes of comparable sensitivity, otherwise

pulsars might have been discovered a few years earlier. Since rapid fluctuations in the signals from any celestial source were not expected the receivers and recording devices of earlier surveys were usually adjusted with time constants of several seconds to smooth random noise fluctuations.

Soon after the observation began in July 1967, Hewish's research student, Jocelyn Bell noted some strange, sporadic, signals in the survey records. At first, they could not convince themselves that these signals were emitted from a naturally ocurring astronomical object. After readjusting the recorder to accept a much faster response time, on November 28, 1967, regular pulses showing periodicity of 1.3377295s were confirmed. This was the first pulsar to be discovered, and was designated CP 1919 meaning 'Cambridge Pulsar at right ascension 19h19m'. The survey records revealed three other similar sources it thus became clear that the sources had to be natural phenomena. These new findings were published in a February issue of Nature in 1968 (Hewish et al. 1968). The enormous impact of this discovery resulted in an unprecedented burst of astronomical activity in the following months. During this time, the properties of pulsars were elaborated in detail, many more examples were discovered and finally their nature as rotating, magnetised neutron stars was firmly established.

1.2 Theoretical Status

1.2.1 The Structure Of Neutron Stars -

The concept of a neutron star was first discussed by Baade and Zwicky in 1934 and model calculations giving the structure of such an object were first made by Oppenheimer and Volkoff (1939). The basic idea behind these models is that the infalling mass due to gravitational attraction is balanced by the pressure created by neutron degeneracy. Neutron star models are computed by integrating the general-relativistic equation of hydrostatic balance (the Tolman-Oppenheimer-Volkoff equation):

$$-\frac{dp}{dr} = \frac{[G(\rho(r)) + P(r)/c^2]\ [m(r) + 4\pi r^3 P(r)/c^2]}{r^2[1-2Gm(r)/rc^2]} \qquad (1.1)$$

where $m(r)$ is the mass within radius r, $P(r)$ and $\rho(r)$ are the pressure and density respectively at r.

This equation shows that in the case of general relativity the pressure contributes to the effective mass-density hence the gradient of pressure dP/dr is greater than in nonrelativistic cases. The parameters $P(r)$ and $\rho(r)$ are related by the equation of state, which must be known or estimated for the different density regions of the star. At subnuclear densities the equation of state is fairly well known, but there is considerable uncertainty at high densities. Since the equation of state determines the mass upper limits of neutron stars, so it is important to know

the correct form of this equation. By requiring that the equation of state does not violate causality, Rhoades and Ruffini (1974) have placed a firm upper limit (within general relativity) of 3.2 $M_{\odot}$ on the mass of neutron stars. A schematic illustration of the structure of a 1.33 $M_{\odot}$ neutron star is shown together with its various predicted constituents in Figure 1.1.

1.2.2 Pulsar Magnetosphere -

Having briefly discussed the internal structure of the neutron star the magnetosphere, the region immediately surrounding the star, will now be considered. All the electrodynamic processes and emission mechanisms are predicted to occur in this region. It is almost certain that the neutron stars we observe as pulsars possess extremely strong magnetic fields which are thought to be the strongest anywhere in the universe. Calculations based on the rate of loss of rotational kinetic energy suggest that the surface magnetic fields of most pulsars are of the order 10^{12} G. Ruderman and Sutherland (1973) suggest that turbulent convection in the core of pre-supernova stars results in the field building up to an equipartition value of $\sim 3 \times 10^{9}$ G. Conservation of flux during the collapse to a neutron star then results in a surface field strength $\sim 4 \times 10^{12}$ G.

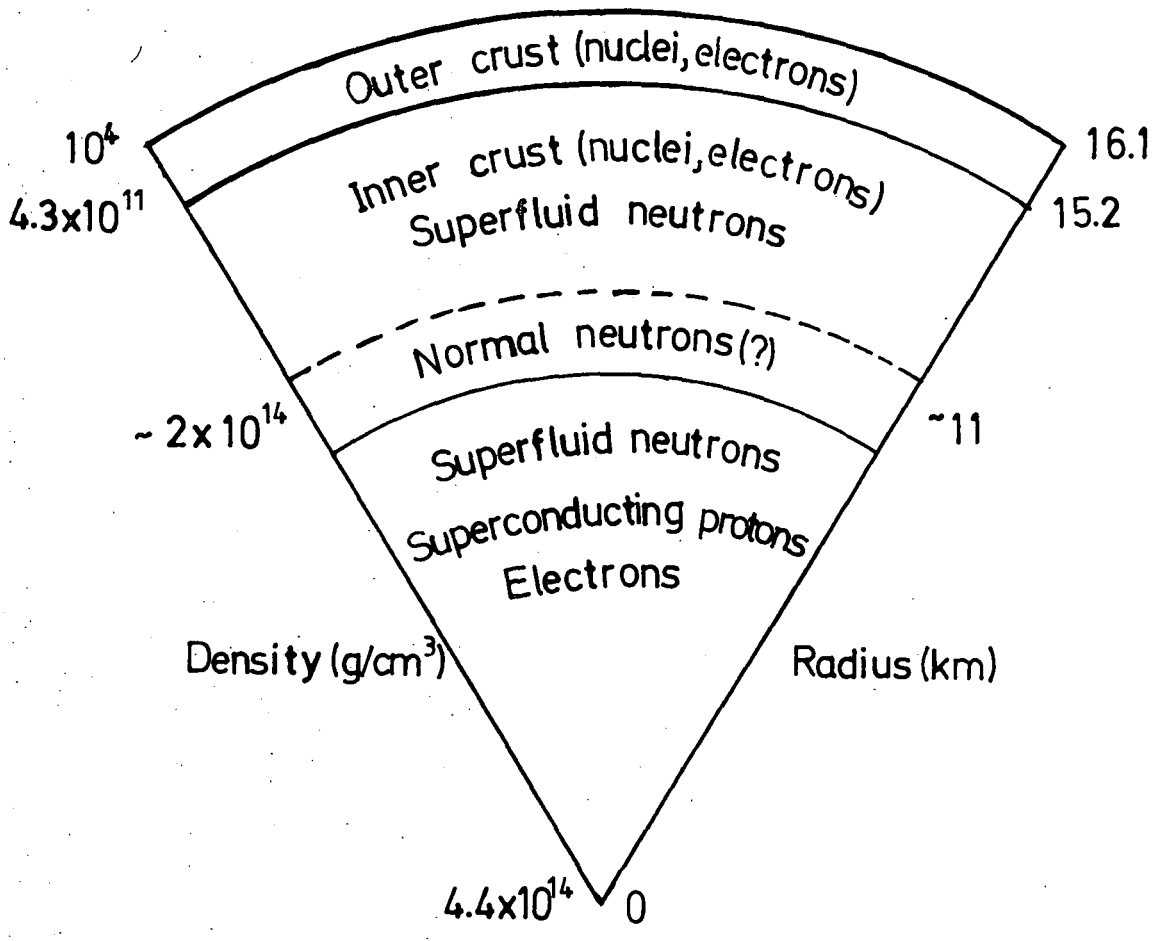

Figure 1.1 Cross-section of a neutron star having a gravitational mass of 1.33 $M_\odot$ (After Pandharipande et al. 1976)

Since all the radiation processes are in this region, therefore it is of vital importance that we understand the configuration and state of the plasma in the magnetosphere of the star. Before pulsars were discovered theorists did not expect that there would be an atmosphere on neutron stars as any atmosphere present would be condensed onto the surface. A normal atmosphere under gravitational equilibrium would have a scale height, given by

$$h = \frac{kTr^2}{GMm_H} \qquad (1.2)$$

where M is the neutron star mass with a radius r and m_H is the mass of a hydrogen atom. For a temperature of 10^6 K, the scale height is about 1 cm. The situation was completely changed with the suggestion of Pacini (1967) that there might be a very strong magnetic field associated with neutron stars which were rotating rapidly such that the Lorentz force created by this field would overwhelm the gravity by many orders of magnitude. Pacini considers an ideal situation in which a magnetic dipole is rotating very rapidly perpendicular to the rotation axis. In this way the dipole radiates significant amounts of energy in the form of electromagnetic waves - magnetic dipole radiation - at the rotation frequency. The radiation reaction torque transmitted to the star by the magnetic field is

$$\tau = - \frac{2(m\sin\alpha)^2}{3c^3} \Omega^3 \qquad (1.3)$$

where m is the magnetic-dipole moment, and α is the angle between the magnetic and rotation axes. Since $m \sim B_o R^3$, where B_o is the surface field strength and R is the radius of the star, the magnitude of the surface magnetic field can then be obtained once we know the period and period derivative (assuming $\sin\alpha$ equal to one) from

$$B_o \simeq \left(\frac{3Ic^3 P\dot{P}}{8\pi^2 R^6}\right)^{1/2} \qquad (1.4)$$

where I is the moment of inertia of the rotating system. Putting in a typical set of parameters for a neutron star ($I=10^{45}$ gcm^2, $R=10^6$ cm, P in s and $\dot{P}$ in ss^{-1}) we have :

$$B_o \simeq 3.2 \times 10^{19} (P\dot{P})^{1/2} \quad G$$

For the Crab pulsar, $P \sim 0.033$ s and $\dot{P} \sim 4.2\times10^{-13}$ ss^{-1}, the magnetic field would be $B_o \simeq 3.8\times10^{12}$G.

So far, we have only considered an ideal situation in which a conducting sphere is surrounded by a vacuum, but the region can not be a vacuum because of these strong fields. Besides, one may have doubts about the life-time of such a strong field, as it may decay through ohmic dissipation in a lifetime short compared with that of pulsars. These problems were solved in a classic paper by Goldreich and Julian (1969). In which they argued that there existed an electrically generated magnetosphere containing charged particles and the conductivity of neutron star material is extremely high and may be assumed infinite. The spinning of the neutron star in the presence of a strong magnetic field

induces an electric field of a substantial strength, hence within the star (provided particle inertia is neglected):

$$\underline{E} + \frac{1}{c} (\underline{\Omega} x \underline{r}) x \underline{B} = \emptyset \qquad (1.5)$$

where $\underline{E}$ and $\underline{B}$ are the electric and magnetic fields and $\underline{\Omega}$ is the vector angular velocity of the star. The presence of this field requires a redistribution of the charge within the star such that

$$\rho_e = \frac{1}{4\pi} \nabla . \underline{E} = - \frac{1}{2\pi c} \underline{\Omega} . \underline{B} \qquad (1.6)$$

which gives a charge number density $n_e = 7 \times 10^{-2} \; B_z P^{-1} \; cm^{-3}$, where B_z is the component of $\underline{B}$ parallel to $\underline{\Omega}$.

If we have static vacuum magnetospheric fields surrounding the star. Then using Laplace's equation, together with boundary conditions at the stellar surface (r=R) will give a quadrupolar electrostatic potential

$$\varphi = - \frac{B_o \Omega R^5}{6cr^3} (3\cos^2 \theta - 1) \qquad (1.7)$$

where θ is the angle from the rotation axis.
The electric field corresponding to this potential has non-zero $\underline{E}.\underline{B}$, the value at the stellar surface being

$$(\underline{E}.\underline{B})_R = - \frac{\Omega R}{c} B_o^2 \cos^3 \theta \qquad (1.8)$$

Hence the magnitude of the electric field parallel to the

magnetic field at the surface is

$$E_{||} \simeq \frac{\Omega R}{c} B_o \simeq 6 \times 10^{10} P^{-1} \quad (\mathrm{Vcm}^{-1}) \qquad (1.9)$$

for $B_o = 10^{12}$ G and P in seconds.

Fields of this magnitude give both electrons and ions an acceleration exceeding that of gravity by many orders of magnitude. The normal factors determining the scale height are therefore completely dominated by electromagnetic effects, and provided the surface binding energies are not too large, charge will flow from the star to fill the surrounding region. If the particle inertia is neglected, the above equations (1.5) and (1.6) will apply to the plasma-filled magnetosphere, hence the parallel components of the electric field will be zero i.e. $\underline{E}.\underline{B}=0$.

Due to the strong magnetic field, charged particles are forced to co-rotate with the star and locked firmly to it by the magnetic field. The electrodynamic condition for this locking is that the Alfven velocity is less than the co-rotation velocity $\underline{\Omega}x\underline{r}$, if this were not so there would be an instability and the field pattern would be destroyed. However, this does not seem to be an important restriction as rotation can continue until the tangential velocity equals the velocity of light. This surface where $\underline{\Omega}x\underline{r}$ reaches c is a cylinder, known as the light cylinder, which has a radius

$$R_L = c/\Omega \simeq 5 \times 10^9 P \ (\mathrm{cm}) \qquad (1.10)$$

where P is in seconds.

The Goldreich-Julian model of the pulsar magnetosphere is illustrated in Figure 1.2. There are two distinct regions : the open field-lines that leave the star near the poles and penetrate the light cylinder which do not co-rotate with the star and the closed field-lines that do not penetrate the light cylinder which rotate with the star.

The closed field lines are those which originate on the surface beyond an angular distance θ_p of the poles, given by

$$\sin\theta_p = \left(\frac{\Omega R}{c}\right)^{1/2} \qquad (1.11)$$

Therefore, the radius of the polar cap region containing the open field-lines is

$$R_p \simeq R \sin\theta_p = R(\Omega R/c)^{1/2} \qquad (1.12)$$

The zone from which particles may leave the magnetosphere is known as the 'wind zone'. The trajectory of charged particles follow the open field lines until they approach the light cylinder.

Since the magnetic and rotation axes are parallel, the potential at the base of the field-lines near the axis will be negative with respect to the stellar environment, so electrons will stream from the star along these lines. At some critical field-line, the potential at the stellar surface will be equal to the exterior potential; in the annular region between the critical field-line and the last

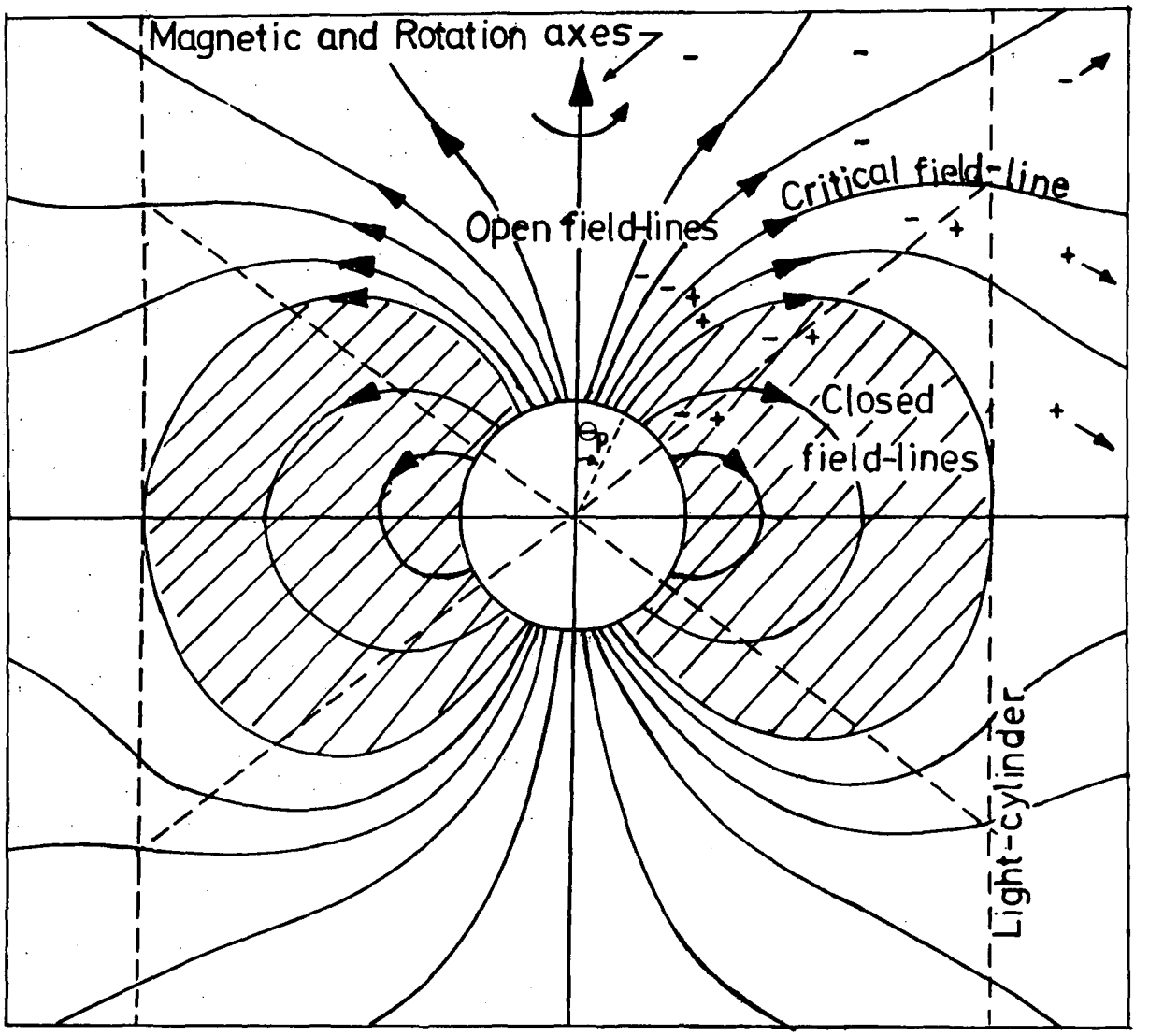

Figure 1.2 The magnetosphere of a pulsar with parallel magnetic and rotation axes. (Partly adapted from Goldreich and Julian, 1969)

open field line at θ_p it will be positive, so protons (ions) will stream from this region. The location of the critical field-line is determined by the condition that there be no net charge flow from the star. From equations (1.7) and (1.12) the potential difference between the centre and edge of the polar cap is

$$\Delta\varphi \simeq \frac{1}{2}\left(\frac{\Omega R}{c}\right)^2 RB_o \qquad (1.13)$$

For $B_o \simeq 10^{12}$ G and P in seconds, $\Delta\varphi \simeq 6\times10^{12} P^{-2}$ V

Although the field-lines are equipotential near the star, most of this potential must become available either near or beyond the light cylinder to accelerate charges along the open field-lines. Consequently, particle energies of ~ $6 \times 10^{12} P^{-2}$ eV are expected, comparable to those expected from acceleration by magnetic dipole radiation.

Goldreich and Julian consider only a simplified system (an aligned or axisymmetric rotator). But in the real situation pulsars must have an oblique rotator system i.e. with non-axisymmetric field, otherwise periodic pulsations will not be observed. Furthermore, their model does not give a self-consistent description of the currents and fields surrounding the star; also there is ambiguity of charge flow of one sign through regions of space with charge of the opposite sign.

The extreme case of an oblique rotator is one that rotates with its magnetic axis perpendicular to the rotation axis. In this case the assumption made by Goldreich and Julian that charges flow from the surface of the star to fill the magnetosphere is still valid. But in the closed field line regions where the streaming current is zero, Henriksen and Norton (1975) found that the field-lines form cusp-like neutral points near the light cylinder, as shown in Figure 1.3. Michel (1973a) found earlier that these neutral points formed a circle on the surface of the light cylinder centred on the magnetic axis. The charge accumulates at these neutral points and is ejected across the light cylinder. The shape of the open field-line regions is modified by the streaming currents as in the case of the aligned rotator. Henriksen and Norton are able to find a set of solutions to the force free equations that relate the field structures in the zone near the star, the light cylinder region and the wave zone far from the star. The two regions of particle acceleration they find are: the 'sling' region inside the light cylinder and the 'surfing' region in the wave zone. The major problem with the orthogonal rotator model is the absence of electrostatic acceleration of particles along the magnetic field lines because there is no component of the electric field parallel to the magnetic field, which is unlikely in real pulsar magnetospheres.

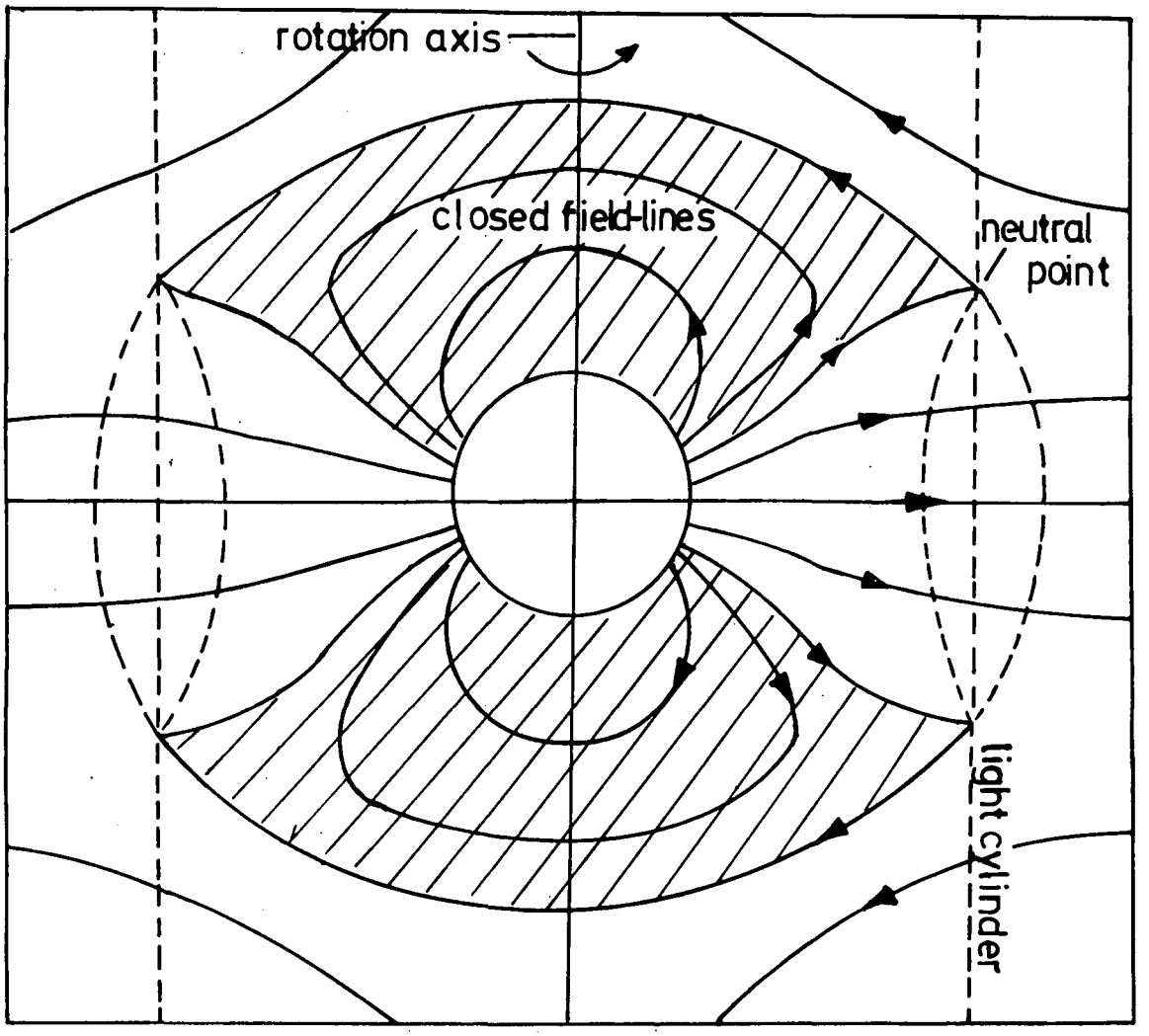

Figure 1.3 The magnetosphere of a pulsar with its magnetic axis perpendicular to the rotation axis.

The last configuration of the pulsar magnetosphere to be considered is for a magnetic monopole. Michel (1973b) has shown that, for a magnetic monopole, field-lines that remain radial in the meridian plane and form Archimedean spirals in the equatorial plane (Figure 1.4a,b) are an exact solution of the equation of motion with the assumption of massless magnetospheric particles. In this case, the outflow velocity is everywhere c and there is no co-rotation. The problem with this model is that the flow is charge separated and instability in the fully charged-separated plasma may occur. Also the effects of particle inertia have been neglected as a first approximation, so $\underline{E}.\underline{B}=0$ everywhere in the magnetosphere; meaning that there are no parallel electric fields to accelerate charges along the open field-lines.

Three basic models of the pulsar magnetosphere have been described above, but none of these gives a satisfactory explanation. In the following sections, the mechanisms and models for emission are reviewed through these configurations of the magnetosphere.

1.2.3 Mechanisms And Models For Emission -

Any comprehensive model which tries to account for the observed properties of pulsed emissions need to consider the four following problems:

(i) the radiation be emitted in a relatively narrow beam;

(ii) the mechanism be capable of producing an extremely high

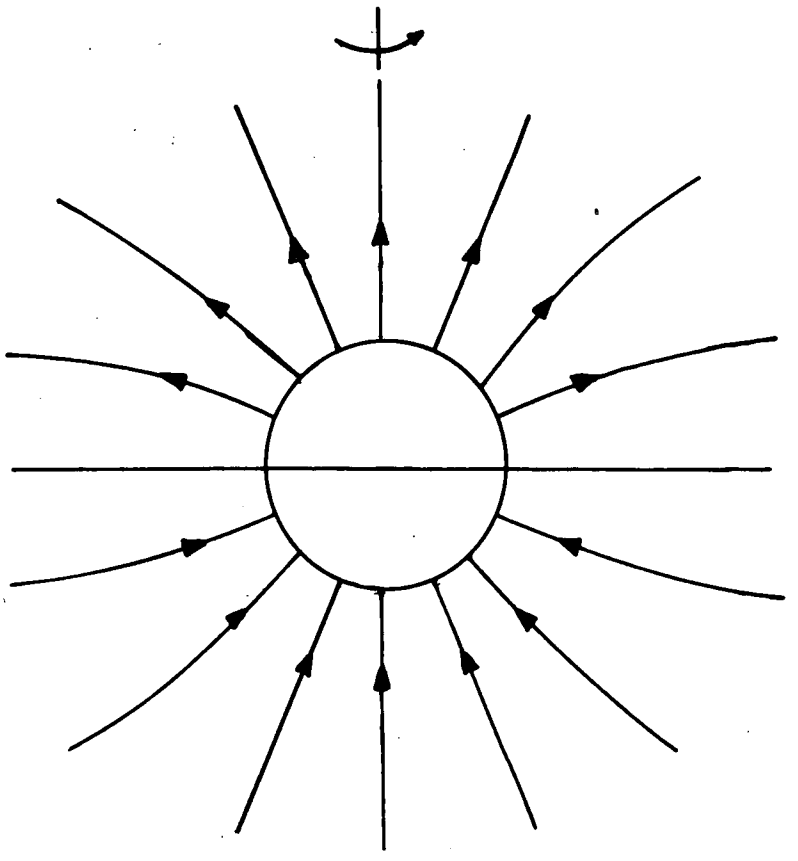

(a)

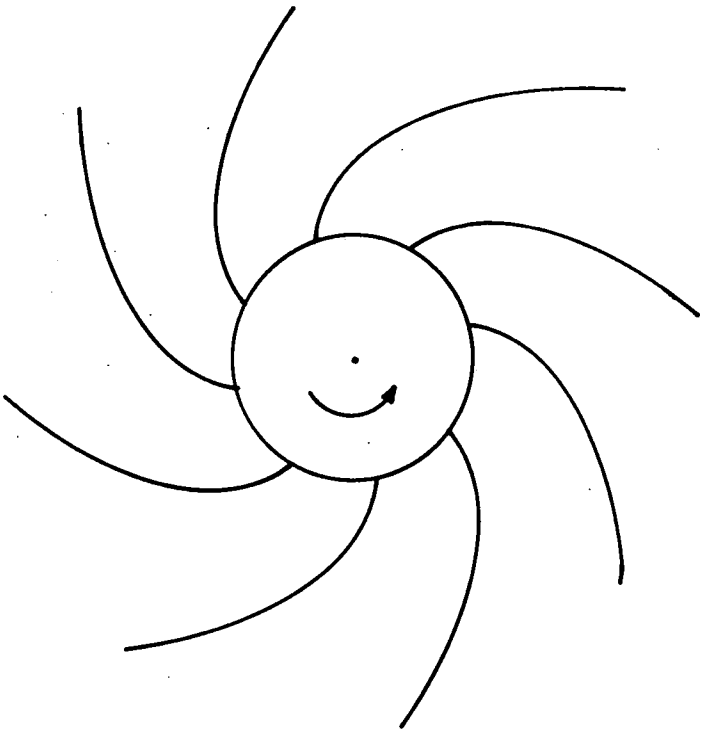

(b)

Figure 1.4 The magnetosphere of a pulsar with a magnetic monopole configuration.
(a) radial field lines in the meridian plane,
(b) Archimedean spirals in the equatorial plane.

specific intensity (or brightness temperature) of broadband radiation;

(iii) be able to produce the energy-independent light curves;

(iv) need to explain the energy emission spectrum from infrared to gamma-ray energies.

The various models proposed so far do not agree in general with one another, but can be conveniently distinguished according to the location of the emission region with respect to the neutron star and light cylinder (Knight 1981). The four different families of model thus devised are the Polar Cap, Outer Gap, Light Cylinder, and Wave Zone models. These models are described below, in each case one example is given either be the original model or a representative of that family.

1.2.3.1 Polar Cap Models -

These models seem to have been most favoured by theorists. There have been numerous papers written on these models which are all based on a model first proposed by Sturrock (1971). In his original model Sturrock suggested that nearly all of the potential between the centre and edge of the polar cap is available to accelerate charges near the surface. Since this potential is $\geq 10^{12}$ V, electrons are accelerated to relativistic factors $\gamma \geq 10^{7}$. Because of the strong magnetic fields in the polar cap region, the lifetime against synchrotron radiation is extremely short, so particles move parallel to the field-lines with essentially

zero pitch angle. However, if the field-lines are curved, the particles radiate the so-called 'curvature' radiation in their direction of motion. The characteristic frequency for this radiation corresponding to the synchrotron relation is

$$\omega_c \simeq \frac{3\,c}{2\,\rho_c}\,\gamma^3$$

where ρ_c is the radius of curvature of the field-line. Thus for $\gamma \simeq 10^7$ and $\rho_c \simeq 10^8$ cm, the characteristic frequency $\omega_c \simeq 5 \times 10^{23}$ s^{-1} i.e. Hertz the radiation would be in the form of gamma-rays with energy ~ 10^9 eV.

A central theme of Sturrock's model is that gamma-rays of this energy moving in a magnetic field of 10^{12} G produce electron-positron pairs. If the electric field is sufficiently strong, the secondary particles will themselves be accelerated and radiate gamma-rays, which in turn can produce further electron-positron pairs. Consequently, a cascade will occur; Sturrock computes that for the Crab pulsar more than 10^7 electron-positron pairs are produced for each primary electron, resulting in a total particle input to the Nebula in excess of 10^{41} s^{-1}. Unfortunately, the central assumption in Sturrock's theory, that the full homopolar potential is dropped along the field-lines near the star, may not be correct.

Further, the assumption that both electrons and ions can flow freely from the neutron star surface may not be true, it is possible that ions will not be ejected from the

surface. Ruderman and Sutherland (1975) have considered the consequences of this restriction on the magnetosphere of an axisymmetric system. They suggest that vacuum gaps form above the neutron star surface in regions where positive charges normally flow. In these gaps $\underline{E}.\underline{B} \neq 0$ and hence field-lines above them are not forced to co-rotate with the star. In the approximation in which the gap height $h < R_p < R$ (where R_p is the radius of the polar cap and R is the radius of the neutron star), Ruderman and Sutherland show that the potential across the gap is

$$\Delta\varphi \approx \frac{\Omega B_o h^2}{c}$$

Since the first model of Sturrock (1971) more detailed models have been developed (e.g. Aysali 1981, Harding 1981) which give good fits to the observed spectra at high energies in the gamma-ray region. In all these models the acceleration is limited either by the space charge limited flow that develops (e.g. Sturrock 1971) or by the onset of pair production in an "inner gap" (e.g. Ruderman and Sutherland 1975). Although refinements of the space charge limited flow models have led to quantitative predictions (e.g. Fawley 1977), there are problems with reproducing the observed spectra and light curves from the Crab and Vela pulsars. Others have tried to solve this analytically difficult problem by numerical simulation using approximations to the various physical processes (e.g. Harding et al. 1978; Aysali and Ogelman 1980).

1.2.3.2 Outer Gap Models -

The outer gap is formed in the region where the diagonal dashed line in Figure 1.2 crosses the open field-lines at a distance of $3x10^7$ cm from the neutron star surface. In the model of Cheng and Ruderman (1977), they considered the Crab pulsar specifically and predicted electron-positron pair production in the outer magnetosphere at the 'outer gap', as a source of emission at all observed energies from optical to Gamma-ray. The model gives optical and X-ray pulses from inverse Compton scattering of radio photons by e^+ and e^- that are created with $\gamma_{||} \sim 10^3$ and $\gamma_{\perp} \sim 10^4$ relative to $\underline{B}$. The synchrotron radiation gives very hard X-rays and gamma-rays up to 10^3 MeV. The Crab radio emissions, except for the precursor, are also predicted to originate from the 'outer gap'.

Inflow of negative charges from this gap (rather than outflow of positive charges from the star) would avoid the problem of charges streaming through regions of opposite sign. The model of Cheng and Ruderman qualitatively predicts the Crab pulsar's energy independent light curve and double peaks separated by 144° using only one magnetic pole. However, the model does not fully explain the existence of the necessary power law distribution of high energy electrons with large pitch angles or the magnetic field structure required.

The refinement of the model of Cheng and Ruderman by Elitzur (1979) shows that outer-gap breakdowns through curvature radiation pair-production cascades can explain the observed gamma-ray emission of pulsars. The shape of the spectrum and the polarization of the optical and X-ray pulses from the Crab pulsar are analysed, assuming that the high-frequency radiation originates from Compton boosting of the radio emission. It predicts one spectral break in the Crab pulsed spectrum and a relation between the gamma-ray efficiency and the apparent pulsar age is obtained. The predicted spectrum is shown to fit well to the observations.

1.2.3.3 Light Cylinder Models -

Many models for the pulse emission process have the pulses originating in a region near the light cylinder. Hardee (1979) locates the emission region at ~ 10^8 cm = $0.7R_L$ from the stellar surface for the Crab pulsar, where the plasma becomes unstable due to filamentation. At this location, the self-pinched filaments generate a magnetic field $\delta\underline{B}$ (~10^6 G) which is perpendicular to the ambient (stellar) field $\underline{B}$, this leads to the scattering of particles entering the unstable region into pitch angles given by $\delta\underline{B}/\underline{B}$ ~ 0.01 radians. The emission spectrum produced by this order of small angle synchrotron emission can be represented by a power law distribution of particles:

$$N(E) \sim E^{-2.2} \qquad 150 < E < 10^7 \text{ eV}$$

which is continuous from infrared to gamma-ray energies. A

steepening of the power law emission spectrum occurs at ~ 10 keV because radiation losses cannot be balanced (in < 10^{-3}s) by new radiating particles.

In order to produce the energy independent light curve, Hardee assumes a small angular size emission region, but confinement of the radiating plasma and the necessity of small pitch angles require multipole magnetic fields of ~ 10^{14}G at the surface of the neutron star. In addition, the large energy of the relativistic particles needed to explain the pulsed luminosity requires that nearly all of the available potential is used to accelerate the particles and may also require non-steady particle flow from the stellar surface. However, the field structure is unknown near the light cylinder, so detailed light curves cannot be produced. Before this model can make any progress, a fuller understanding of the dynamics of the radiating plasma is necessary.

1.2.3.4 Wave Zone Models -

As mentioned earlier when discussing the magnetosphere, the wave zone or wind zone is a region beyond the light cylinder where particles can escaped from the pulsar magnetosphere. The model of (Kundt and Krotscheck 1980) is another model specially designed for the Crab Nebula and its pulsar, involving calculations of the dynamics and radiation of the relativistic material which emanates from the pulsar. They located the pulsed emission beyond the light cylinder

out to ~ 1 light year ~ $10^{16} R_L$ ~ 40 arc seconds. The model shows that both electrons and positrons from the pulsar are injected into the Nebula according to a power law distribution

$$N(E) \sim E^{-2.2} \qquad 3 \times 10^5 < E < 10^9 \text{ eV}$$

The low frequency (30 Hz) waves (dipole radiations) and the relativistic particles contribute about one half of the total energy density, with probably a minute amount of magnetic flux contribution.

The inner part of the Nebula is filled with multiply reflected 30 Hz waves, of field strength $B \lesssim 10^{-3}$ G, which bounce off the thermal component. The observed pulsed radiation, from gamma-ray to X-ray energies, is emitted by extremely relativistic particles on their way from the pulsar out to the Nebula, whose inner edge is located at R ~ 1 ly. In this case the gamma-rays are either synchrotron photons or synchro-Compton radiation, produced as the particles extract energy from the waves (the oscillating radiation field) radiating either via the synchrotron or the Compton process. The photon spectrum will be essentially a power law, but any breaks or slope changes can be produced by modifying the input spectrum. The radius of the emitting region will vary inversely with photon energy.

A predicted transient third peak at X-ray energy between the double peaks of the Crab pulsar light curve is considered as a detour effect, produced at the inner edge of

the Nebula. The kinks in the pulsed spectrum, near photon energies of 10 Mev and 1 keV, are due to the onset of different pulse smearing mechanisms (detouring). The model requires that particles remain phase-locked with the electromagnetic waves to produce the pulsed radiation. An extended structure predicted by the Wave Zone model for the Crab pulsed emission makes it difficult to explain the doubly-peaked Crab light curve.

Although, four different families of models have been described above, as yet, there is no single model that is exotic enough to produce the right answer. The predictions of the characteristics of the pulsed emission and light curve of the Crab pulsar by some models are obviously somewhat better than by others, but each has one or two problems that cannot be accounted for. At any rate, the above and all the problems which remain open do not imply that pulsars are inexplicable objects. Our present knowledge, however poor, is certainly a working one, and in extending it further the contribution of gamma-ray observations will be of paramount importance.

CHAPTER 2

OBSERVATIONAL STATUS

2.1 Historical Observations

Any study on the Crab Nebula and its pulsar would not seem to be complete without mentioning the 'guest star' of AD 1054. The term '*k'o-hsing*' meaning 'a guest star' was used by ancient astronomers of the Far East to describe a new star-like object. Two accounts of the sighting of the Crab SNR are given below which have been taken from the *Sung-shih* [The History of the *Sung* Dynasty AD 960-1279 (China)].

"1st year of the *Chih-ho* reign period, 5th month, (day) *chi-ch'ou* [=AD 1054 July 4]. (A guest star) appeared approximately several *t'sun* (1 *t'sun* ~ 0.1°) to the south-east of *T'ien-kuan* (= ζ Tau). After more than a year it gradually disappeared". (*Sung-shih*, Astronomical Treatise, Chapter 56.)

and in the *Sung-shih* Imperial Annals, chapter 12,

"1st year of the *Chia-wu* reign period, 3rd month, (day) *hsin-wei* [=AD 1056 April 17]. The Director of the Astronomical Bureau reported that since the 5th month of the 1st year of the *Chih-ho* reign period a guest star had appeared in the morning at the east, guarding *T'ien-kuan*, and now it has vanished".

The birth of the Crab Nebula was one of the many guest stars noted by these ancient astronomers and recorded in history books. From these observations we thus have the exact date of the event and also the length of time (a total duration of more than 21 months) the event was visible. A lengthy

entry in chapter 52 of the Sung-hui-yao (Collection of the Essentials of Sung History) indicates that this event was actually visible in daylight for 23 days. The usefulness of these observations is that they place important constraints on any theoretical model of the Crab Nebula and its pulsar. The name "Crab" was given by Lord Rosse in 1844, this Nebula was first associated with the AD 1054 event by Hubble in 1928 and conclusively identified with it by Duyvendak, Cort and Mayall in 1942.

2.2 Discovery Of The Crab Pulsar

With the accidental discovery of a pulsar by Hewish et al. in 1967, nearly every radio telescope in the world was pointed to search for new pulsars. In late 1968, Staelin and Reifenstein (1968) announced the detection of two radio sources in the region of the Crab Nebula. Later, observations made at Arecibo confirmed one of these sources was situated within 5 arc minutes of the centre of the Crab Nebula and that its period was 33 ms. It was also noted that the period was lengthening at a rate of ~36 ns/day. These observations indicated that pulsars were related to supernovae and probably rapidly rotating neutron stars spinning at the observed pulsating frequency. The discovery of the Crab pulsar also fulfilled predictions made by Wheeler (1966) and Pacini (1967) before the discovery of any pulsars, namely, that the energy source in the Crab Nebula could be a rotating neutron star.

Once the positions of the radio pulsars were known, researchers examined the positions using optical telescopes. The confirmation that the Crab emits pulsed radiation at visible wavelengths was provided by Cocke et al. (1969) at the Steward Observatory in Arizona. They found a pulsating stellar source in the centre of the Crab Nebula, with a period equal to that of the radio pulsar. It was soon shown that the star emitting the optical pulses was that identified by Baade and Minkowski in 1942 as a remnant of the supernova explosion. Within the year, pulsations of this object had been detected at X-ray frequencies (Fritz et al. 1969), and later in the gamma-ray region (Hillier et al. 1970).

2.3 Low-energy Gamma-ray Observations Of The Crab

2.3.1 The Importance Of Low-energy Gamma-ray Observations -

Gamma-rays that are produced in this Universe can be grouped in four classes:

(1) Solar System gamma-rays which are produced from Solar flares, lunar and planetary surfaces.

(2) Rapid gamma-ray transients which are produced from gamma-ray bursts anywhere in the sky.

(3) Galactic gamma-rays which are produced by the galactic centre and discrete galactic sources.

(4) Extragalactic gamma-rays which are believed to have been produced by both discrete and diffuse extragalactic emissions.

The Crab Nebula is a discrete source belonging to the class of galactic gamma-rays. At present there exists only a few results on discrete gamma-ray sources in the range between X-ray and high-energy gamma-rays and even these results are sometimes conflicting. Observations in the low-energy gamma-ray region ~ 1 to 10 MeV are motivated by the knowledge that unique astrophysical phenomena may become observable once this nearly unexplored field of astronomy is explored. The reasons behind these thoughts are as follows:

(1) The continuum spectra from low-energy gamma-ray observations will give information on high-energy electrons rather than on high-energy protons. High-energy electrons produce gamma-radiation via bremsstrahlung, inverse Compton collisions or as synchrotron radiation. Even thermal bremsstrahlung production seems to be possible at low gamma-ray energies.

(2) The possibility of observing gamma-ray lines in the low-energy gamma-ray range is by far the more interesting aspect. Gamma-ray lines are expected from the decay of radioactive nuclei, which were produced during explosive nucleosynthesis processes in supernova remnants. Observation of these lines will provide a unique means to observe nucleosynthesis processes directly. Also, gamma-ray lines are produced in nuclear interactions of energetic nucleons (typically 10 MeV per nucleon) with interstellar matter or with matter near the surface of a neutron star. By observing gamma-ray lines from nuclear interactions, information can be obtained on the flux and spectral shape

of these energetic particles which cannot be obtained by other means. The shapes of gamma-ray lines contain valuable information on the physics of the emitting region, and they are important for considerations regarding the detectability of the lines above background.

Although, hope has been high since the first gamma-ray experiment progress is not keeping pace with expectation. The slow progress in low-energy gamma-ray astronomy is mainly due to experimental difficulties. These difficulties are essentially threefold:

(1) The sensitivity of experiments flown so far is poor. This is due to small detection areas or low detection efficiencies of the instruments, and also the observation times have been too short because most experiments were flown on balloons where sources could be observed only for periods of some hours.

(2) The directional resolution of existing experiments is insufficient. For most instruments it is worse than 10° and in some cases the detectors were even only omnidirectionally sensitive.

(3) Most experiments suffer from large atmospheric and detector background fluxes.

Up to now, the only galactic source which has been investigated with much effort by various experimental groups is the Crab Nebula and its pulsar. Although there seems to be more or less a general agreement on the flux of the pulsar, reports on the total Crab emission in the 1 - 10 MeV

band differ by as much as a decade. In the following the observations on both the Crab Nebula and its pulsar are reviewed.

2.3.2 The Crab Nebula -

Where as a pulsar can be identified by its periodicity, it is much more difficult to detect a continuous source. In order to resolve a continuous source against the background radiation it is necessary to have directionally sensitive detectors. In most cases directionality in low-energy gamma-ray astronomy is obtained by shielding of the detector or occultation of the source. In the former case 'source-on' - 'source-off' observations are necessary so that the 'background only' counts may be subtracted from a 'source region' counting rate. This procedure is not without problems, because in order to obtain the correct result the background must be the same in both cases. The difficulties may be the reason for the discrepancies in the total gamma-ray fluxes that have been reported by various workers from the Crab between 1 and 10 MeV.

The usual technique employed to obtain an energy spectrum of the total Crab emission requires the conversion of the excess counting rate at the position of the Crab into a gamma-ray flux. In the region between 1-10 MeV Walraven et al. (1975) have produced results which agree with a simple power-law extrapolation from the X-ray region, however, Baker et al. (1973) and Gruber and Ling (1977) give

evidence for a flattening of the spectrum in this region which produces a flux a factor of ~ 7 to 30 above such extrapolations. Figure 2.1 shows the collective differential photon spectrum for the total Crab emission between 10 keV and 100 MeV. All data except those between 1 and 10 MeV can be fitted by a power law ~ $E^{-2.3}$. This figure clearly illustrates the discrepancies between different measurements in the range from 1 to 10 MeV and the spectral shape in this region has yet to be resolved.

2.3.3 The Crab Pulsar -

Pulsed emission from the Crab pulsar has been studied extensively in the optical, X-ray and gamma-ray bands. The different light curves of the Crab pulsar from radio to high-energy gamma-ray energies are shown in Figure 2.2. Light curves of the Crab pulsar in the five different energy regimes (radio, optical, X-ray, low-energy gamma-ray and high-energy gamma-ray) seem to have a similar shape. It is easy to say that they have a common origin, but minor details of individual light curves are different. At radio frequency, a third pulse component, known as the precursor is detected preceding the main pulse. The optical profile remains significantly above zero level between the two pulse components. This is the same case at X-ray energies, presumably the emission mechanisms are more closely related. The light curve in the X-ray energies shown was measured between 100 and 400 keV by Kurfess (1971) with an omnidirectional NaI detector. The pulsar events were

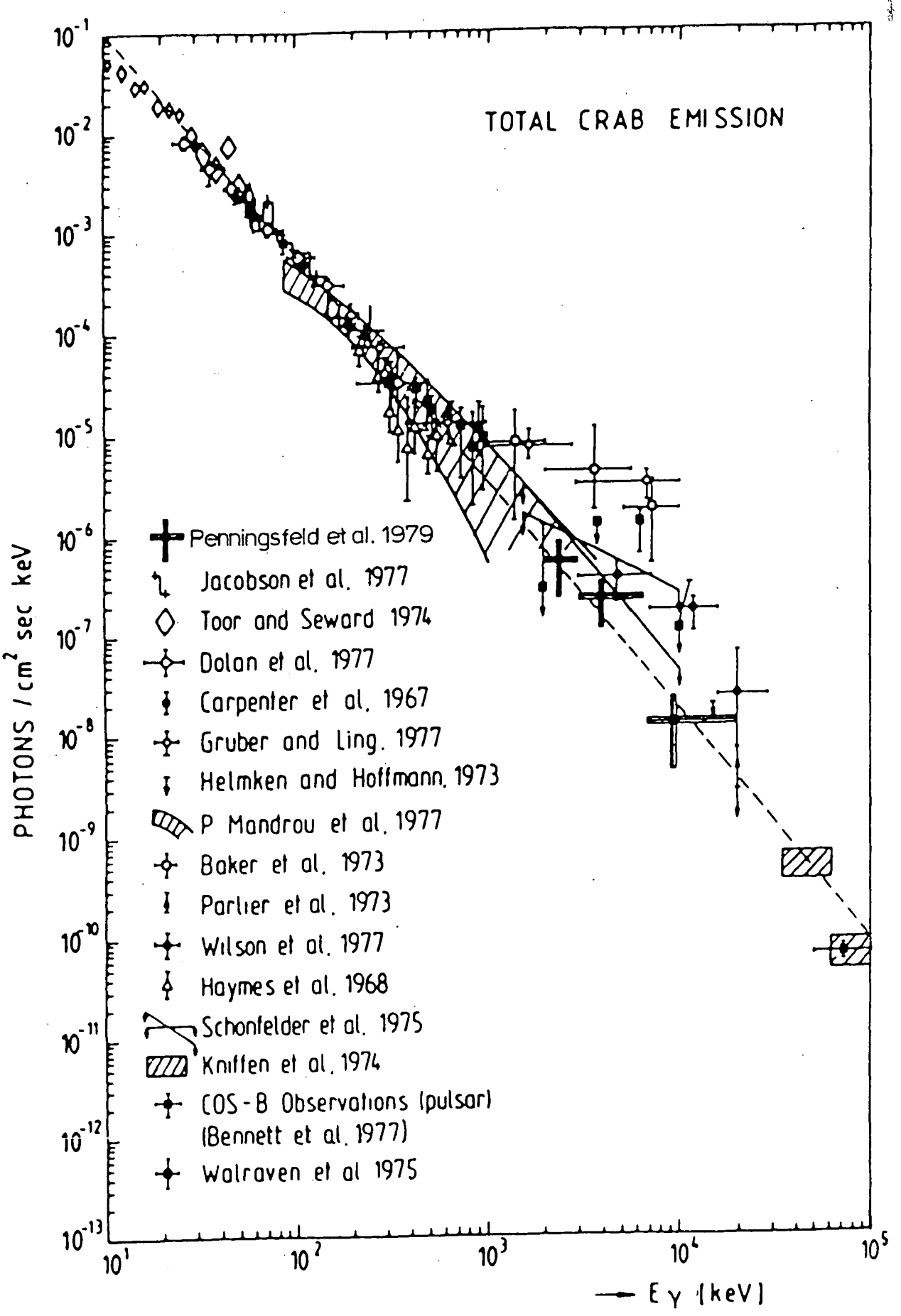

Figure 2.1 Photon number spectrum of the total Crab emission between 10 keV and 100 MeV (After Penningsfeld et al. 1979)

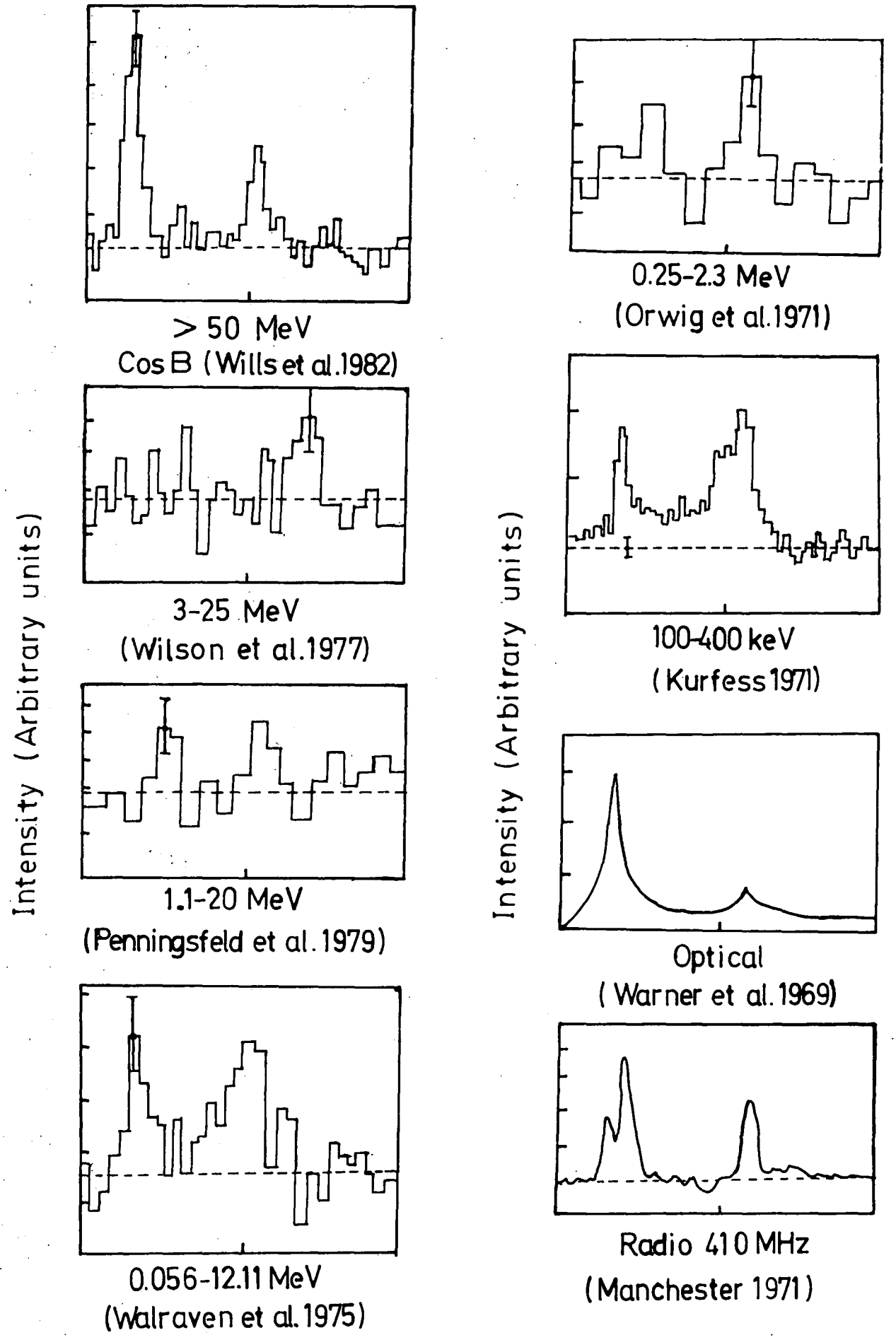

Figure 2.2 Light curves of the Crab pulsar from radio to high-energy gamma-ray

identified by their periodicity. From these observations gamma-ray flux values up to 3 MeV can be derived. A nearly identical experiment was flown at about the same time by Orwig et al. (1971); their light curve in the energy interval 250 keV - 2.3 MeV is also shown.

At MeV energies, three light curves from different experiments are shown. The light curve obtained by Walraven et al. (1975) using a NaI detector between energy interval 56 keV to 12.11 MeV seems to have the best statistics. Penningsfeld et al. (1979) of the Max-Planck-Institute in Garching, using a Compton-telescope obtained a light curve between 1 and 20 MeV, but statistics are poor. The light curve of a similar experiment (Wilson et al. 1977) using the University of California, Riverside, double Compton-telescope is for the energy range 3 to 25 MeV. The Cos-B light curve (Wills et al. 1982) at high-energy gamma-ray above 50 MeV is shown for comparison.

The pulse structure, consisting of a main pulse and an interpulse with a separation of about 0.4 in phase (~144° of 360°), seems to be the same at all energies. The relative intensity, height and width of these peaks varies with energy, but it seems that the statistical significance is much worse at low gamma-ray energies than in the other ranges. This fact once again illustrates the difficulties of observations at MeV energies. The flux between the two peaks is consistent with zero at all energies except at the optical and hard X-ray regions. The excess flux above zero

observed in the hard X-ray energies has interesting implications. Knight (1982) shows that there are two pulsed emission components for this energy range: the emission from the two main pulse peaks and a separate interpulse emission connecting the two peaks known as the 'light bridge'. The interpulse emission is found to contribute 22% of the total pulsed flux between 15 and 200 keV and has a harder spectrum than the spectrum for the two main pulse peaks.

2.3.4 Observed Gamma-ray Line Features -

Although, pulsed gamma-ray emissions from the Crab have long been observed, in fact, it was first observed during a balloon-borne measurement of the Crab Nebula back in 1967 (Fishman et al. 1969), experiments with detectors that are specially designed to observe gamma-ray lines have only been a recent development. Walraven et al. (1975) observed the Crab Nebula and its pulsar using an actively collimated scintillation counter. It consisted of a NaI(Tl) central crystal 15cm in diameter and 5cm thick surrounded by an anti-coincidence shield also constructed from NaI(Tl) crystals. The measurements were conducted in the 56 keV to 12.11 MeV energy range with a field of view of 13° full width at half-maximum (FWHM). They were able to measure the energy spectra from both the Crab Nebula and its pulsar and found it could be fitted by a simple power law. No significant departures from these fits were observed, but the 2σ upper limits on spectral line emission were listed.

The first reported line emission feature from the Crab with a statistical significance was a line at 400 $\pm$ 1 keV by Leventhal et al. (1977). The experiment was conducted on the 10th-11th May 1976 with a balloon-borne telescope from Alamogordo, New Mexico. The detector was a 92cm^3 lithium drifted germanium Ge(Li) detector surrounded by an anticoincidence shield of active NaI. The energy resolution of the system below 2 MeV was 3.4 keV FWHM and an aperture varying with energy between 11° FWHM at 59 keV and 13° FWHM at 1.33 MeV. The 400 keV line was detected with an intensity of (2.24 $\pm$ 0.65) x 10^{-3} photons cm^{-2} s^{-1} and width less than 3 keV, which corresponds to a 3.5σ excess. Leventhal et al. suggested that the possible origin of this line as the gravitationally redshifted 0.511 MeV positron annihilation line produced near the surface of a neutron star. Yoshimori et al. (1979) performed a similar experiment using a Ge(Li) spectrometer on 30th September 1977 and observed a line feature at 400 keV with a flux of (7.4 $\pm$ 5.4) x 10^{-3} photons cm^{-2} s^{-1} but the statistical significance is clearly low.

A search by Ling et al. (1977) for this reported line feature in the data they obtained during a balloon flight on 10th June 1974 yielded a null result. If the 400 keV line had been observed with the intensity measured by Leventhal et al., it would have been observed with a 3.9 σ significance. The experiment was conducted over Palestine, Texas with a balloon-borne high-resolution gamma-ray spectrometer. The instrument consisted of four 40 cm^3

lithium ion drifted germanium crystals Ge(Li) surrounded by a CsI anticoincidence shield 6.35 cm thick. The energy resolution of the spectrometer was about 2.2 keV at 122 keV and an angular resolution of 30° FWHM. The instrument operated in the energy range of 0.06-10 MeV and observed the Crab Nebula region for 6.5 hrs. As the two observations were separated by 2 years, Ling et al. (1977) were careful not to rule out the possibility that the reported feature could vary with time.

In the same data collected by this balloon flight of 10th June 1974, four transient lines were seen during a twenty-minute period (Jacobson et al. 1978). These lines were at energy 413 keV, 1.79, 2.2 and 5.95 MeV which appeared in the background spectrum without any appreciable continuum emission. The widths of these lines (15 keV to 95 keV) were all broader than the instrument's resolution. The events observed by the main detector system were also accompanied by correlated behaviour in several shield segments. The events are quite different in character from the types of cosmic transients reported by Teegarden and Cline (1980). Lingenfelter et al. (1978) suggested that these gamma-ray transient lines could result from episodic accretion onto a neutron star from a binary companion leading to redshifted lines from the neutron star and unshifted lines from the atmosphere of the companion star. The positron annihilation and neutron capture on hydrogen and Fe^{56} near the surface of the neutron star with a surface redshift of ~0.28 would produce the observed

redshifted line emission at about Ø.41, 1.79 and 5.95 MeV respectively. A similar process in the atmosphere of the companion star would produce unshifted lines, the 2.2 MeV line resulting from neutron capture on hydrogen. Unfortunately, spatial resolution of the source direction can not be achieved because the large field of view (3Ø° FWHM) of the telescope.

Although the 4ØØ keV line was not seen during the flight of 1974, a line feature at (73.3 ± 1.Ø) keV in the direction of the Crab Nebula region was detected at 3.8 σ confidence (Ling et al. 1979). The line has an intensity of (3.8 ± Ø.9) x $1Ø^{-3}$ photons cm^{-2} s^{-1} and a width less than 4.9 keV FWHM. No evidence was found for any pulsed emission within the sensitivity of the experiment.

Several efforts were made to observe this line and confirmation of this line was provided by Manchanda et al. (1982) and Strickman et al. (1982). Manchanda et al. reported a feature around 73 keV with intensity (5.Ø ± 1.5) x $1Ø^{-3}$ photons cm^{-2} s^{-1} and width less than 4 keV. The experiment was carried out using a balloon-borne multiwire, high-pressure xenon proportional counter flown from Milo Base, Sicily (Italy) on 26th August 1979. The fields of view of the detectors were 7.5° x 7.5° and 5.Ø° x 5.Ø° FWHM and operated in the energy range 2Ø-15Ø keV.

Strickman et al. (1982) observed a transient line at 77 keV which was pulsed at the Crab pulsar frequency during a balloon-borne experiment over Palestine, Texas on 11th May 1976. The detector consisted of a 5mm thick NaI(Tl) central crystal and a caesium iodide CsI(Na) backplate in a phoswich configuration, shield by a CsI(Na) collimator. The field of view was 10° FWHM and the energy resolution was 24% FWHM at 60 keV. The 77 keV line was detected for the first 25 minutes of a three hour observation and then disappeared below the continuum.

The possible origin of this line feature in the 73 to 77 keV region has been interpreted as the cyclotron radiation in the intense magnetic field surrounding the pulsar, but as yet no model has been proposed to explain the intensity variations of the line.

Recently, Hameury et al. (1983) reported that they did not see any line feature at 73 or 400 keV with 3 σ upper limits of 6.2×10^{-3} photons cm^{-2} s^{-1} and 1.7×10^{-3} photons cm^{-2} s^{-1}. The experiment was conducted on the 25th September 1980 using a balloon-borne high-energy resolution spectrometer launched from Palestine, Texas. The instrument consisted of an array of three 1 cm thick high-purity germanium planar detectors with a total effective area of 53 cm^2 at 60 keV. These detectors were collimated by an active NaI shield of about 10 cm thick and a passive iron collimator which defined a field of view $5^{\circ} \times 10^{\circ}$ FWHM. The energy resolution of the detector was about 1.4 keV over the

its operational energy range 20-800 keV.

The essential characteristics of the various detectors mentioned above are summarised in Table 2.1. Thus far, only two potential line features have been observed in the Crab gamma-ray spectrum. These occurred at energies of ~ 400 keV and ~ 73 keV and have conflicting statistics. Before any positive conclusion can be drawn, further evidence of these lines or observation of more lines is necessary. It was with the aim of providing further observational evidence that the Durham high resolution spectrometer was constructed and this is described in the next chapter.

TABLE 2.1 CHARACTERISTICS OF VARIOUS DETECTORS

	Dimensions of Central Detector	Shielding Thickness	Field of View
Walraven et al 56 keV - 12.11 MeV	NaI(Tl) 182 cm^2 5 cm thick	NaI(Tl) 12.7 cm	13° FWHM
Leventhal et al 100 keV - 5 MeV	Ge(Li) 85 cm^3 17.3 cm^2	NaI(Tl) 200 kg 15.2 cm	13° FWHM
Ling et al 50 keV - 10 MeV	Ge(Li) 4 x 40 cm^3 53.8 cm^2	CsI(Na) 6.35 cm	30° FWHM
Manchanda et al 20 - 150 keV	Xenon proportional counter 900 cm^2 10.5 cm (depth)	2.63 atm gas mixture	7.5°x7.5°FWHM
Strickman et al 20 - 250 keV	NaI(Tl) 765 cm^2 5 mm thick	CsI(Na)	10° FWHM
Hameury et al 20 - 800 keV	Ge(Hp) 53 cm^2	NaI 10 cm	5°x 10° FWHM

CHAPTER 3

EXPERIMENTAL APPARATUS AND TECHNIQUES

3.1 The Durham MK1B Spectrometer

3.1.1 General Introduction -

Photons in the low-energy gamma-ray region below ~10 MeV interact with matter through three primary processes: the photo-electric effect, Compton scattering and pair production. The nature of these interactions is such that the range (measured in g cm^{-2}) of gamma-ray photons in matter is roughly independent of the material. The consequences of this fact present one rather unfortunate problem for gamma-ray astronomy. Consider for example, a 1 MeV photon which has a range of about 15 g cm^{-2} in air or approximately a kilometer. This means that photons incident on the top of the Earth's atmosphere will never reach sea level. The implication of this for those experimenters working in the field of low-energy gamma-ray astronomy is obvious; they must carry their detectors to a height where attenuation of gamma-rays by the Earth's atmosphere is negligible. The detector can either be carried by a satellite or by a balloon. Although, potentially better quality results may be obtained from a satellite experiment than with a balloon experiment, the cost of a satellite

experiment is usually prohibitive and so a balloon experiment is commonly the inevitable choice.

As the detector has to be deployed at a high altitude and owing to the extreme forces and large variations both in temperature and pressure encountered during launch, float and descent; the detector not only has to be small and compact so as to reduce the mass and volume of the total pay load, but also has to be structurally strong and protected to withstand these conditions. Apart from these fundamental criteria, the following features have to be optimised in the design of a good detector: counting rate, energy resolution, detection efficiency, small acceptance angle, precision timing and, a versatile, accurate steering system. The Durham MK1B Nuclear Gamma-ray Spectrometer was designed and built with these considerations in mind for the study of gamma-ray lines from discrete sources. The basic detector is a hyperpure Germanium crystal Ge(Hp) situated inside an anticoincidence shield comprising three NaI(Tl) crystals. A cross-sectional view of the spectrometer is shown in Figure 3.1. The details of individual element are described under their respective headings below.

3.1.2 The Germanium Detector -

This is an intrinsic, hyperpure germanium crystal of volume 86 cm^3 in a right circular, cylindrical, closed-end coaxial configuration. The crystal, having diameter of 50mm and length 44mm is situated at the end of a cold finger 50cm

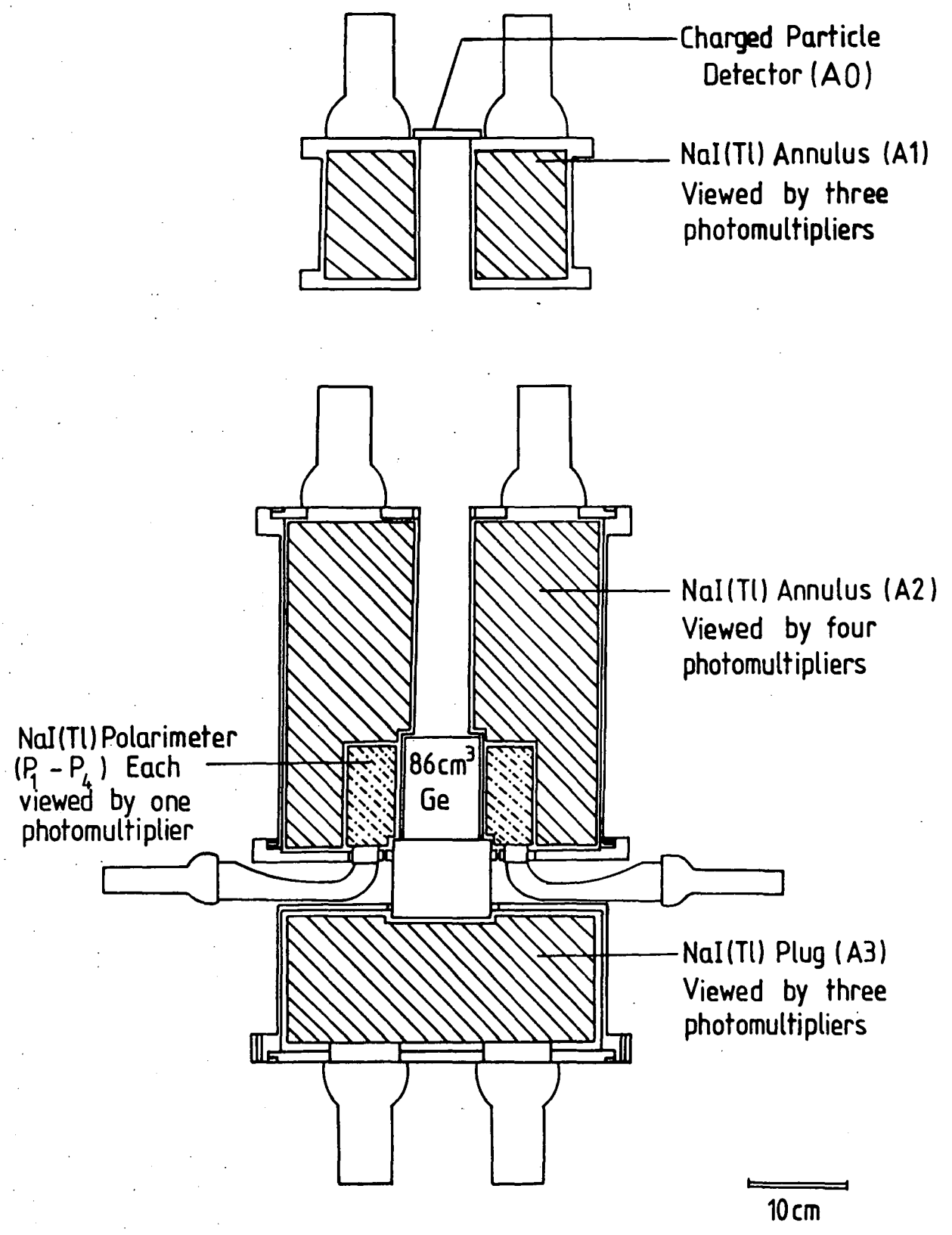

Figure 3.1 Cross-sectional representation of the Durham Gamma-ray Spectrometer.

long attached to a dewar which can contain a maximum of 20 litres of liquid nitrogen (Figure 3.2). Under normal atmospheric pressure the liquid nitrogen consumption is ~1.6 litres per day, and the system can operate without refilling for at least 7 days. During the balloon flight the pressure of the liquid nitrogen is controlled by a relative pressure relief valve which is set to open at a differential pressure of 0.4 bar. This ensures that the temperature of the liquid nitrogen remains above -210 °C and therefore the nitrogen remains in the liquid state. The preamplifier of the Ge(Hp) detector was moved from its normal position near the detector to a point ~ 50cm from the crystal head so that the NaI(Tl) shield could be fitted closely around it. The Ge(Hp) detector has an efficiency of 23% at 1.33 MeV relative to a standard 3" NaI(Tl) detector irradiated by an axial, point source at a distance of 25cm from its top surface, and an energy resolution of 2.12 keV at 1.33 MeV and 0.985 keV at 122 keV. The energy resolution and absolute photo-peak efficiency of the Ge(Hp) detector have been measured in the laboratory using coaxially placed radioactive sources and the results are shown in Figure 3.3.

3.1.3 The Anticoincidence Shield Array A0,A1,A2 And A3 -

A0 is a 3mm thick charged particle detector covering the aperture of the spectrometer. This is a circular disc 75mm in diameter made from NE102a plastic scintillator. The usefulness of a plastic scintillator is that it detects charged particles traversing it but is almost totally

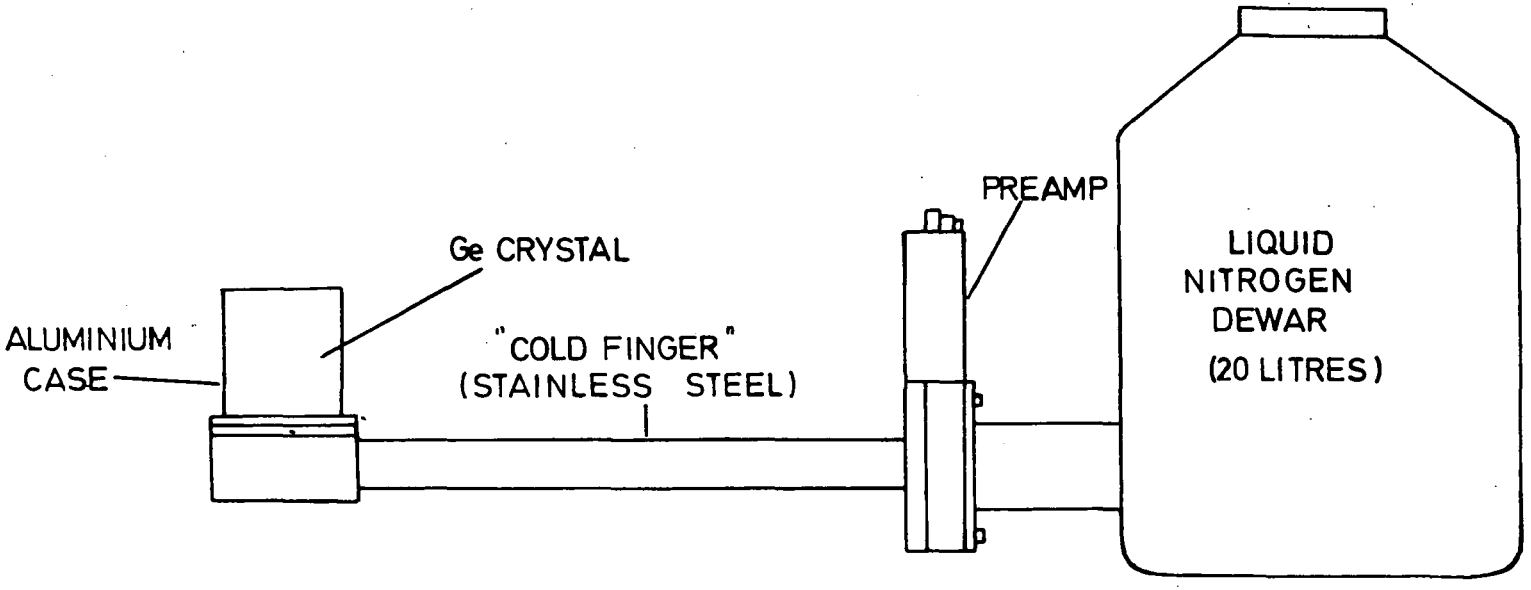

Figure 3·2 The layout of the Ge crystal, Preamp and Liquid Nitrogen Dewar.

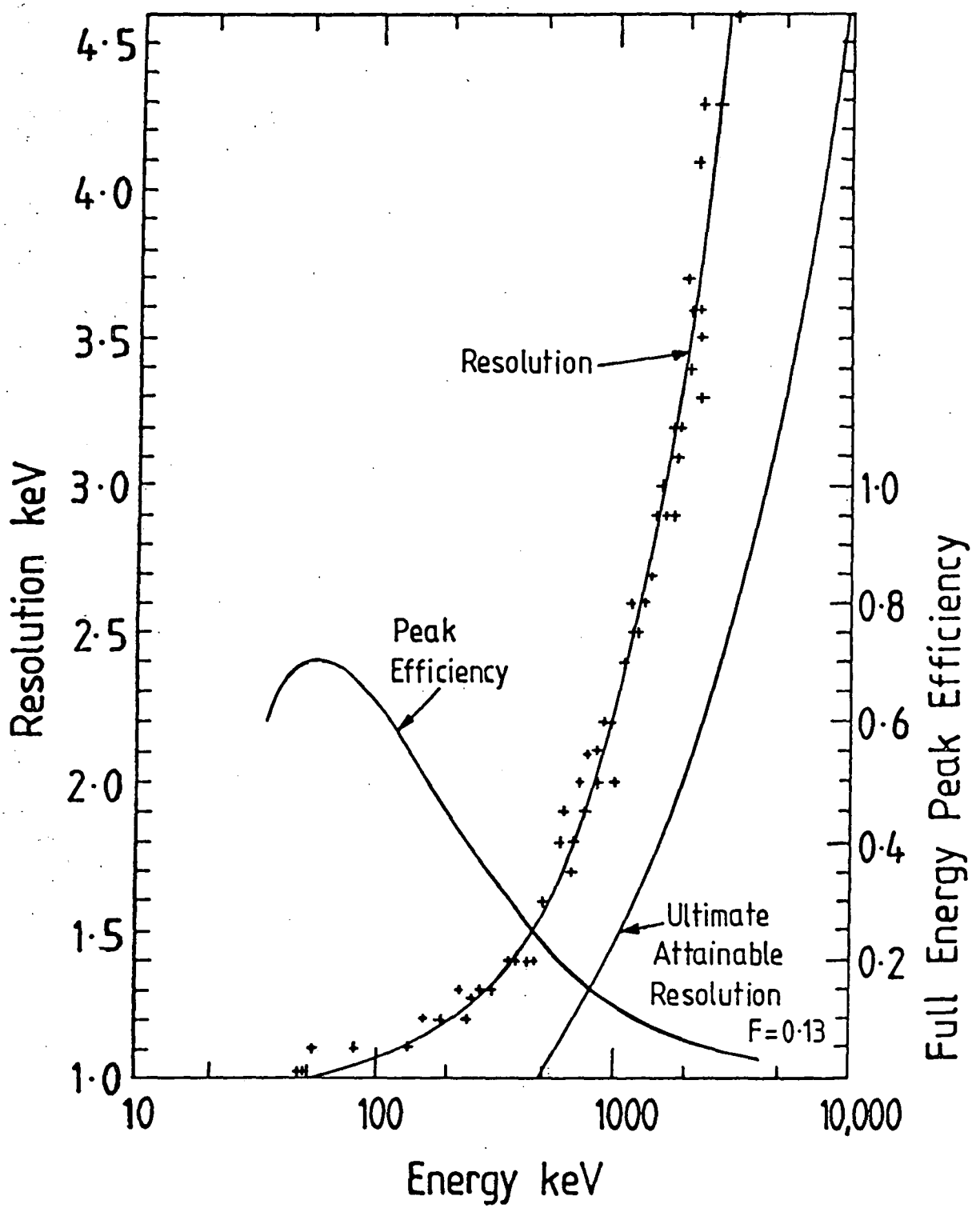

Figure 3.3 The energy resolution and photopeak efficiency of the Spectrometer.

transparent to gamma-rays. Events which are coincident with pulses from this detector are not recorded. This detector is viewed by a photomultiplier tube (EMI 9757B) via a perspex, light-pipe optically connected to its edge.

A1 is a right-cylindrical annular NaI(Tl) crystal, of diameter 22cm and thickness 15cm (Figure 3.4). This element is viewed by three 3" photomultiplier tubes (EMI 9758) and the condition necessary for the detection of an event is that at least two of the tubes detect >50 keV deposited in the crystal. At balloon altitudes this unit counts at 4.2 x 10^3 s^{-1}. This element is intended to limit the aperture of the spectrometer; such that the geometric aperture of the spectrometer incorporating A1 is 4.78° (FWHM).

A2 is a collimation crystal of thickness 30cm and diameter 30cm (Figure 3.5). A2 shield is viewed by four 3" photomultipliers of the same type as used to view A1, and the counting rate of A2 is typically 16 x 10^3 s^{-1} at an atmospheric depth of 5.4 g cm^{-2}.

A3 is a cylindrical crystal of thickness 14cm and diameter 30cm (Figure 3.6). The element A3 is viewed by three 3" photomultipliers (EMI 9758) and a necessary requirement is that at least two of the three photomultipliers detect >50 keV deposited in the unit. With this threshold, the unit counts at 5.3 x 10^3 s^{-1} at an atmospheric depth of 5.4 g cm^{-2}. At 662 keV the resolution (FWHM) of the individual crystals A2 and A3 are 12.7% and 10.2% respectvely.

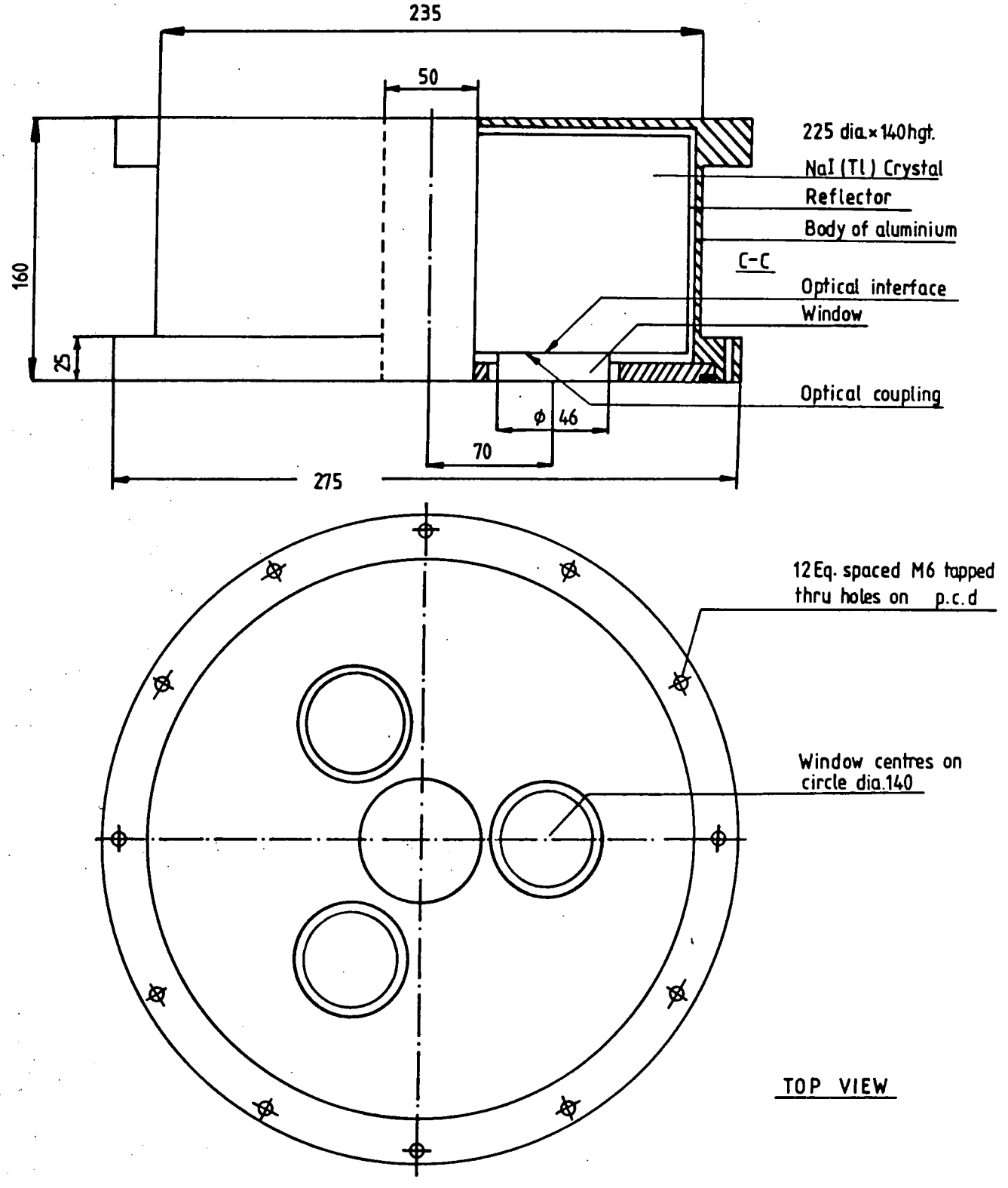

Figure 3.4 The A1 annular crystal assembly

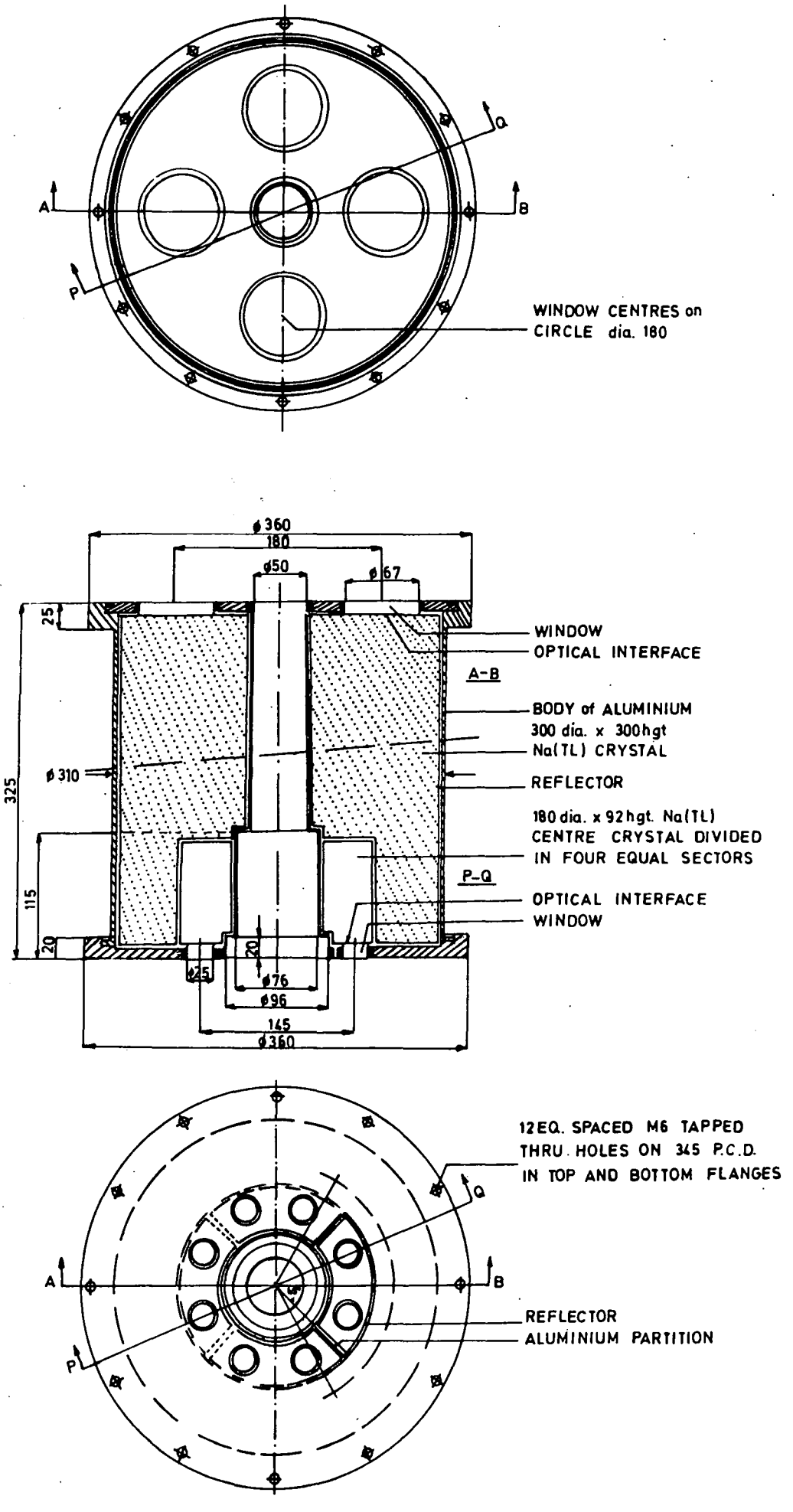

Figure 3·5 The A2 annular crystal assembly.

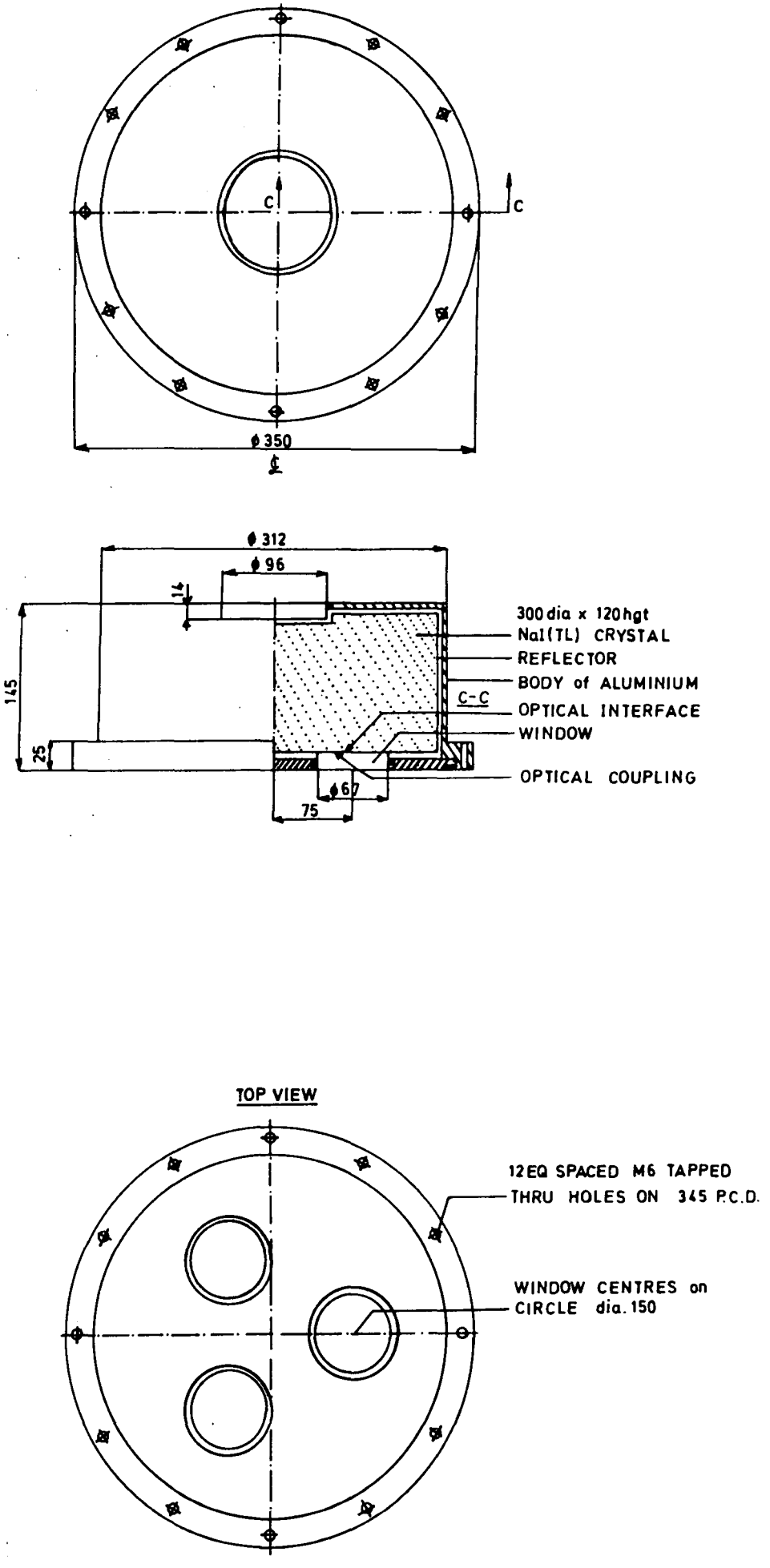

Figure 3·6 The A3 crystal assembly.

All the above mentioned NaI(Tl) shield elements are hermetically sealed inside aluminium containers to prevent hygroscopic dissolution of the crystals. NaI(Tl) crystals were chosen because of Na(Tl)'s low self absorption of scintillation photons, high light output and stability over a wide range of temperature. The active shield array in total weighs ~ 180 kg.

3.1.4 The Polarimeter P1 - P4 -

The polarimeter was bored out of the main collimation shield A2, and segmented into the form of four quadrants. These were then replaced within the the body of A2 but kept optically isolated. The polarisation measuring crystal segments (P1 - P4) are each of thickness 6cm and are 9cm tall. The upper end of the annulus formed by the quadrants is in the same plane as the upper face of the Ge(Hp) crystal. Each polarimeter segment is viewed by a single 2" photomultiplier (EMI 9757) through intermediate light pipes. The resolution of the polarimeter segments is about 25%, and the count rate of each polarimeter segment at float altitude is $7 \times 10^{2} s^{-1}$. The polarisation of incoming gamma-rays are studied via the Compton scattering of the gamma-rays in the Germanium crystal and their subsequent detection in one segment of the polarimeter.

3.1.5 The Gondola -

The spectrometer together with its associated electronics were contained in a pressurised shell which was hermetically sealed and thermally insulated. The entire dome was protected by a rectangular cage constructed from Aluminium scaffolding tubes. This overall arrangement is known as the "gondola" and is illustrated in Figure 3.7.

3.2 Methods Of Data Recording

Operation of a scintillation crystal detector may be described as follows. An incident photon strikes a NaI crystal and interacts by one of the processes mentioned above (ie.the photo-electric effect, Compton scattering and pair production). Because of this interaction, an energetic electron is produced in the crystal which subsequently loses its energy to the atoms of the crystal, by excitation and ionization. The consequent de-excitation of these atoms, results in the emission of optical photons, which are detected by the photomultiplier tubes. The height of the electrical pulses from these photomultipliers are analysed (pulse height analysis) to obtain a measure of the energy which has been deposited in the crystals. The total energy of the gamma-ray may be transferred to the scintillation crystal if the gamma-ray interacts by way of the photo-electric effect. If however, the initial interaction is a Compton collision, the scattered photon may exit the crystal without further interaction. Whenever pair

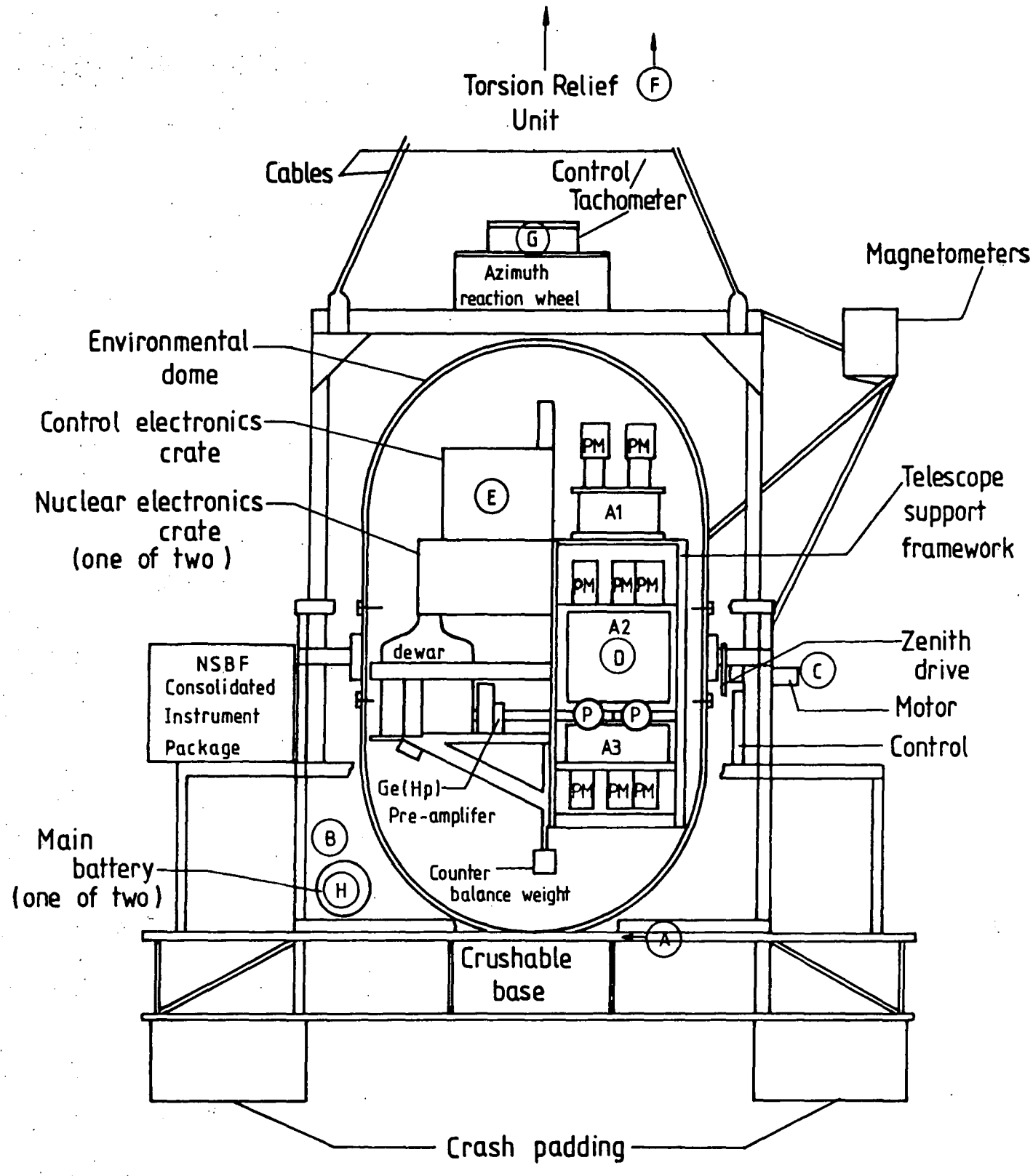

Key:- PM Photomultiplier tubes

Ⓐ·····Ⓗ Positions of temperature sensors

Figure 3.7 Cross-section of the Gondola and Environmental dome.

production occurs within the crystal, it is followed by the annihilation of the created positron. One or both of the 511 keV photons produced by the positron's annihilation may escape from the crystal without interaction.

An anticoincidence technique is used both to collimate the viewing direction and to suppress Compton scatters from the Germanium crystal. When a coincidence occurs between an event in the Ge(Hp) detector and one segment of the shield, the central crystal count is recorded and flags set to indicate the nature of the coincidence. The energy deposited in the shield is also recorded. The classification of the data into coincident and anticoincident events is made subsequently software-wise from the raw data available from the spectrometer.

The analogue pulses derived from the Ge(Hp) detector range from 0-10 V and represent 0-10 MeV deposited in the crystal; these pulses are analysed using a 16384 channel ADC which gives a resolution of ~ 0.65 keV per channel. The low energy threshold of the detector is ~ 50 keV, therefore the spectrometer operates in the range from 50 keV to 10 MeV. The electronic system has the capability of analysing two coincident pulses occuring within the spectrometer, with an instrumental resolving time of 1 μs.

The pulses chosen for analysis follow a predefined hierarchy. A trigger in the Ge(Hp) detector is analysed together with one of the shield elements, P1, P2, P3, P4, A1, A2, A3; the order given being the order of precedence.

The conditions for the detection of a shield signal are as follows:

(i) AØ - its single photomultiplier generates a signal, this unit has a hardware veto on all other triggers;

(ii) A1, A2 and A3 - coincidence signals from any two of the photomultipliers on at least one of these units above a discrimination level of 5Ø keV;

(iii) P1 to P4 - any one of the photomultipliers detects a signal.

A positive trigger from the Ge(Hp) detector is conditional upon there being no trigger from either the combined shield A or any polarimeter element P. The energy spectrum from the Ge(Hp) detector for positive events, both 'on-source' and 'off-source', can be obtained by off-line analysis by scanning the data for events which correspond to a trigger of Ge, that is $\overline{(A+P)}$.

3.3 Telemetry Systems

The Durham balloon flight used the facilities offered by the National Scientific Balloon Facility (NSBF) in Palestine, Texas, U.S.A.. For each balloon flight NSBF provides a Consolidated Instrumentation Package (CIP). The package comprises the following items:

L band telemetry transmitter

Command receiver

Omega Navigation system

Resemount altimeter

FM/FM telemetry system

PCM telemetry encoder

Command decoder

The Pulse Code Modulation (PCM) encoder is a Spacetac 2100 having a PROM programable format and providing forty-eight analogue and twelve 10-bit digital input channels. The data are telemetered to the NSBF, Palestine ground station at a transmission rate of 40.96 kbits/s. All information recieved at the ground station was recorded via a DEC PDP11/20 minicomputer onto industry standard 800 BPI computer tape together with a "ground-frame" containing timing and positional information. The layout of the format is shown in Figure 3.8. The positions of the detector (latitude and longitude) are derived from the Omega navigation system which locates the balloon to within a one mile square box. The Rosemount altimeter incorporates a displacement/frequency transducer of sufficient sensitivity to be capable of detecting an altitude change of less than 0.1% at 120,000 feet.

3.3.1 Durham Telemetry Format -

The PCM telemetry unit supplied by NSBF can sample a variety of analogue and digital channels in a predefined sequence. All twelve of the available digital channels and thirty-two of the analogue channels were used for the Durham spectrometer flight. Figure 3.9 shows the arrangement of the Durham experiment's data formats.

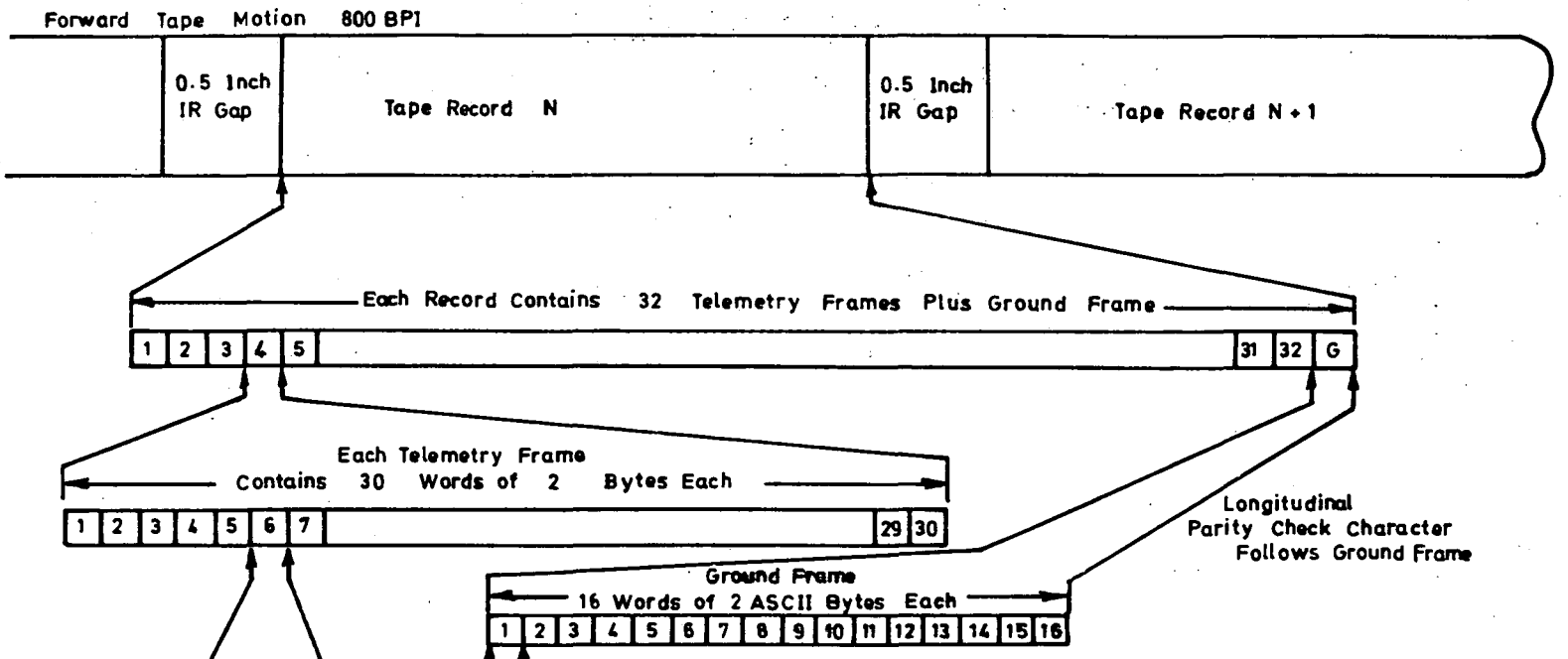

Tape Track	Byte 1	Byte 2
	Odd Parity	Odd Parity
9		128
8		64
7		32
6		16
5		8
4		4
3	512	2
2	256	1
1	Binary	

Byte 1	Byte 2
Odd Parity	Odd Parity
0	0
0	0
Fixed One	Fixed One
Fixed One	Fixed One
8	8
4	4
2	2
1	1
ASCII	

Data Contained in Ground Frame					
Word	Byte 1	Byte 2	Word	Byte 1	Byte 2
1	Year Tens	Year Units	9	Long Deg 100	Long Deg Tens
2	Mo Tens	Mo Units	10	Long Deg Units	Long Min Tens
3	Day Tens	Day Units	11	Long Min Units	Long Min 1/10
4	Hour Tens	Hour Units	12	Lat Deg Tens	Lat Deg Units
5	Min Tens	Min Units	13	Lat Min Tens	Lat Min Units
6	Sec Tens	Sec Units	14	Lat Min 1/10	Pressure
7	Sec Tenths	Sec 1/100	15	Pressure	Pressure
8	Sec 1/1000	Sec 1/10000	16	Pressure	Pressure Rge

Figure 3-8 The format for each tape record.

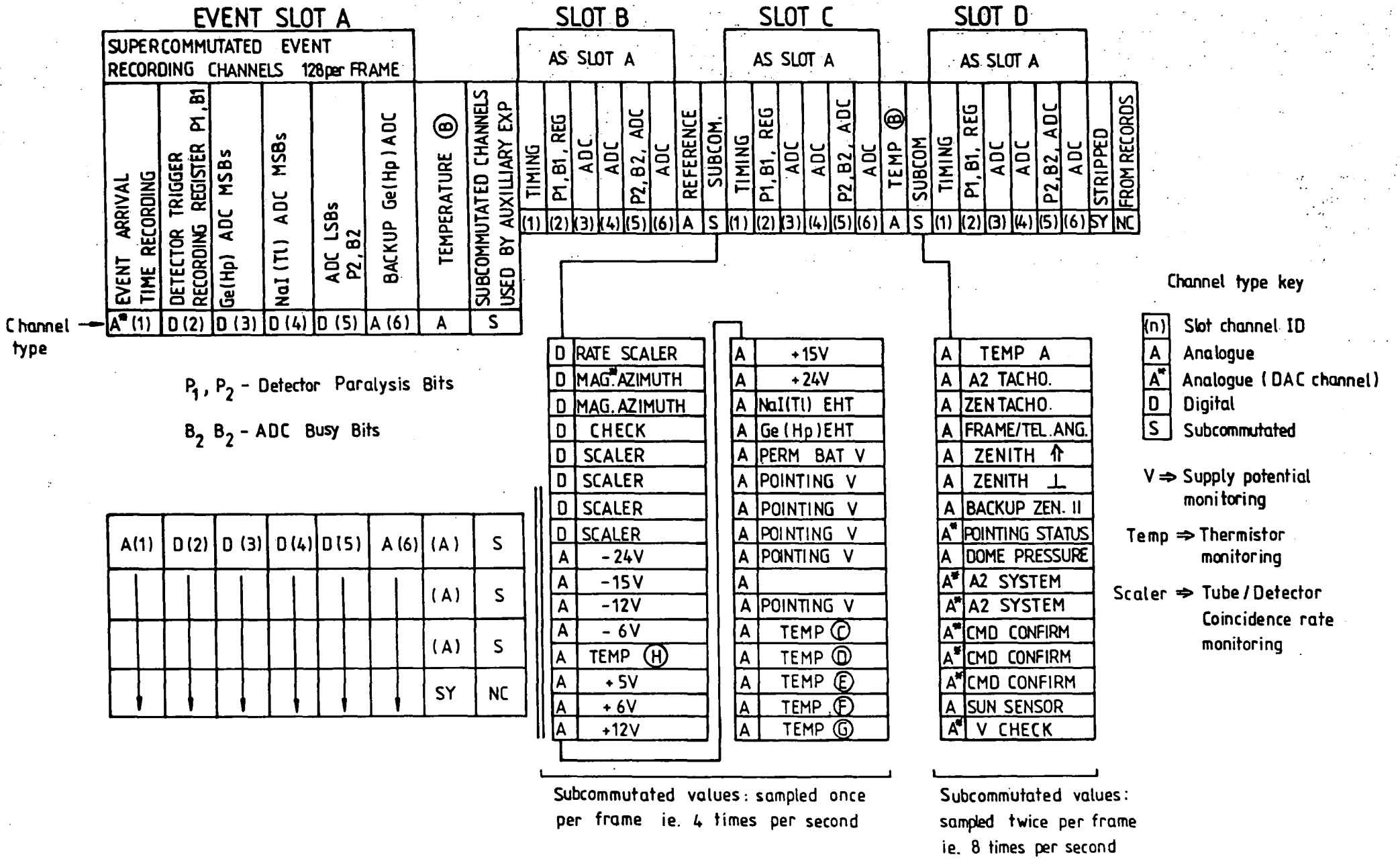

Figure 3.9 The Durham experiment's telemetry format.

The two basic repetitive cycles can be termed the subcommutation cycle and supercommutation cycle. A subframe consists of 32 words and forms the main repetition cycle (the subcommutation cycle). The process of data collection by this "subcommutation cycle" allows some of the words to be arranged to sample different quantities in the successive subframes. A frame is made up of 32 such subframes i.e. in a frame there are a total of 1024 words. A frame is transmitted every 0.25s, hence 244 μs per word.

In addition, the Durham telemetry formats repeats along each of the 32 subframes, these are divided into units of eight words, the first six of which are identical in all four cases, this forms the supercommutation cycle. The remaining two words in each unit are used for subcommutated information or are less frequently sampled or, in the case of the last two words in each frame, contain the frame synchronization code.

Therefore, in each complete frame of 1024 words there are 128 repeated samplings of the same six quantities. Each of these units is a slot which can contain a description of an event. An event is the consequence of a Ge(Hp) trigger and the system must not be paralysed (ie. "live") for the event to be accepted. The six words include the measure of the detected pulse height from the Ge(Hp) and that from one of the shield elements, if any. Also contained in these words are the timing information, independent "backup" recording of the Ge(Hp) pulse-height and an event register

specifying which detectors have fired.

3.3.1.1 Main ADC System -

A gamma-ray entering the Ge(Hp) detector generates a signal and the pulse height is analysed using an Analogic MP 8014 14-bit ADC (Analogue to Digital Converter). The transmission and subsequent recording of these 14 bits extends over several words on the data tape, and the energy deposited in Ge(Hp) is divided amongst 16384 energy channels. Inputs to the ADC unit are selected by Analogic MN4708 analogue multiplexers from one of two SHM60 Burr-Brown sample-hold units. One of these 'holds' the first Ge(Hp) pulse which arrived since the last ADC reset pulse. The ADC reset pulse is derived from the telemetry system and the state of completion of the last analysis; the timing of which is locked into the main supercommutated sampling cycle.

The other sample-hold module contains either the summed pulse heights from all the photomultipliers on a particular detector which fired in coincidence with the Ge(Hp) or, in the absence of any shield piece being triggered, the summed output from all the shield detectors other than A0. The voltages from the two sample-hold modules are analysed in turn and the output digital words are entered into the telemetry frame.

3.3.1.2 Pulsar Clock -

This consists of a 6-bit scaler clocked by a quartz crystal oscillator. The 6-bit scaler produces a digital word of 6 bits, and counts from Ø to 63. The device is reset after being read in the A1 word. The arrival of an event causes the scaler value to be latched at that instant, This value is then read out at the next A1 read. Or if there is no real event, the scaler is reset to zero before over ranging and starts again.

In order to transmit the scaler information the digital word is converted into an analogue pulse because there are only a limited number of digital lines available for input to the CIP, and these are used up by the transmission of other digital data. The conversion is done by feeding the 6-bit D (Digital) pulse into the 6 MSBs (Most Significant Bits) of a 1Ø-bit DAC. The information transmitted to the ground receiving station is stored as a 1Ø-bit digital word on tape in the range Ø to 1Ø23. The values stored on tape are analysed to give the original integer time values in the range Ø to 63 (max). This is explained in chapter 4 where the analysis of the data is discussed.

3.4 The Pointing System

In order that gamma-rays from a specific direction can be studied the apparatus must be capable of being pointed in a known direction. The Durham spectrometer pointing system employed an alt-azimuthal mounting in which two angles,

zenith and azimuth, were used to define the pointing direction. The zenith angle was varied by tilting the spectrometer and pressure dome about a horizontal axis. The zenith drive was a DC motor, the output torque was transmitted through a worm reduction gear and tilted the pressure dome by driving its central horizontal spindle with respect to the main rectangular frame of the gondola (See Figure 3.7). The angle of the spectrometer with respect to the zenith was monitored by four sensors:

(i) a 60 degree range inclinometer operating in the plane of the zenith angle;

(ii) a 4 degree range inclinometer operating perpendicular to the plane of the zenith angle;

(iii) a backup geared pendulum and potentiometer unit operating in the plane of the zenith angle;

(iv) a transducer to measure the angle between the gondola frame and the spectrometer axis.

An error signal derived from the comparison of the required angle and the digitised output from the 60 degree inclinometer was used to control the zenith drive motor. In order to check whether the required angle had been obtained a sub-system, independent of the main system, consisting of two perpendicular geared pendulums was used to monitor the spectrometer altitude angle to approximately 0.2°.

The azimuthal angle of the spectrometer was changed by rotating the entire gondola. The mechanism involved an inertial reaction wheel which was driven by a direct-drive motor. This unit was mounted above the environmental dome

on the top branch of the rectangular frame (see Figure 3.7). The four corners of the gondola were attached to the balloon through double swivels. Torsion relief was provided by driving one swivel with respect to the other by a geared stepper motor at a rate controlled by pulses from an optical encoder on the reaction wheel.

The azimuthal automatic drive control signal was derived from a pair of opposed fluxgate magnetometers which were mounted on a rotary table. The table was revolved by a reduction-geared small stepper motor at the other end of a one meter shaft. This long shaft essentially magnetically isolated the magnetometers from the stepper motor and ferromagnetic materials in the gondola. The orientation of the table was sensed by an absolute encoding system, and it could be adjusted using digital comparison to an accuracy of 10.5 arc minutes in accordance with a transmitted demand angle.

The processed output from the magnetometers was used to control the azimuthal drive. Effectively, the gondola was rotated until a stable null signal was produced at the magnetometer output; the opposed magnetometers would then be aligned along the Earth's magnetic field. Thus by rotating the magnetometer table it was possible to arrange the spectrometer axis to point in any azimuthal direction. The working of the azimuthal pointing system was monitored by two orthogonal pairs of magnetometers. The signals were processed by a digital resolver which measured the azimuthal

pointing direction to approximately Ø.1°.

3.5 Performance Of The Balloon Flight

The flight took place on the morning of the 6th June 1981 in Palestine, Texas, U.S.A. using a balloon of size 433,488 m^3. It was launched at 12.35.23 UT (7.35.23 local time) with an ascent rate of 4.68 ms^{-1} and reached float altitude (~ 36.58 km) at 14.26.Ø UT. The Crab observation was from 17.Ø1.ØØ UT to 21.5Ø.ØØ UT and the Crab was at transit at 19.Ø5.ØØ UT. After a total observing period of 23.4 hrs the flight was terminated at 1Ø.55.ØØ UT. On-line monitoring showed that all systems performed well apart from short periods of hardware failure and bad signal reception.

The internal dome temperatures remained within a few degrees of 2Ø °C. and pressure to within 25 mBar of the nominal pressure of 1 Bar. The steering system proved to be accurate to within 1/4 deg, and the environmental dome functioned as expected. The hardware failure mentioned concerned the occasional non-resetting of the paralysis of the data acquisition system. Immediately such a fault was noticed it was corrected manually by the transmission of suitable commands to the payload.

CHAPTER 4

DATA ANALYSIS AND RESULTS

4.1 Data Conversion

After a successful ballon flight, the raw data that have been recorded on a series of analogue magnetic tapes are converted into a form upon which direct computer analysis can be performed. This process filters out all the information which are not of direct scientific interest. Although a wealth of data is recorded during the flight, only a small amount of it is actually used in the data analysis. The relevant data include:

(i) the heights of the pulses emanating from the detectors in the spectrometer (from which the count rate is obtained);

(ii) timing information;

(iii) the telescope pointing directions;

(iv) the geographical positions of the balloon.

The process of reading the data tapes, cataloguing the channel numbers and times is complicated by anomalies in the data. These are caused by telemetry dropouts and instrumental malfunctions as mentioned in the last chapter. Some data frames have been corrupted and are recorded onto tapes along with the valid data by the recording system. Though validation programs have been written which can handle many of the errors, some require direct, manual

intervention in order to interpret and circumvent the problem in the most reasonable fashion. This is essentially a two-stage procedure. Firstly, simple checks are carried out to remove the obvious corrupt frames. Secondly, using both the temperature and system voltage as monitors further corrupt frames are checked. It is found that those frames containing unrealistic values of temperature and voltage are corrupt and hence should be rejected. This procedure of examining the data produced as a result small gaps in the data stream (see Figure 4.1).

The early stages of data reduction were carried out on an IBM 370/168 computer of the NUMAC (Northumbrian Universities Multiple Access Computer) system. Later it was transferred to a DEC VAX 11/750 computer of the SERC Starlink network when the Durham node was commissioned. The data analysis described here, except part of the line feature search, was performed using the VAX 11/750 computer.

4.2 Search For Line Features

4.2.1 On And Off Source Spectra -

Angular resolution of a source and consequently the definition of both the 'on source' and 'off source' events from that source are very much dependent on how the acceptance angle of the telescope is defined. The Durham spectrometer acceptance factor is defined as:

$$S\Omega \quad cm^2 sr = \int_0^{\theta_M} A_{Eff} \; 2\pi \sin\theta \, d\theta$$

This is a general not specific formula

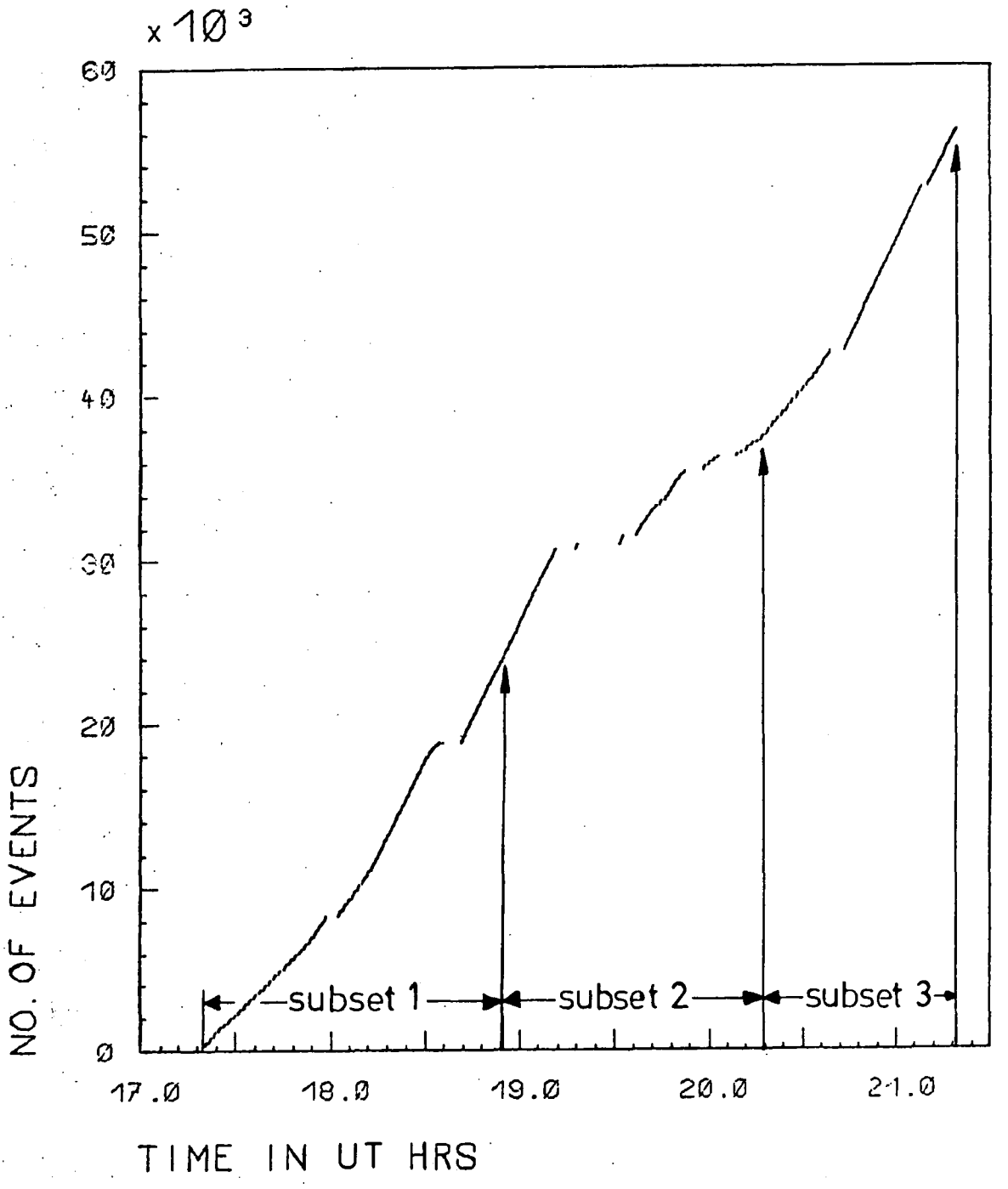

Figure 4.1 The graph of the number of events plotted against time.

where A_{Eff} is the effective area of the telescope and θ_M is the maximum angle off the telescope axis which photons reaching the Germanium detector can have. θ_M is dependent on energy, as the transparency of NaI crystal to photons increases with energy over the energy range studied by the spectrometer. The value of the acceptance angle at full width half maximum (FWHM) θ_{FWHM} varies from 4.9° at 50 keV to 5.36° at 10 MeV. Both the acceptance angle at FWHM and acceptance factor of the spectrometer as a function of energy are shown in Figure 4.2. The spectrometer acceptance is a maximum when its axis is aligned with the source direction and decreases as the angle between the spectrometer axis and source direction increases. With the assumption that the shield is totally opaque to all gamma-rays, a geometrical acceptance angle can be defined which has a value of 4.78° (FWHM). 'On-source' measurements are defined as those events that have been collected when the alignment between the source direction and spectrometer axis is < 2.39°. 'Off-source' measurements are defined to be those events detected when the miss alignment between the two axes is more than 2 x 2.39° and generally less than 8°. The 'on source' events referred to are the total number of photons from the Crab direction plus the background ('off-source' measurements) that is superimposed upon it.

The observation on the Crab provided a total 'on-source' exposure factor of 53673 cm^2 s with an 'on-source' time of 4340.5 s and 'off-source' time 3808.25 s. The energy spectra for both 'on-source' and

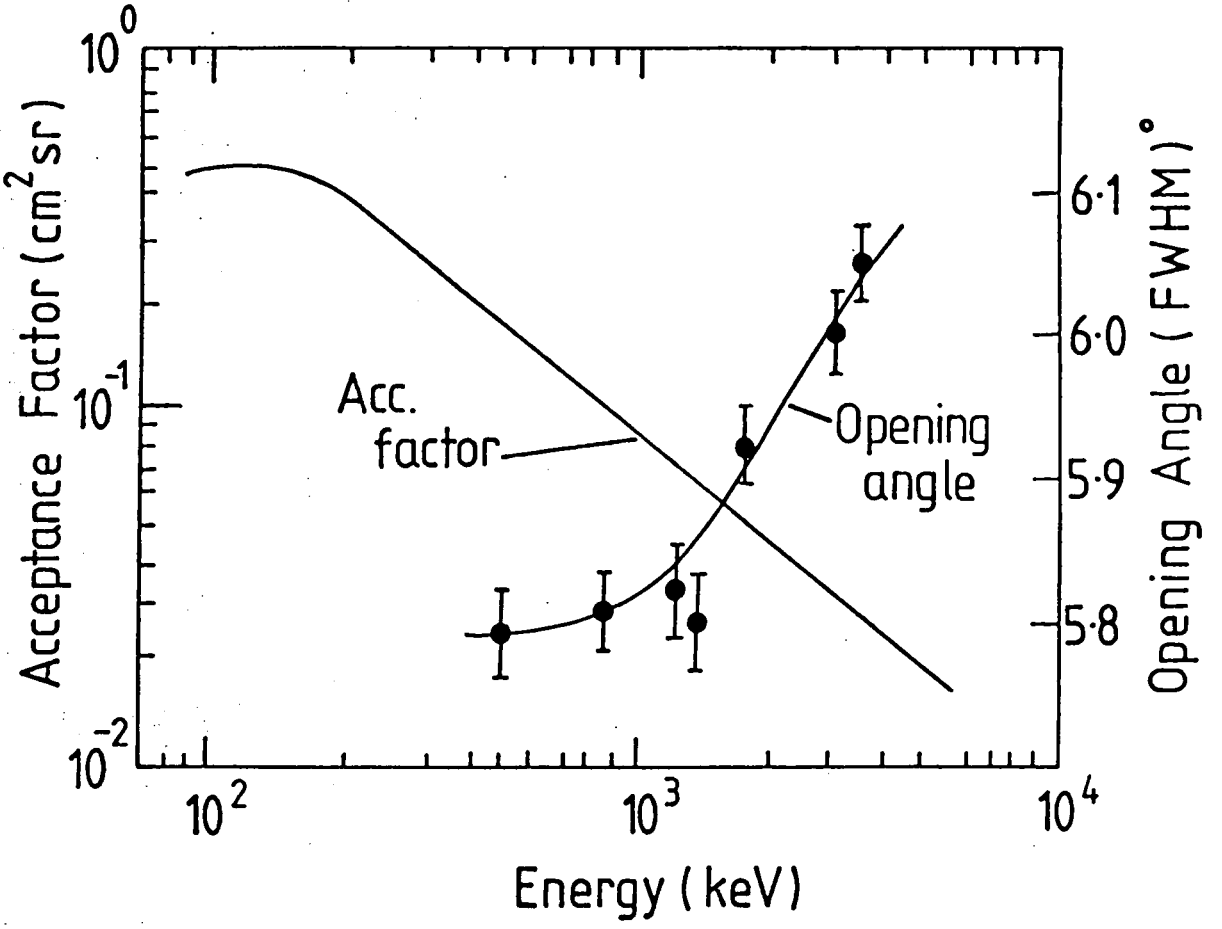

Figure 4.2 The geometrical acceptance factor and the angular acceptance (FWHM) of the spectrometer.

'off-source' are shown in Figure 4.3a and Figure 4.3b. Some of the prominent background lines can be clearly seen on both figures. These have been identified and are tabulated in Table 4.1 together with a possible origin for the lines. The studies of these background lines in the spectra corresponding to different periods of the Crab observation indicate that the drift in the energy calibration of the spectrometer is less than 0.2 keV.

4.2.2 Search Techniques -

The technique employed in the search for line features essentially involved the subtraction of the background counts from the total count rate, and calculating the significance of the excess counts above background. The subtraction was carried out on a channel by channel basis after correcting for the different observation times. The spectrum from the Crab Nebula region resulting from this subtraction was then searched for line features. A computer program was devised to identify line features that departed from zero flux with a significance in excess of 3 standard deviations. The criteria for a feature to be significant was based on a formula derived by Li and Ma (1983) for the hypothesis of zero source counts. The significance, S, of a feature was given as: $S = \sqrt{-2 \ln\lambda}$

where $$\lambda = \left\{\frac{f}{1+f}\left(1 + \frac{N_{off}}{N_{on}}\right)\right\}^{N_{on}} x \left\{\frac{1}{1+f}\left(1 + \frac{N_{on}}{N_{off}}\right)\right\}^{N_{off}}$$

Here N_{on} is the number of 'on source' counts in time T_{on}

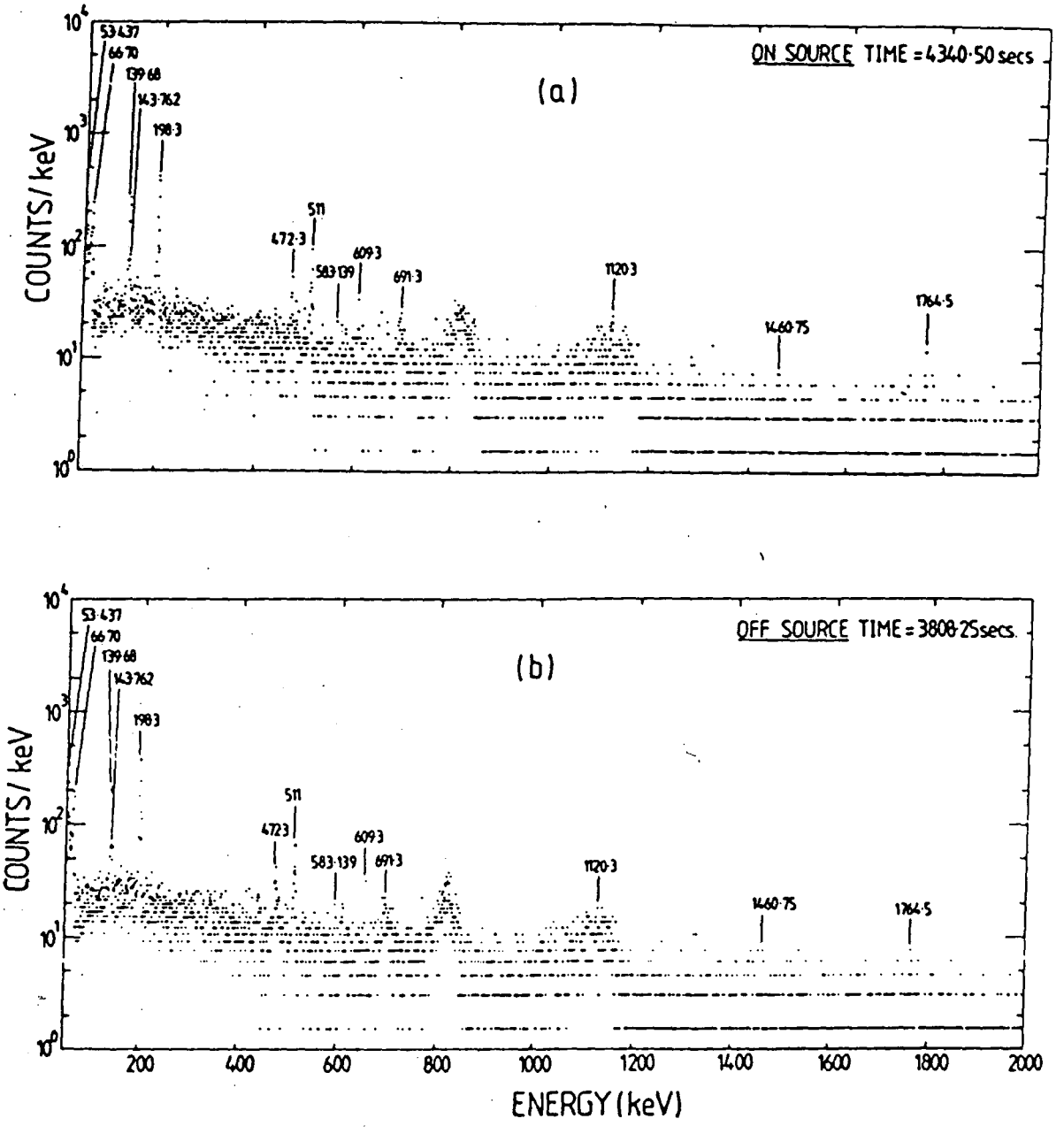

Figure 4.3 (a) The total energy spectrum - on source measurements,

(b) the energy spectrum for the background - off source measurements.

Table 4.1 The major backgroud lines observed during the Crab observation.

MEASURED ENERGY (keV)	TABULATED ENERGY (keV)	PARENT NUCLEUS	POSSIBLE ORIGIN
53.37	53.437	Ge^{73m}	$Ge^{72}(n,\gamma)Ge^{73m}$, $Ge^{74}(p,d)Ge^{73m}$, $Ge^{73}(p,p')Ge^{73m}$
66.53	66.70	Ge^{73m}	
139.64	139.68	Ge^{75m}	$Ge^{74}(n,\gamma)Ge^{75m}$, $Ge^{76}(n,2n)Ge^{75m}$
142.58	143.762	U^{235}	Nat U^{235} (Actinium Series)
198.11	198.3	Ge^{71}	$Ge^{70}(n,\gamma)Ge^{71}$, $Ge^{72}(p,d)Ge^{71}$
472.49	472.3	Na^{24m}	$Na^{23}(n,\gamma)Na^{24m}$, $Al^{27}(n,\alpha)$ Na^{24m}
510.50	511	e^+/e^-, Tl^{208}	Positron annihilation
582.89	583.139	Tl^{208}	Nat Th^{232} (Thorium Series)
609.51	609.3	Bi^{214}	Nat U^{238} (Uranium Series)
693.60	691.3	Ge^{72}	$Ge^{72}(n,n'\gamma)Ge^{72}$, $Ge^{72}(p,p')Ge^{72}$
1120.84	1120.3	Bi^{214}	Nat U^{238} (Uranium Series)
1460.84	1460.75	K^{40}	
1764.62	1764.5	Bi^{214}	Nat U^{238} (Uranium Series)

over the feature; N_{off} is the number of corresponding background counts in time T_{off}; and $f = T_{on}/T_{off}$. The search was conducted in the energy range from 50 keV to 2000 keV for all possible lines with $S > 3.0$.

4.2.3 Line Features From The Crab Nebula Region -

Several line features were observed; these were centred around energies 330.0 keV, 404.4 keV, 1049.6 keV, 1960 keV and 1977 keV. They are listed in Table 4.2 together with the number of 'on source' and 'off source' counts and also listed are the confidence levels, P_T^M, of the effects being real.

The calculation for the confidence level is dependent on the number of degrees of freedom that an individual search would be allowed, or in this instance the number of ADC channels over which the search is carried out. A random fluctuation in the background could have produced a peak centred on any one of these channels. If P_T is the probability that the effect is not due to a random fluctuation in the background at the observed channel, then after one has searched M channels the probability of finding that effect becomes P_T^M. For each candidate line the value of P_T is obtained from the area under the normal distribution for a given value of significance (Table 4.2).

Table 4.2 Candidate lines obtained during the total observing period on the Crab. Also listed are the number of degrees of freedom and confidence level associated with each line.

Energy of Feature (keV)	Number of Events: Source and Background (t_{on}=4340.5) sec	Number of Events: Background (t_{off}=3808.25) sec	Significance (No. of standard Deviations) at a specific energy	Probability of effect not due to a specific random fluctuation	Predicted range for peak (keV)	Number of degrees of freedom (M)	Confidence level (P_T^M) over M
328.7 - 331.3	73	31	3.5	0.999767	50-2000	2985	0.499
401.8 - 406.4	93	45	3.4	0.999663	395-405	14	0.995
					50-2000 †	2985	0.366
1044.6 - 1053.1	81	26	4.8	0.999999207	50-2000	2985	0.998
1954 - 1965	21	4	3.3	0.999517	50-2000	2985	0.236
1974 - 1980	12	1	3.1	0.999032	50-2000	2985	0.056
77.8 - 79.8*	32	11	4.1	0.9999793	70-80	14 x 3	0.999
					50-2000 †	2985 x 3	0.831

† Predicted range, number of degrees of freedom and confidence level when the line search is allowed to extend over the complete energy range.

* This line was seen only in the last subset of the date with t_{on}= 1571.75 sec and t_{off} = 2019.5 sec.

Four of the line features around energies 330.0 keV, 1049.6 keV, 1960 keV and 1977 keV observed in this experiment have not been seen previously. The number of degrees of freedom associated with any one of these searches is just the channel bandwidth over which the search has been carried out. As the line search was conducted in the energy range from 50 to 2000 keV which corresponded to 2985 ADC channels, there were 2985 degrees of freedom allocated to these lines.

For the 404.4 keV line feature, the number of degrees of freedom associated with the search can be reduced substantially if one takes into account previous experiments. As mentioned in chapter 2 there had been two reports of a line feature close to this energy region. Leventhal et al. (1977) reported a feature at (400±1) keV with a 4 σ deviation above the continuum and Yoshimori et al. (1979) also observed a similar feature at 400 keV from a set of data obtained on the Crab but with only a 1.4 σ significance. Assuming that the present result confirms that of Leventhal et al., with the difference in energy of the feature caused by variation of the source, then the number of degrees of freedom can be reduced considerable from the 2985 mentioned above. The search for the 400 keV line was confined to an energy interval of 10 keV centred on 400 keV. This energy bandwith corresponded to 14 ADC channels and therefore the number of degrees of freedom was reduced to 14, the corresponding confidence level increasing to 0.995. If no previous experimental measurements were

taken into account the number of degrees of freedom would have been 2985 and the confidence level 0.366 (see Table 4.2).

From the calculated confidence level for each of these candidate lines, it seems that only two of them can be regarded as significant; the line features at 404.4 and 1049.6 keV. The fluxes of these lines at the top of the atmosphere, after correcting for efficiency, dead time and absorption in the material and air above the detector, are $(7.2 \pm 2.1) \times 10^{-3}$ photons cm^{-2} s^{-1} at 404.4 keV and $(1.9 \pm 0.4) \times 10^{-3}$ photons cm^{-2} s^{-1} at 1049.6 keV with widths (FWHM) of 3.2 keV and 5.9 keV respectively including the experimental resolution. The other lines obtained in the search cannot be counted as significant, unless some other experiments can provide a confirmation of these lines.

4.2.4 Gamma-ray Line Transients -

In order to investigate whether the intensity of any one of the line features in the Crab spectrum varied with time, the total data on observing the Crab were divided into three subsets each with nearly equal on and off-source observation times as indicated in Figure 4.1. These three subsets of data were searched separately for lines of high significance using the same computer line search technique as for the whole data set. One feature at an energy of 78.9 keV was found in the final subset of the data with a significance of 4.1σ and a width (FWHM) of 1.4 keV

including the experimental resolution. The properties of this line have been listed at the bottom of Table 4.2 so that comparison may be made with the other candidate lines.

As mentioned before, various experiments, Ling et al. (1979), Manchanda et al. (1982), and Strickman et al. (1982), reported a line feature in the spectrum from the Crab Nebula at energies around 73 and 77 keV. Hence when calculating the confidence level for this line feature an energy interval of 10 keV (i.e. 14 ADC channels) centred on 75 keV was considered. Since three different subsets of the data had been searched the number of degrees of freedom was increased from 14 to 42 and resulted in a confidence level of 0.999 for the line. If previous experimental observations in the 73-77 keV region were ignored, the number of degrees of freedom associated with the search would have been 8955 (i.e.2985x3) and the confidence level reduced to 0.831 (see Table 4.2).

The effect was only observed in the final subset of the data, thus implying that this was a transient effect. The variation of the intensity incident at the top of the atmosphere with time is shown in Figure 4.4 together with the other two observed features at 404.4 keV and 1049.6 keV for comparison. The dashed region on each graph indicates the mean rate and error over the observation period. It can be clearly seen that the intensity of the 78.9 keV line feature increases with time during the observation period. The other two features remain consistent with the mean rate

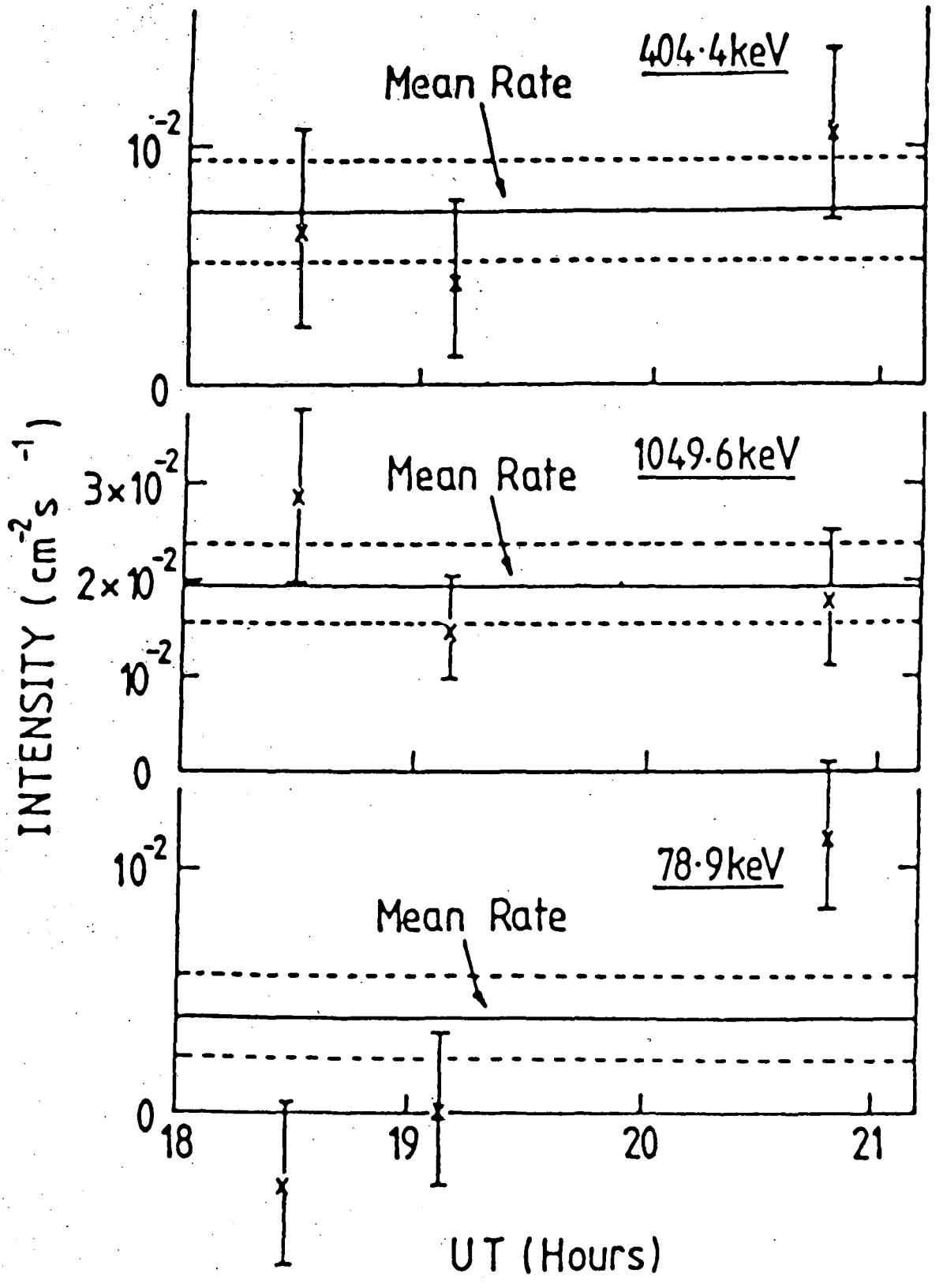

Figure 4.4 Variation in the intensity of the 78.9, 404.4 and 1049.6 keV line features during the observation period.

throughout the entire observation. Although the whole data set could have been divided into smaller time periods than the ones chosen, this was limited by the smaller number of counts detected for smaller energy intervals and the calculation would have resulted in larger statistical errors in the measured rate.

The profiles of the three line features observed in this experiment are shown in Figure 4.5. These are the excess counts (after background subtraction) plotted against photon energy. The width of the individual line feature is indicated by arrows as determined by the computer search technique.

4.2.5 The Crab Total Emission Spectrum -

The Crab total emission spectrum was obtained after subtraction of the background from the source over the whole period of observation on the Crab. This result is shown in Figure 4.6 together with results obtained by other experimenters in the energy region 60 keV to 340 keV. Due to the small statistics no corrections have been made for the lines at 78.9 and 404.4 keV, their intensities have simply been incorporated in the energy bin containing the lines. The result of the Durham experiment is in good agreement with previous experiments in this energy region.

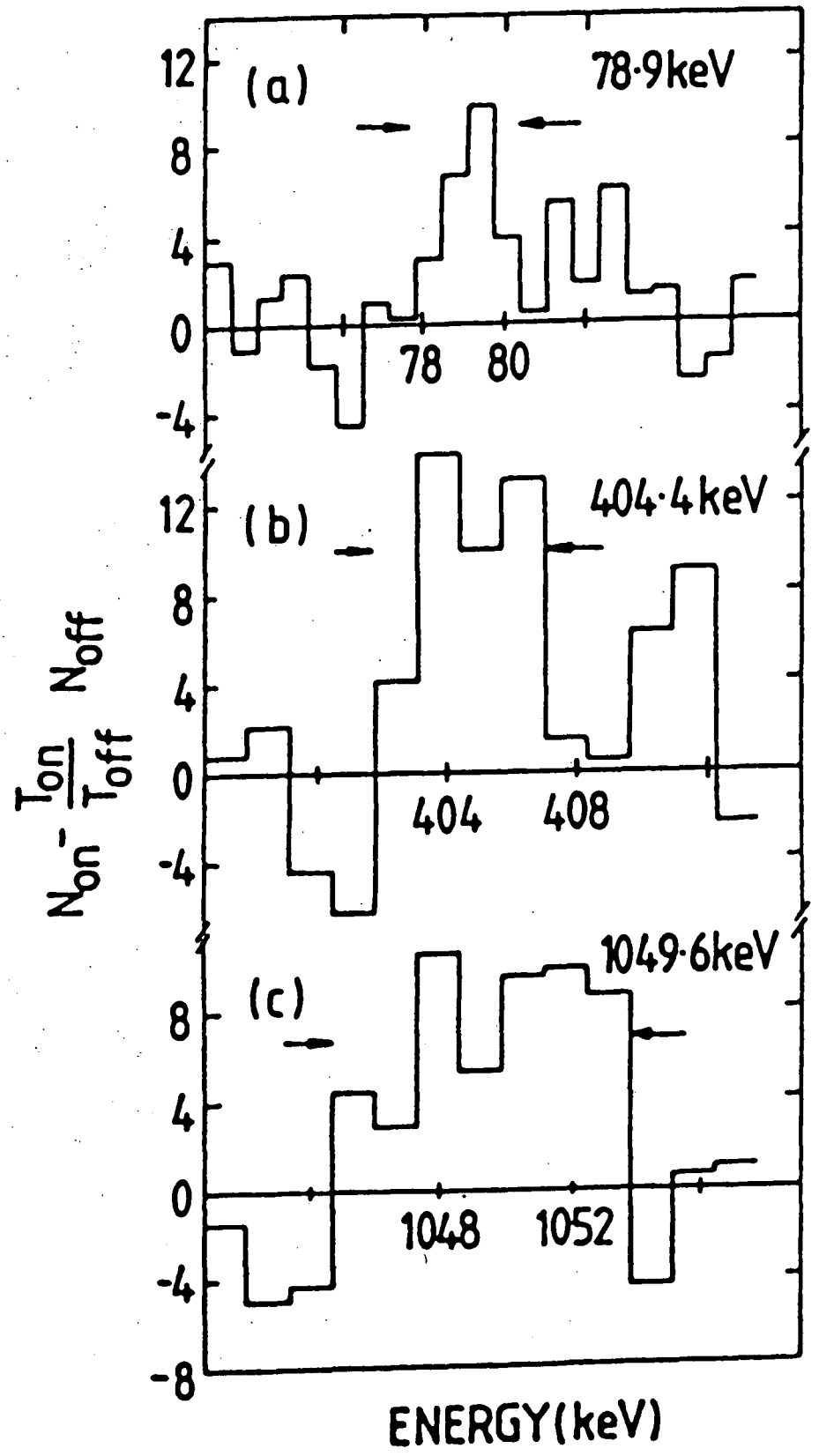

Figure 4.5 Line profiles of the three line features after correcting for the background.

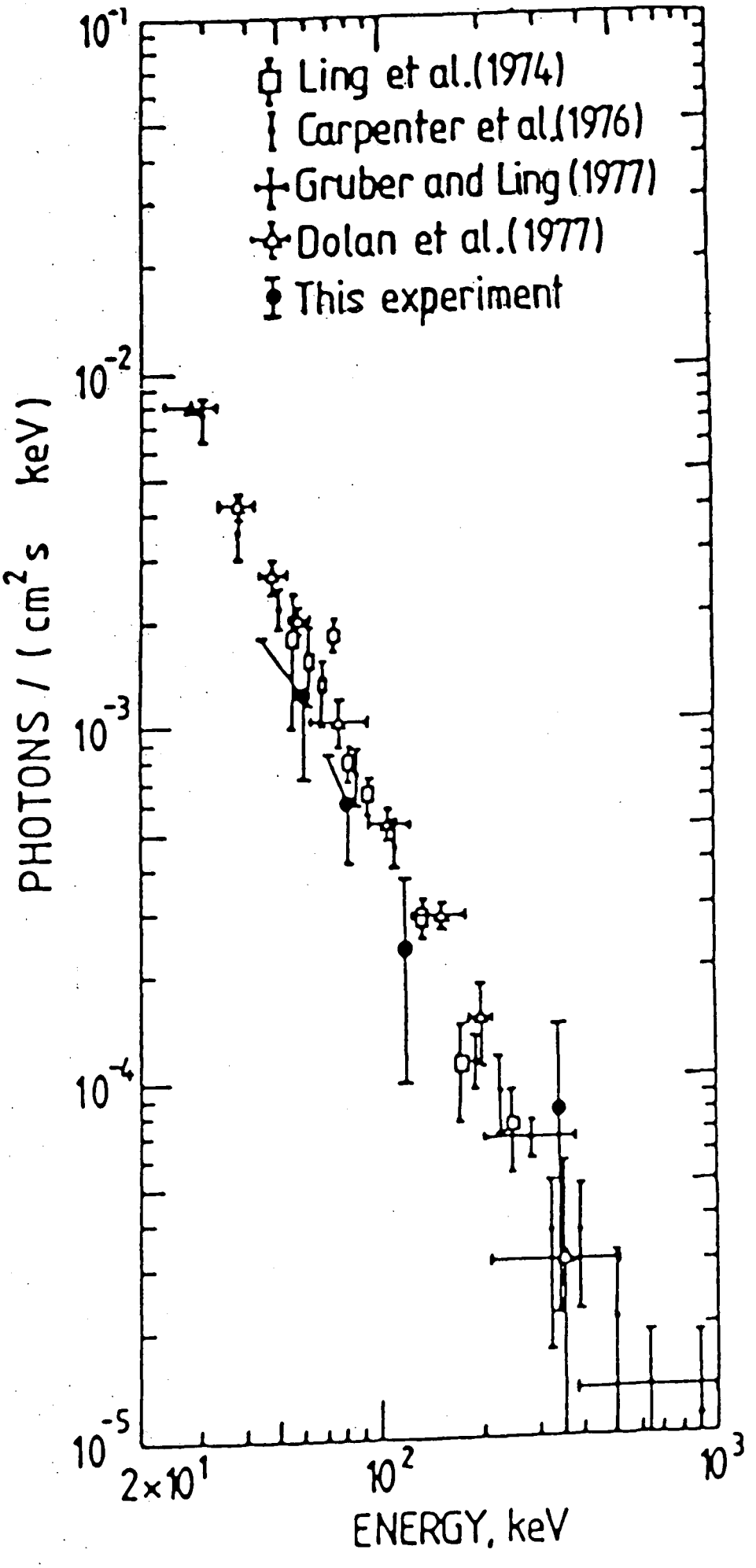

Figure 4.6 The continuum spectrum from the Crab Nebula between 20 and 1000 keV.

4.3 Search For Pulsed Emission

4.3.1 Pulsar Clock Calibration -

As mentioned in the last chapter due to the limited number of digital lines available from the CIP for data transmission it was necessary to convert some digital values into analogue values. The Pulsar Clock was such a quantity. These equivalent analogue values were recorded onto tapes and distributed from Ø to 1Ø23. In order to obtain the true times as measured by Pulsar Clock, it is necessary to convert these analogue values between Ø and 1Ø23 back into the original digital values ranging from Ø to 63. Figure 4.7 shows two regions of the distribution of the recorded Pulsar Clock values as obtained from the raw data on tape. The two regions shown correspond to the start of the range, ADC channels Ø to 2ØØ, and to the end of the range, 8ØØ to 1Ø23. As can be seen the data are distributed in such a way that successive values of the time are well resolved. As an illustration, for each event having an ADC value of between 842 and 858 a value for the Pulsar Clock of 55 would be assigned. The resulting distribution of the Pulsar Clock after dividing and grouping, which represents the original values recorded by the 6-bit scaler, is shown in Figure 4.8. In this analysis a sample of 5ØØ frames was considered.

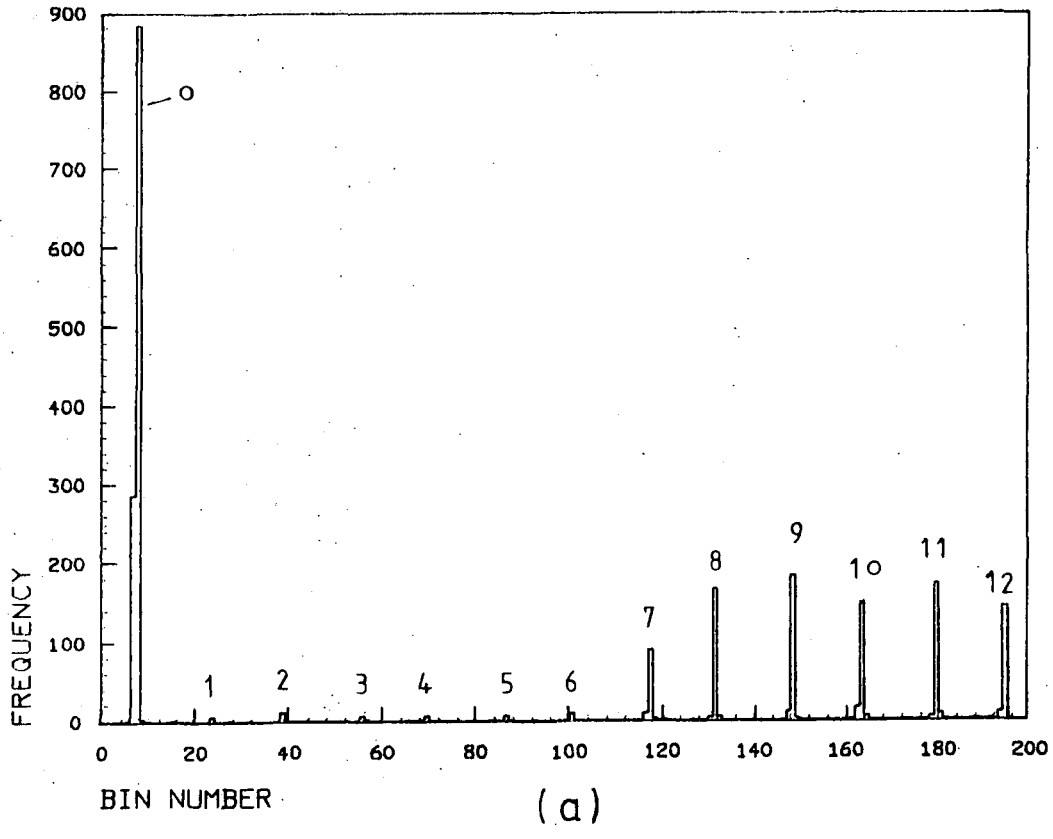

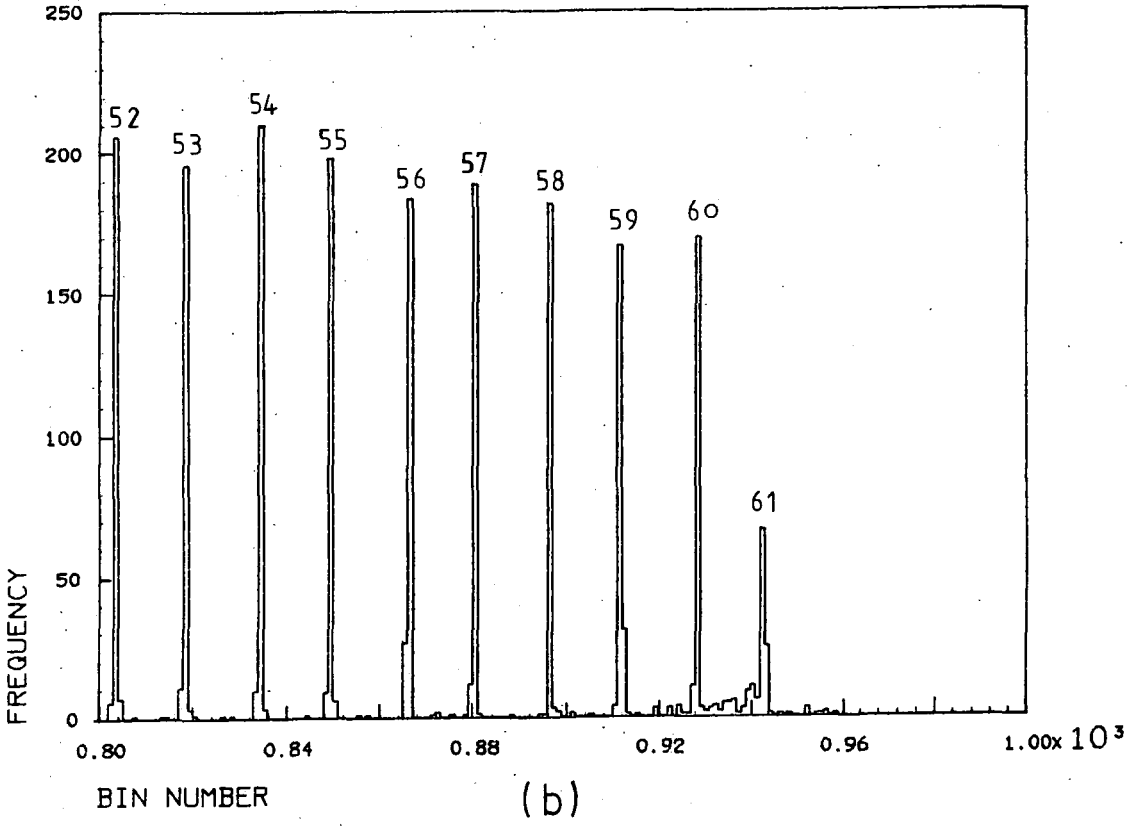

Figure 4.7(a,b) Showing distribution of the Pulsar Clock as obtained from the raw data on tape, the numbers above the peaks are the original integer time values recorded by the 6-bit scaler.

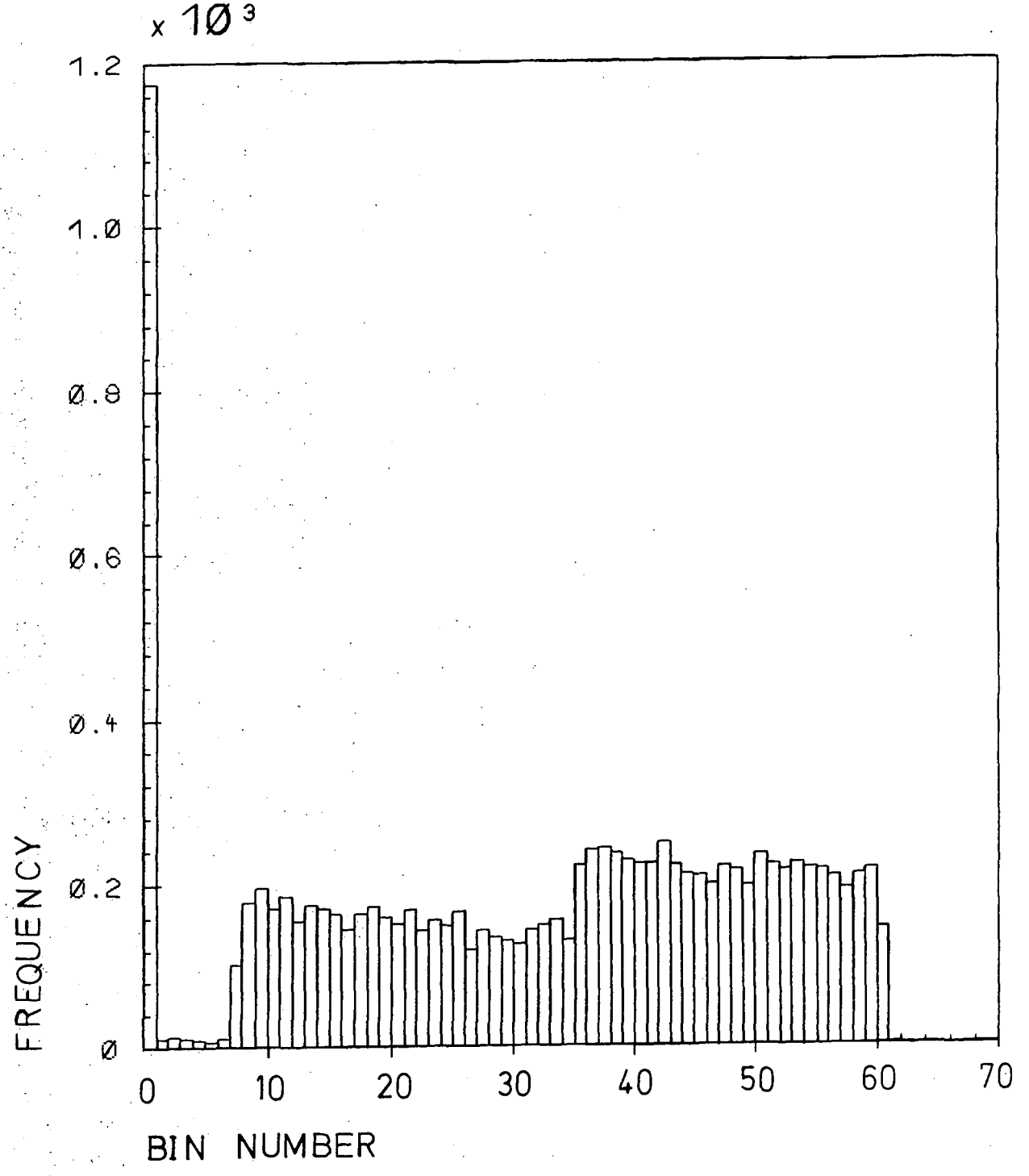

Figure 4.8 Distribution of the Pulsar Clock as recorded by the 6-bit scaler.

It can be seen from Figure 4.8 that only 61 bins were present out of a total of 64 bins available. The Pulsar Clock values are shown to peak at about half range which corresponds to the main ADC reset. The exponential fall in the rate is expected; this is due to the increased probability of the system being paralysed. It also can be seen that some of the lower bin values are missing and have been recorded as zeroes. This is caused by events arriving after the Pulsar Clock reset but before the recording of the paralysis bit P1. This will only increase the noise component in the temporal analysis and will not cause actual timing errors, and hence can be safely disregarded.

As the length of a frame is Ø.25s there are 128 positions (slots) an event can have within the frame. Therefore the time elapsed since the start of a frame is given by the position (POS) of the event multiplied by a factor of Ø.25/128 = 1.9531ms. The 6-bit scaler (Pulsar Clock) is a refined measure of the time within the slot. Since there are 61 places the event can have within a slot, the time is given by the position within the slot multiplied by a factor of 1.9531ms/61 = 32.Ø µs. The time of an event is then given by:

$$t_r = T_F + POS \times 1.9531\ ms + PSR \times 32.Ø\ \mu s$$

Where t_r is the arrival time of an event;

T_F is the time recorded at the start of a frame;

POS is the position of an event within a frame;

PSR is the Pulsar Clock value (recorded as any one

bit pattern of the 6-bit scaler).

4.3.2 Techniques And Methods Of The Search -

In order to determine if a periodic pulsation of small magnitude relative to the total detector counting rate is present, the arrival times are analysed using the epoch folding technique. Under the epoch folding technique the data are folded into a number of phase bins over a series of trial periods centred on the expected value, the resulting light curves are examined for uniformity by the Chi-square (χ^2) method. There are two major complications to this technique of analysis:

(1) The detector is moving with respect to the pulsar during the observation.

(2) The pulsar periods are not constant over typical observational intervals (even a few hours), it is lengthening all the time.

The first problem can be solved by mapping the photon arrival times at the detector to their arrival times at a common point. The second problem requires that a variable period be used to fold the data. The details of this mapping are discussed below followed by a discussion of the folding process.

4.3.3 Arrival Time Corrections -

The movement of the detector with respect to the pulsar introduces variable photon arrival times and there is essentially one significant correction which needs to be applied before binning of the corrected arrival times using the pulsar pulsation parameters can be performed. This correction is a mapping of the arrival times of the gamma-rays at the balloon to arrival times at some plane perpendicular to the pulsar direction, i.e. a set distance from the pulsar in an inertial frame. This condition is equivalent to eliminating the variable Doppler shift due to the Earth and balloon motions. Thus, knowing the photon arrival times at a set distance from the pulsar in an inertial frame allows binning using the pulsar pulsation parameters without regard to the motions of the detector with respect to the pulsar. A plane passing through the Solar System barycentre which is used by radio astronomers seems to be most convenient and is as near to an "inertial" frame of reference as possible. The position of the Solar System barycentre depends on the orbital motion of the planets, mainly the massive planet Jupiter which is sufficiently large to place the barycentre outside the surface of the Sun. The uncertainty in the position of the barycentre is caused by the large perturbations in the orbit of the small planet Pluto which makes this only an approximate centre of inertia.

4.3.3.1 Barycentric Correction -

There are several reasons for this barycentric correction: (i) rotation of the Earth introduces a variable time delay up to the transit time over one Earth radius (Figure 4.9); (ii) the gravitational potential of the Earth differs from the potential at a large distance from the Sun and (iii) the effect due to the annual variation in the rate of the terrestial clock times resulting from changing time dilation as the Earth moves around its elliptical orbit needs correction.

The correction Δt applied to each photon's arrival time at the balloon (see Figure 4.10a) is given by:

$$\Delta t = t_B - t_b = (\underline{R}.\hat{\underline{n}})/c$$

where:

t_B = arrival time at the plane perpendicular to the source direction and passing through the Solar System barycentre;

t_b = photon arrival time at the balloon;

$\underline{R}$ = a vector from the Solar System barycentre to the balloon;

$\hat{\underline{n}}$ = a unit vector in the direction of the pulsar in the same coordinates as $\underline{R}$;

c = speed of light in the appropriate units.

For observations of duration more than a month, an extra correction term to the photon arrival times, Δt_{rel} , must be added. This is due to the variable gravitational

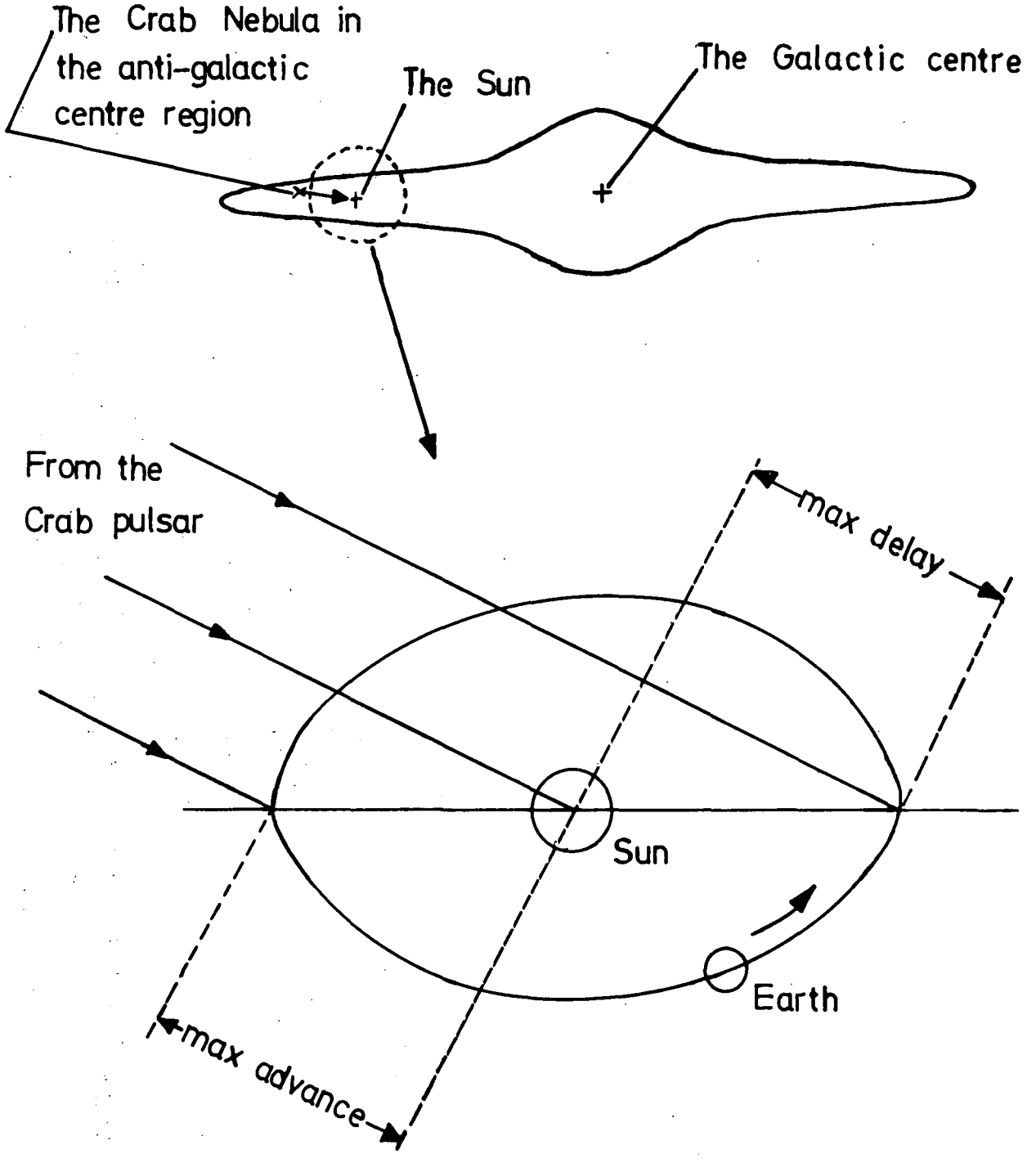

Figure 4.9 Diagrams showing the direction of the Crab pulsar signals and variation in pulse arrival time due to the Earth's orbital motion round the Sun.
(Partly adapted from Smith, F.G., 1977)

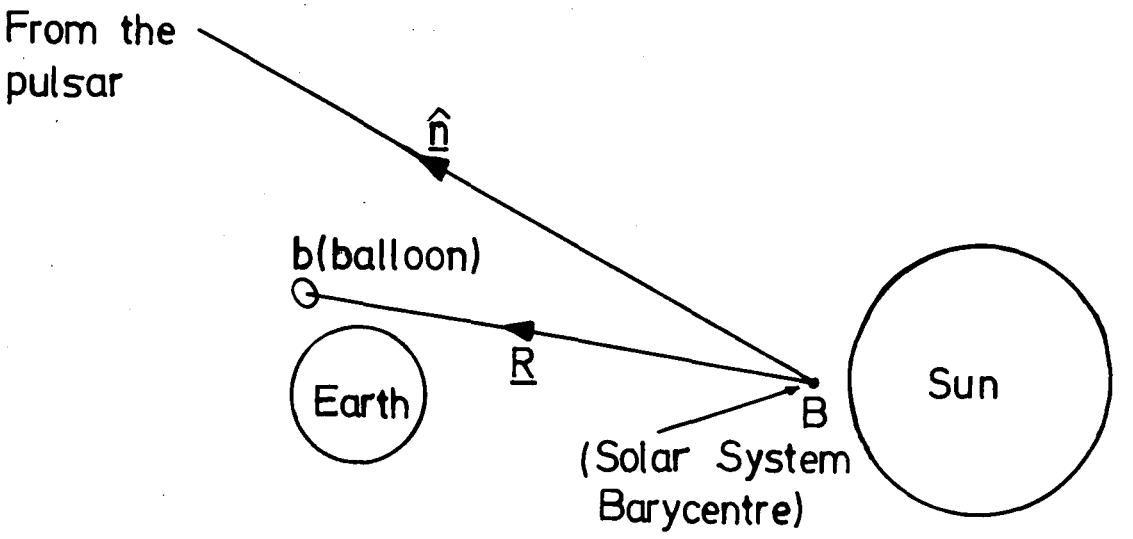

Figure 4.10 a The position vectors relating the pulsar to the balloon and barycentre.

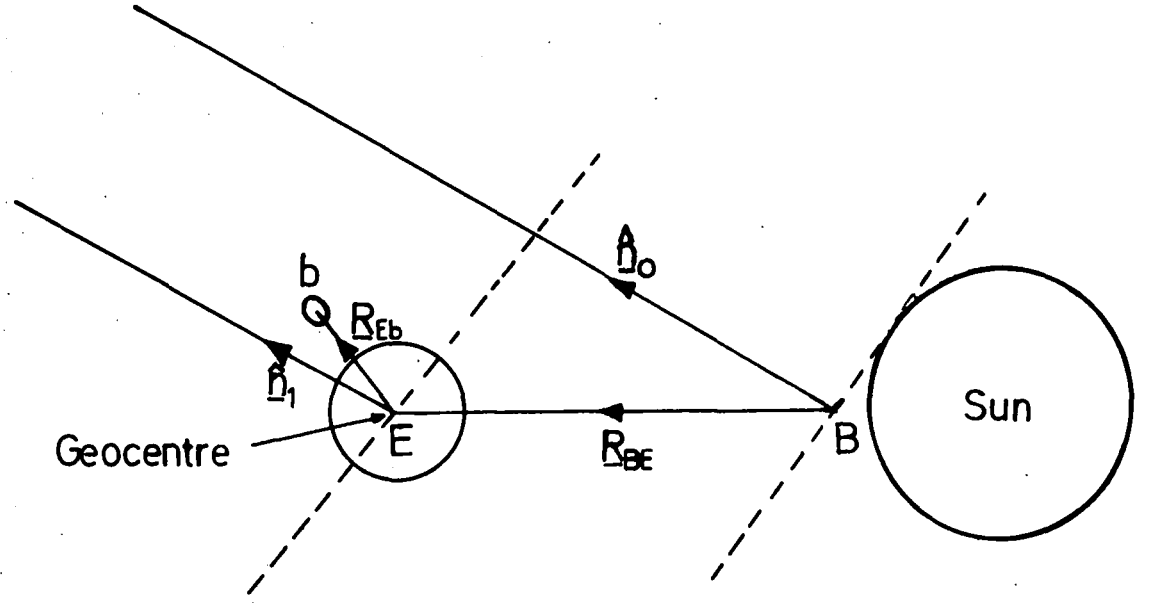

Figure 4.10 b Showing the various vectors used in arrival time corrections.

attraction of the Earth by the Sun in the Earth's eccentric orbit (reasons (ii) and (iii) above) which produces a general relativistic correction term given by:

$$\Delta t_{rel} = 0^{s}.001661 \left[\left(1 - 1/8\ e^{2} \right) \sin l + 1/2\ e \sin 2l + 3/8\ e^{2} \sin 3l \right]$$

where l and e are the mean anomally and eccentricity of the Earth's orbit respectively. (Manchester and Taylor, 1977, "Pulsars").

In order to find Δt, it is necessary to resolve Δt into two parts; one for the balloon position with respect to the Earth's centre (geocentre) and one for the Earth position with respect to the barycentre (see Figure 4.10b). Then the arrival time at the Solar System barycentre is:

$$t_B = t_b + \Delta t_{BE} + \Delta t_{Eb}$$
$$= t_b + \left(\underline{R}_{BE} \cdot \hat{\underline{n}}_o \right)/c + \left(\underline{R}_{Eb} \cdot \hat{\underline{n}}_1 \right)/c \qquad (4.1)$$

where:

$\underline{R}_{BE}$ = the position vector from the barycentre to the Earth's centre
(unit: Astronomical unit = 149600×10^{6} m
= $499.01184 \times c$ second
coordinates: barycentric rectangular; epoch:1950)

$\underline{R}_{Eb}$ = the position vector from the Earth's centre to balloon
(unit: m; coordinates: geocentric rectangular; epoch: epoch of observation)

$\hat{\underline{n}}_o$ = the unit vector in the pulsar direction

(unit: normalised to 1, no distance units; coord: equatorial; epoch: 1950)

$\hat{\underline{n}}_1$ = same as $\hat{\underline{n}}_o$ except, epoch: epoch of observation

The method used to calculate the $\underline{R}_{BE}$ during the observation intervals employed an interpolation of the coordinates of the Earth tabulated on pages B38-B52 of the Astronomical Almanac (1981). These are a set of rectangular coordinates origin at the Solar System barycentre and referred to the standard epoch of 1950.0. The interpolation incoporated a NAG Fortran Library routine E01ABF. This routine interpolates at a given point X from a table of function values evaluated at equidistant points, by Everett's formula. The values obtained from this method of interpolation were checked against the values obtained from a self-consistent set of subroutines developed by Stumpff (1979, 1980) and found to be consistent with one another.

Having found $\underline{R}_{BE}$ the projected distance in the direction of the pulsar can be found:

$$\underline{R}_{BE} \cdot \hat{\underline{n}}_o = (X_{BE} \cos\alpha_o \cos\delta_o + Y_{BE} \sin\alpha_o \cos\delta_o + Z_{BE} \sin\delta_o) \quad (4.2)$$

where α_o and δ_o are the equatorial coordinates of the Crab pulsar at the standard epoch 1950.0 (Table 4.3).

TABLE 4.3 Some of the Parameters used for Data Analysis

The Equatorial Coordinates of the Crab Pulsar:

Epoch	R.A.	Dec.
1950.0	5h 31m 31.46s	+ 21° 58′ 54″.8

(Ref:Minkowski, R. 1968)

The Geodetic Coordinates of Palestine:

Lat.	Long.	Height (above sea level)
31°.78333N	95°.7333W	422 ft

4.3.3.2 Correction For Balloon Drift -

The motion of the balloon away from the receiving station introduces a variable transmission delay and it can be compensated by calculating the clock drift. This is calculated by knowing the photon arrival times at the balloon. In order to know the photon arrival times at the balloon, it is necessary to obtain the distance between the balloon and receiving station (i.e. the range) throughout the flight. The range is easily obtained once the positions of the balloon and receiving station with respect to the geocentre are worked out (Figure 4.11). If $\underline{r}_{SE}$ is the position vector from the receiving station to the geocentre and $\underline{r}_{Eb}$ is the position vector from the geocentre to the balloon, then the range between the station and balloon can be represented by the vector $\underline{r}$ (Baker and Makemson, 1960).

where

$$\underline{r} = \underline{r}_{SE} + \underline{r}_{Eb}$$

Let

$$\xi = x_{SE} + x_{Eb}$$

$$\eta = y_{SE} + y_{Eb}$$

$$\zeta = z_{SE} + z_{Eb}$$

then

$$r = (\xi^2 + \eta^2 + \zeta^2)^{1/2}$$

The formulae for calculating the geocentric rectangular coordinates x,y,z from known geodetic coordinates h, λ, φ, (where h is the height of the place above the spheroid of reference and λ and φ are the longitude and latitude

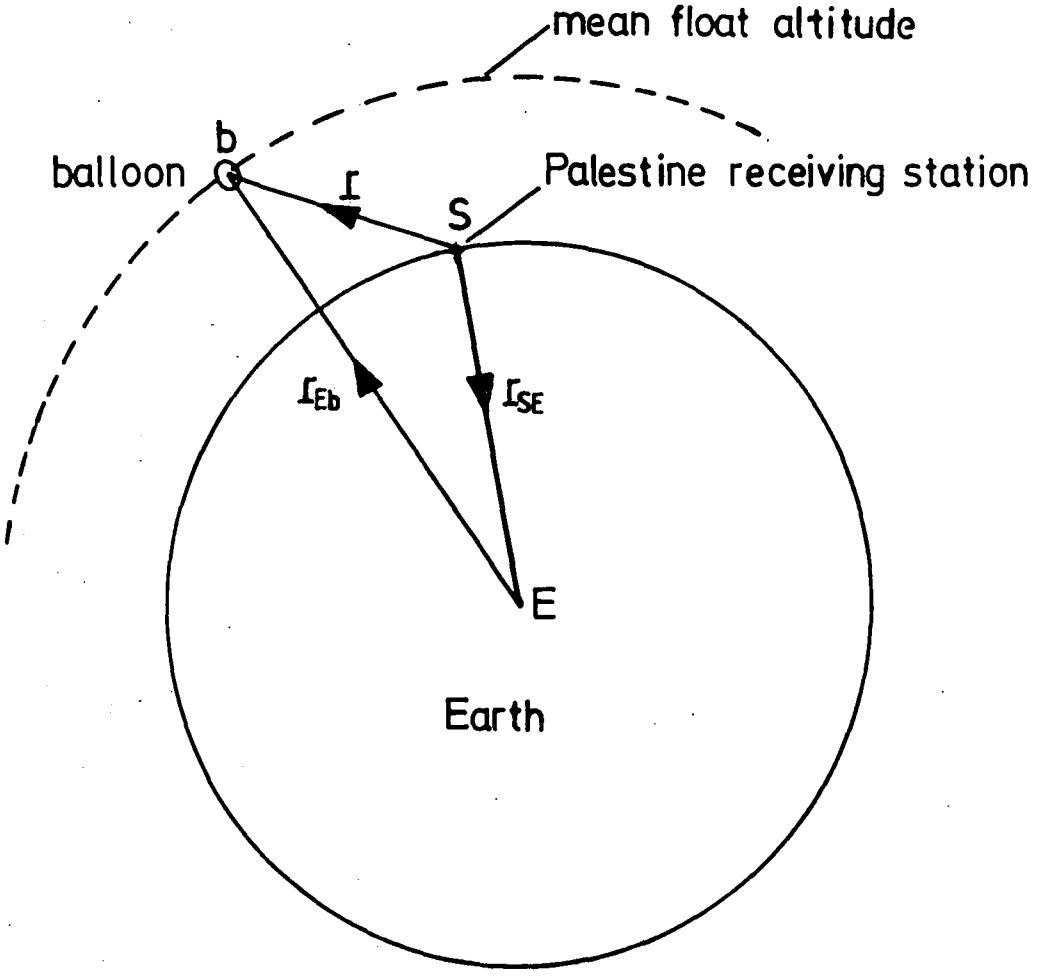

Figure 4.11 Position vectors defining the range

respectively) are given on p B55 of the Astronomical Almanac (1981) as below:

$$x = a(C + h/a)\cos\varphi\cos\lambda$$

$$y = a(C + h/a)\cos\varphi\sin\lambda$$

$$z = a(S + h/a)\sin\varphi$$

where $C = \{\cos^2\varphi + (1-f)^2\sin^2\varphi\}^{-1/2}$

$S = (1-f)^2\ C$

equatorial radius, $a = 6378\ 160$ m

flattening, $f = 1/298.2472 = 0.003\ 352\ 924$

The values for a and f are those defined for the international spheroid of reference (Internatioal Association of Geodesy, 1967). The geodetic coordinates for the receiving station at Palestine are tabulated in Table 4.3 and for the balloon, these are derived from the Omega navigation system and Rosemount altimeter.

Once r is known the photon arrival times at the balloon can be found:

$$t_b = t_r - r/c$$

where t_r is the recorded times at the ground receiving station and c is the speed of light.

By projecting the position vector of the balloon in the direction of the pulsar the extra path and thus the extra light travel time to the geocentre can be calculated. This is given as follows:

$$\underline{R}_{Eb} \cdot \hat{\underline{n}}_1 = (x_{Eb} \cos\alpha_1 \cos\delta_1 + y_{Eb} \sin\alpha_1 \cos\delta_1 + z_{Eb} \sin\delta_1) \qquad (4.3)$$

where α_1 and δ_1 are at the epoch of the observation.

Putting (4.3) and (4.2) in (4.1) the corrections of the photon arrival times at the barycentre are obtained and the folding process can then begin.

4.3.4 Epoch Folding Technique -

4.3.4.1 Binning The Data -

Since the pulsar period is not exactly constant, the corrected photon arrival times t_B are binned according to the pulsar phase Φ for the entire observational interval.

$$\Phi(t_B - t_o) = \int_{t_o}^{t_B} (P(t))^{-1} dt$$

where

t_o = reference time for (arbitrary or absolute) zero phase;

$P(t)$ = pulsar period calculated using the radio pulsation parameters.

Φ is the total phase or (real) number of periods which have elapsed between t_o and t_B. Its fractional part multiplied by an integer n gives a bin number for the photon arrival time t_B . In this way a light curve (pulse profile or phase histogram) of n bins is generated by folding with a test period. Since the period is not constant in time, phase as defined above is the quantity needed for binning. From the intrinsic properties of the pulsars; its pulsation

parameters can be represented by:

$$P(t) = P_o + \dot{P}(t - t_o) + \emptyset.5\ \ddot{P}\ (t - t_o)^2 + \ldots$$

where

P_o = the pulsar period at t_o

$\dot{P}$ = the 1st derivative of period with respect to time

$\ddot{P}$ = the 2nd derivative of period with respect to time

The parameter $\dot{P}$ is usually important in calculating phase even if $\ddot{P}$ is small enough not to contribute to Φ. To solve for Φ we assume

$$\dot{P}\ (t - t_o) << P_o$$

and that

$$\emptyset.5\ \ddot{P}\ (t - t_o)^2 << P_o$$

where $t_o < t < t_B$. For the Crab ($P \sim \emptyset.\emptyset33$ s, $\dot{P} \sim 4.2x1\emptyset^{-13}$ ss^{-1}, $\ddot{P} \sim -3x1\emptyset^{-24}$ ss^{-2})

$$\frac{P_o}{\dot{P}} \sim 8x1\emptyset^{10}\ s$$

and

$$\frac{2\ P_o}{\ddot{P}} \sim (2x1\emptyset^{11}\ s)^2$$

Therefore the assumptions are justified. Then, expanding the integrand by Taylor's series in $T = t_B - t_o$:

$$\Phi = \frac{T}{P_o} - \frac{1}{2}\frac{\dot{P}}{P_o^2}\ T^2 + \left(\frac{1}{3}\frac{\dot{P}^2}{P_o^3} - \frac{1}{6}\frac{\ddot{P}}{P_o^2}\right) T^3 + \ldots$$

Putting in some values for the Crab and $\Phi = \emptyset.\emptyset1$:

$$\emptyset.\emptyset1 \left(\frac{1}{2} \frac{\dot{P}}{P_o^2} \right)^{-1} \sim (7 \times 1\emptyset^3 \text{ s})^2$$

$$\emptyset.\emptyset1 \left(\frac{1}{3} \frac{\dot{P}^2}{P_o^3} - \frac{1}{6} \frac{\ddot{P}}{P_o^2} \right)^{-1} \sim (1\emptyset^6 \text{ s})^3$$

showing that the respective phase contributions are significant only for observation times greater than those given in the parentheses. The value $\emptyset.\emptyset1$ is chosen to avoid smearing at the level of $\emptyset.\emptyset1$ of a pulsar period.

It is usually necessary to test a number of periods close to the radio parameter values to obtain the best pulsar signal, $\dot{P}$ can be held fixed at the radio ephemeris value. The range of scanning for P with $\dot{P}$ at a fixed value is $\Delta P = P/n_P = P^2/T_{Obs}$ corresponding to a shift of one period for an event during the observation interval T_{Obs}. Where n_P is the total number of periods in the observation interval T_{Obs}. Following each test binning, a χ^2 test with the null hypothesis of equal number of photons per bin can be applied.

4.3.4.2 The χ^2 Test -

The χ^2 test is normally applied to find a function which best fits the experimental data. But in the analysis described here the test is being used to find the data which fits a function worst. The function in this case is the mean value. For a data stream in which the mean value of the number of counts per light curve bin N_i is $\langle N \rangle$, the χ^2

can be defined as:

$$\chi^2 = \sum_{i=1}^{n} \frac{(N_i - \langle N \rangle)}{\sigma_i^2}$$

where:

N_i = total number of counts in bin i;

$\langle N \rangle = (\sum_{i=1}^{n} N_i)/n$ is the expected value for a uniform distribution of events in n bins (i.e. the mean number of counts per bin);

σ_i^2 = the variance for bin i.

In the absence of pulsations, the fluctuations in the counts per bin are Poisson distributed, with the variance σ_i^2 best estimated by the mean number of counts per bin $\langle N \rangle$. Hence the χ^2 becomes:

$$\chi^2 = \sum_{i=1}^{n} \frac{(N_i - \langle N \rangle)}{\langle N \rangle}$$

From what precedes it follows that a flat light curve is expected from a random data set with the expectation value of χ^2 being $\sim \nu$, where ν is the number of degrees of freedom. For the present case $\nu = (n-1)$, the number of bins in the light curve minus one, as a one parameter fit is used. Thus at periods far from the correct period the light curve is expected to be flat, and $\chi^2 \simeq \nu$. However, at the correct period, the light curve is not expected to be well approximated by a flat distribution, the value of χ^2 will increase, and it is therefore the largest value of χ^2 that is sought in this type of analysis. When a large value of χ^2 is found, its significance may be assessed by computing

the probability associated with the given values of χ^2 and ν. Detailed discussions of the χ^2 test as applied in the search for the temporal structure of a celestial source may be found in Boldt et al. (1971) and Buccheri et al. (1977).

4.4 Low-energy Gamma-ray Measurements On The Crab Pulsar PSRØ531+21

4.4.1 Interpolation Of The Period -

The long integration time necessary at gamma-ray energies requires a high degree of accuracy in the pulsar parameters (period P and derivative $\dot{P}$) used to fold the gamma-ray arrival times to obtain the phase histogram. In general the radio measurements refer to an epoch not contemporary to the gamma-ray observation. This requires an extrapolation or interpolation of the parameters over time intervals which can be rather large; the resulting indetermination for P and $\dot{P}$ at the epoch of the gamma-ray observation is often such as to make a straight forward folding of the gamma-ray data meaningless. Another difficulty arising from interpolation is the occurrence of a glitch in the pulsar period in an epoch between the two observations; large glitches could be identified if there were observations made relatively closed to the occurrence, but micro-glitches could occur at any time. These are probably due to the magnetic field lines of the magnetosphere being torn apart as a result of the rotation of the neutron star. Also the proper motion of the source

or incorrect evaluation of its position may introduce problems.

No contemporary radio data for P and $\dot{P}$ were available; so in order to determine approximately what the pulsar period would have been at the epoch of our observation, an interpolation was made from radio data. There are two methods of interpolation, one uses the simple linear regression line technique and the other is to calculate the period using the period and period derivative of an observation before and after the required epoch. The latter method will give an error estimate and indicate any occurrence of glitches.

The straight-forward interpolation using the simple linear regression technique to the mid-interval of our observation period produced an expected value for the period of 33.258438ms and for the period derivative 4.2165×10^{-13} ss^{-1}. Figure 4.12 shows the graph for the period interpolation. The calculated method gave two expected periods of 33.258434 and 33.258437 ms for the mid-interval of our observation. The two methods combined to provide an expected value of 33.258436ms ($\pm$3 ns) for the period. The formal errors associated with the values P and $\dot{P}$ from radio measurements usually are very small and lead to negligible errors for the interpolated values. The error quoted on the expected P is just the would be change in P over the observation interval on the Crab ($\sim$ 4 hrs) as a consequence of $\dot{P}$, i.e. $\delta P = T_{Obs} \times \dot{P}$.

TABLE 4.4 Periods and Period Derivatives of the Crab Pulsar (PSR0531+21).

Epoch (JD-2440000)	P(sec)	$\dot{P}$(sec/sec) $\times 10^{-13}$	References
2647.0 (22 Aug 1975)	0.0331813125	4.22216	Bennett et al. 1977 (private communication to J.M. Rankin)
2982.0625 (22 Jul 1976)	0.0331935345	4.22108	Gullahorn et al. 1977
3946.442 (13 Mar 1979)	0.0332286993	4.21922	Wills et al. 1982
4128.5 (12 Sep 1979)	0.0332353356	4.21904	As last entry
4508.5 (26 Sep 1980)	0.0332491851	4.21782	As last entry
4762.3 (6 Jun 1981)	0.0332584350	4.21650	Our values
4910.5 (2 Nov 1981)	0.0332638331	4.21481	Gibson et al. 1982 (private communication to A.G. Lyne)

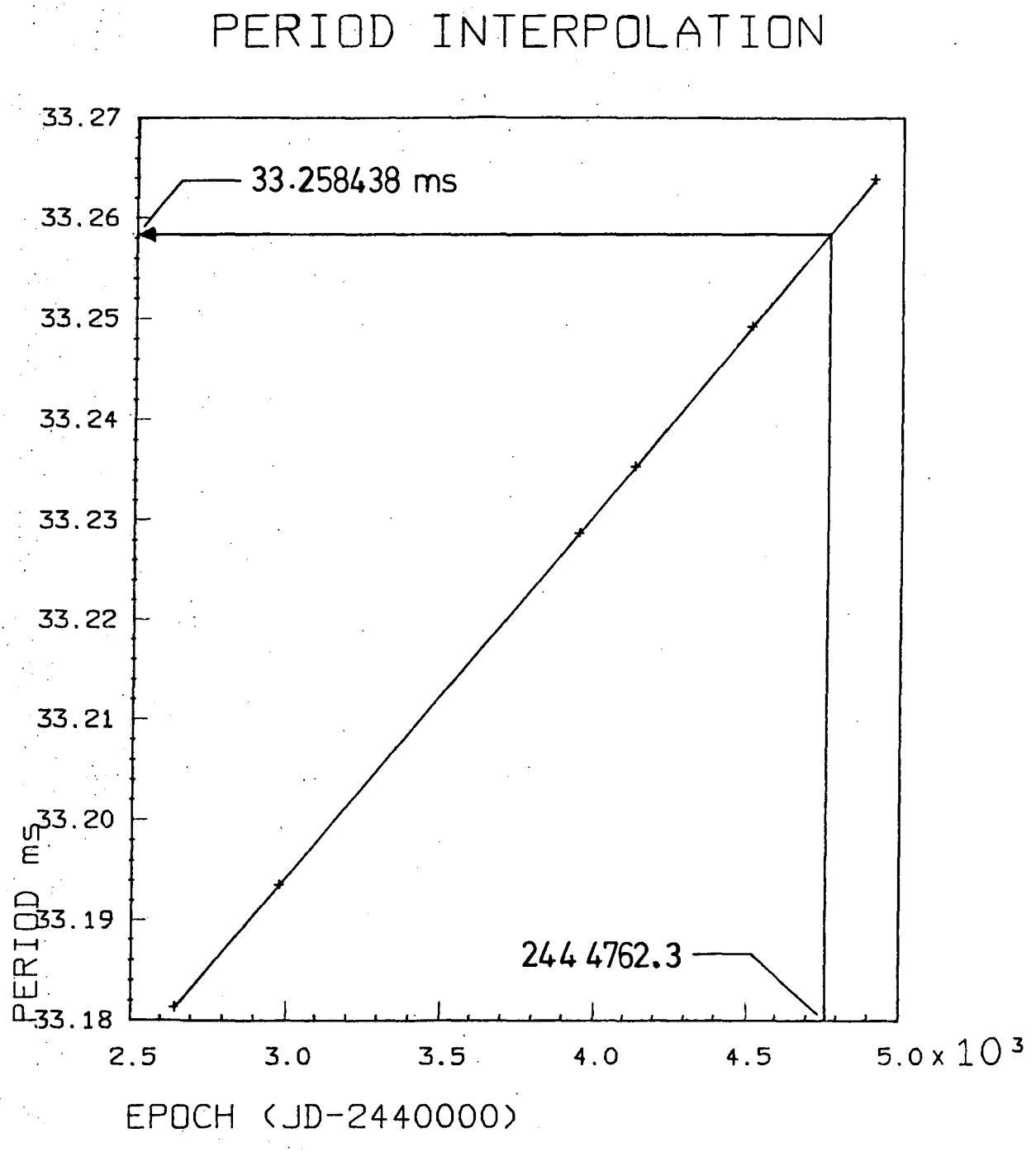

Figure 4.12 The interpolation of the Crab pulsar period.

4.4.2 Search For The Period At The Observational Epoch -

Before the search for the best period the background lines listed in Table 4.1 were subtracted. Although the nature of the pulsar obviates the need for separate background measurements in order to preclude any unnecessary background noise, those events which came outside a geometrical acceptance angle of 3.8° (3/4 of the FWHM value) were excluded. The distribution of the total detected events with respect to this acceptance angle of 3.8° is shown in Figure 4.13.

The events in the energy range from 50 keV to 2.5 MeV were considered. The barycentric photon arrival times were binned into 25 bins using the binning method discussed above. The reduced χ^2 (i.e. χ^2 divided by the number of degrees of freedom with an expected mean value of 1) for the resulting light curve was calculated. After each binning and test a new period was used. The data were searched for a range of trial periods on either sides of the expected period and the period derivative was held fixed at the value obtained from interpolation. The width of the scanning range was $2\Delta P = 2P^2/T_{Obs} \sim 150$ns covering an interval between 33.258360 and 33.258510 ms. The range was chosen to avoid missing the pulsation by a whole period on either sides of the expected period. The search was conducted in 1 ns steps within this range using χ^2 as the pulse profile indicator.

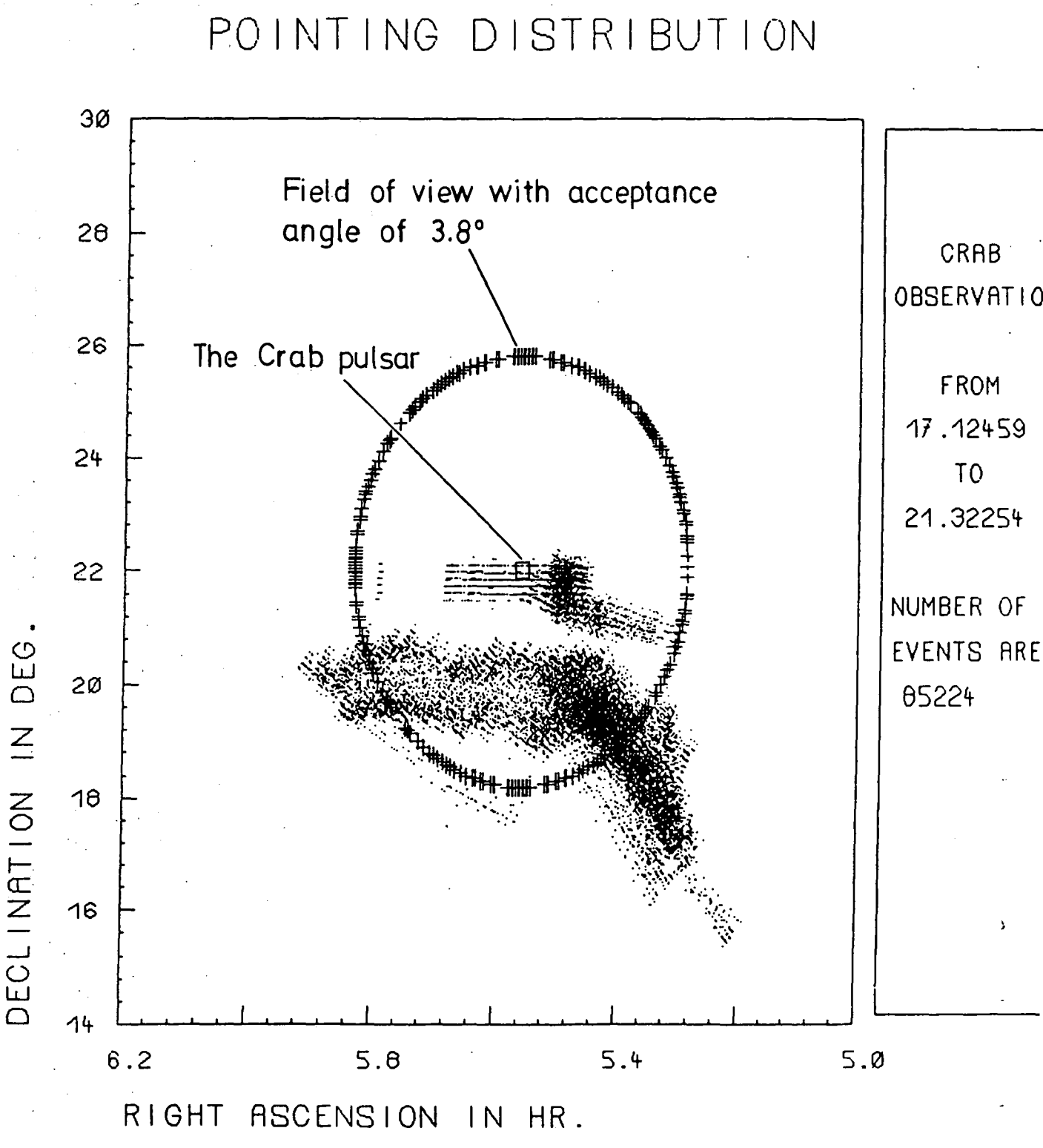

Figure 4.13 Distribution of events in right ascension and declination with respect to the acceptance angle of 38°.

The results of this analysis are shown in Figure 4.14, in which the reduced χ^2 is plotted against the period. The period associated with the highest reduced χ^2 was 33.258435ms, and the value of the reduced χ^2 was 2.07611 for 24 d.o.f. (degrees of freedom). This is compared with the reduced χ^2 vs period curve (Figure 4.15) for the case in which the photon arrival times are not corrected to the barycentre. Both the period and period derivative obtained from the analysis are tabulated together with the values of period and period derivative used for the interpolation in Table 4.4.

The sensitivity of the χ^2 to the change in origin was tested by scanning an arbitrary set of origins centred on the original chosen value across a whole bin. The χ^2 test as used for the period search was again employed. The results of the search for the best origin are shown in Figure 4.16. Since the highest χ^2 was sought in this analysis the origin which maximised the χ^2 was hence being used.

The probability for a region of enhancement occurring on the χ^2 vs period graph as a result of statistical fluctuation for a distribution of events with zero pulsed fraction may be estimated by assuming a binomial distribution of the events. If m is the total number of the scanning steps covering an interval for which the shift of an event in the light curve is at least of one period during the time length of the observation and k is the number of

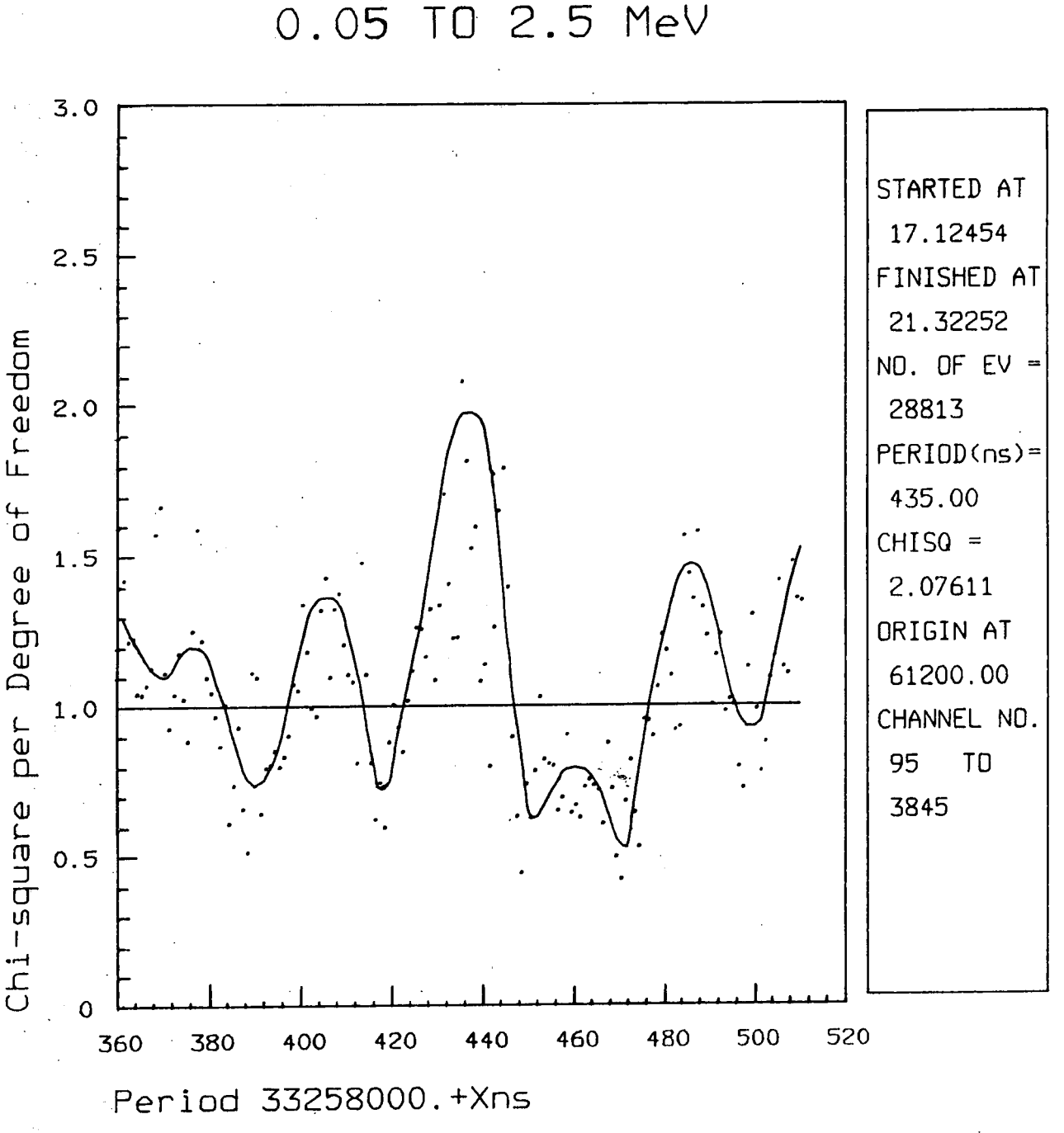

Figure 4.14 Reduced χ^2 vs period graph for search for the period at the epoch of observation.

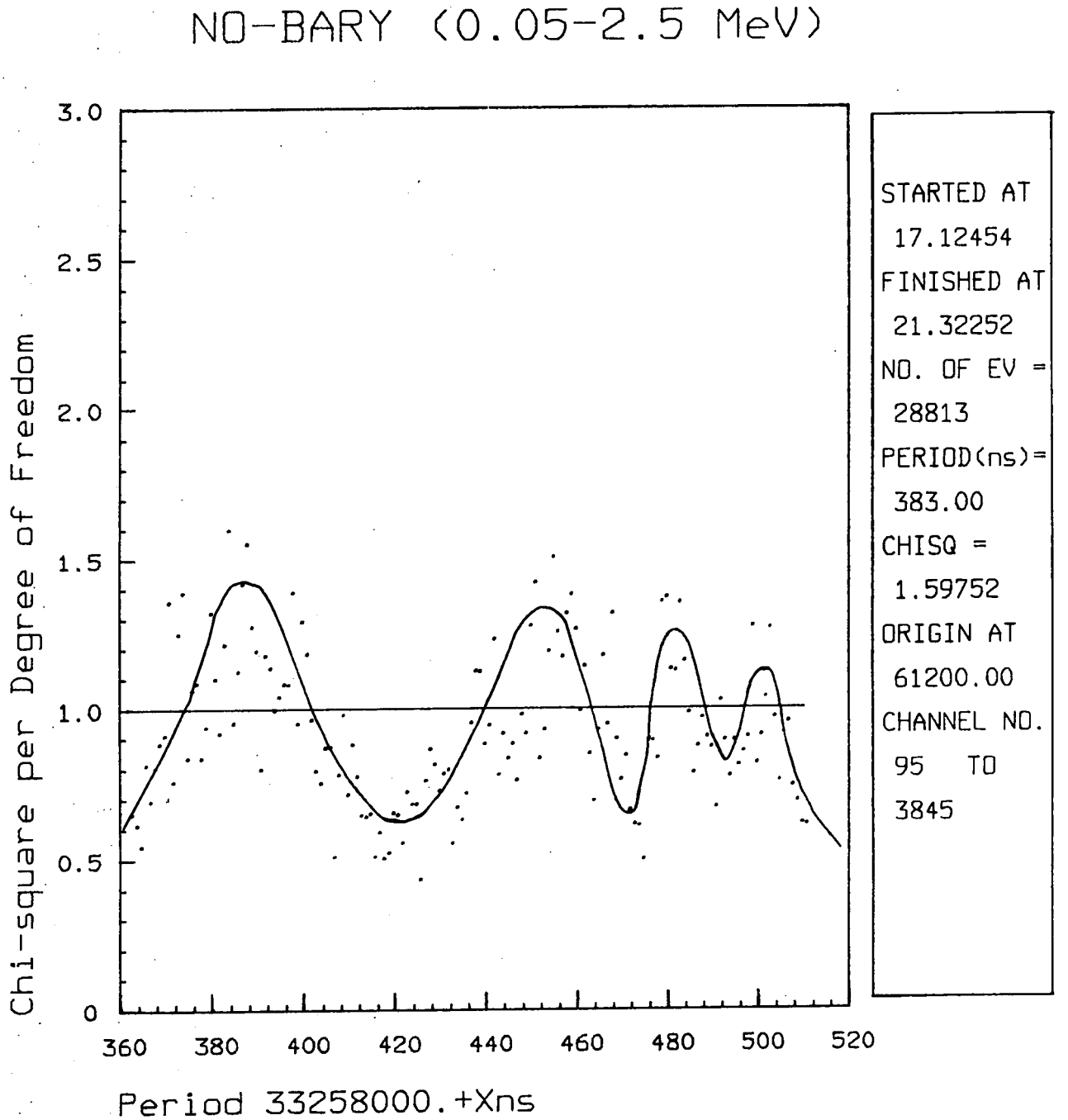

Figure 4.15 Reduced χ^2 vs period graph for a similar search as Figure 4.14 but photon arrival times are not corrected to the barycentre.

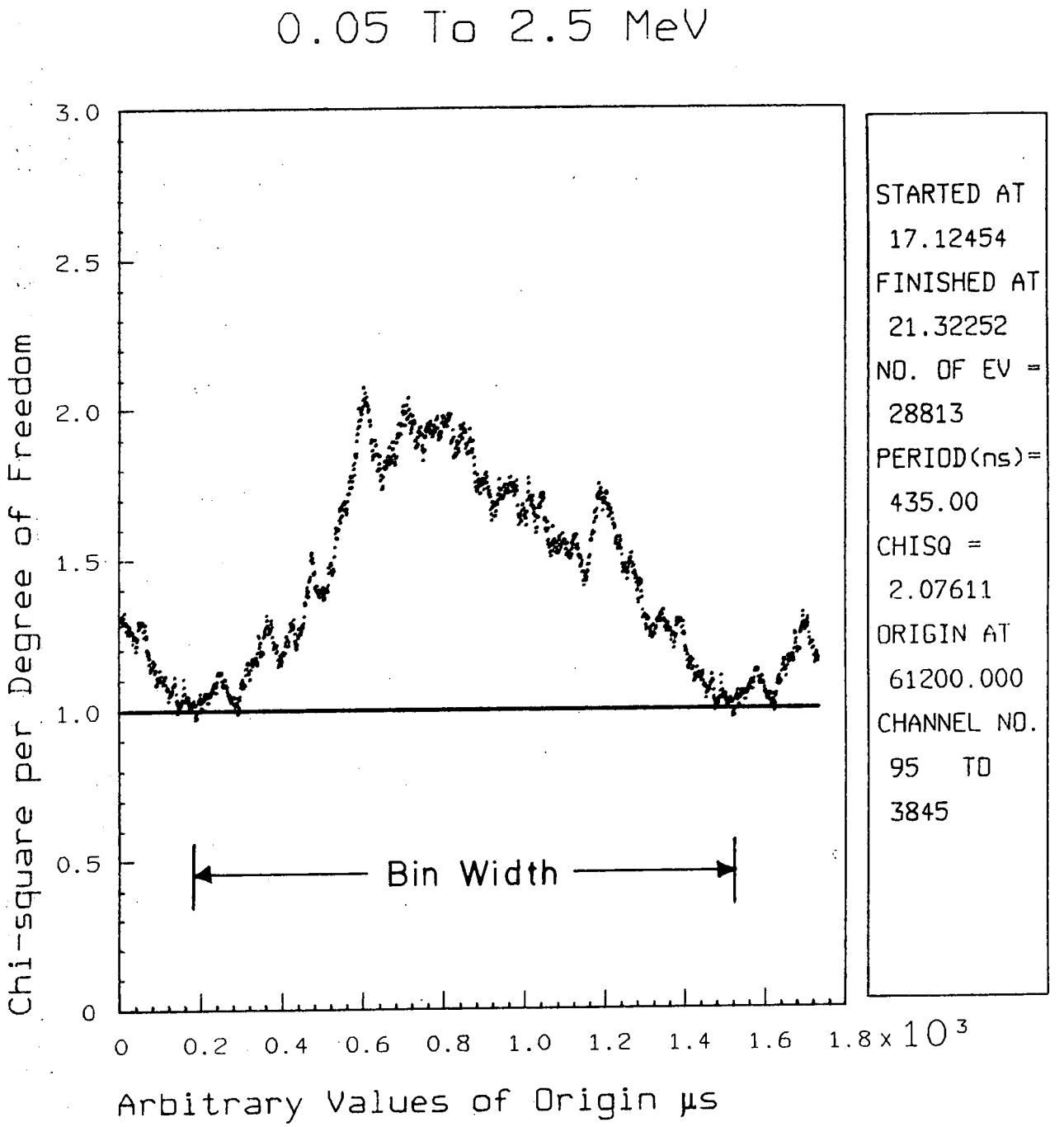

Figure 4.16 Reduced x^2 vs origin in the search for the best origin, bin width is given by the period divided by 25 (total number of bins).

times a value of χ^2 greater than a threshold χ^2_o is found, then the probability of occurrence of an enhancement region is given by:

$$Pr = \binom{m}{k} P^k \ (1-P)^{m-k}$$

where $P = P\ (\chi^2 > \chi^2_o)$ is the probability for $\chi^2 > \chi^2_o$ in a single trial.

The threshold χ^2_o defined corresponds to a 'detection' at a certain confidence level which has a small probability of being exceeded by chance, the confindence level chosen in this case is the 95% confidence level. In statistical 'jargon', an event being detected at the 95% confidence level is termed as 'very likely to be true'. The probability that Figure 4.14 is the result of a chance fluctuation calculated using the above equation is

$$Pr \sim 0.029$$

(reference χ^2_o threshold = 1.64017 at the 95% confidence level)

4.4.3 The Resulting Light Curves -

The resulting light curve with the best period and best origin from a superposed epoch scan of all gamma-ray counts with channel numbers in the range 95 to 3845 (corresponding to energy 50 keV to 2.5 MeV) is shown in Figure 4.17. The mean background line shown is the mean value of the non-pulsed bins. The probability associated with a value of χ^2 can be found in p122-129 of the Biometrika Tables for

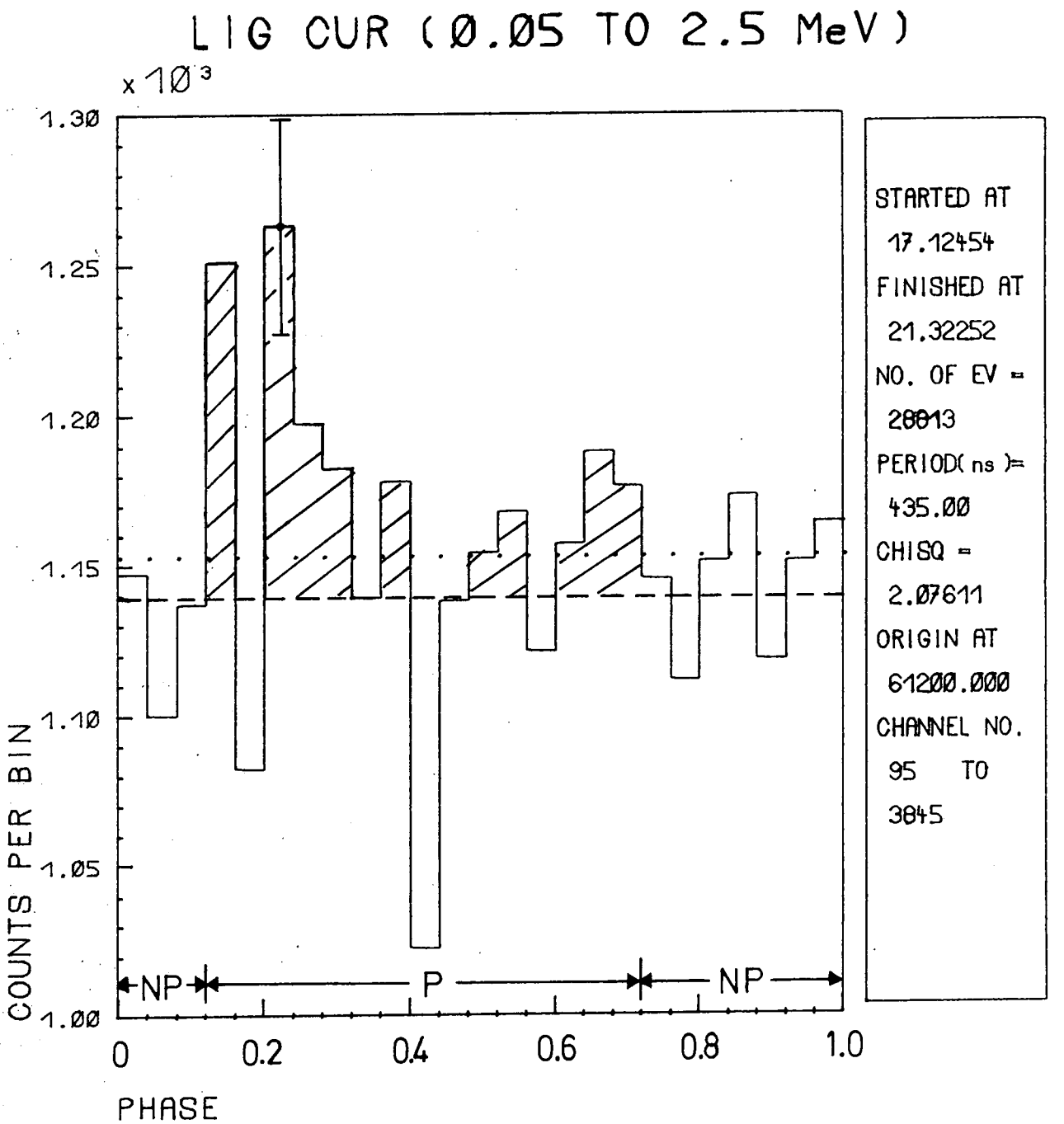

Key:- P Pulsed
NP Non-pulsed
. . . . . mean number of counts per bin
---- mean background
//// excess pulsed counts above background

Figure 4.17 Light curve in the energy range 50 keV to 2.5 MeV, error bar is $\pm\sigma$.

Statisticians Vol 1., edited by E.S. Pearson and H.O. Hartley. The probability of obtaining a reduced χ^2 of 2.07611 for 24 d.o.f. is 0.00152.

The light curves for the energy range 0.050 to 5.0 MeV (Figure 4.18), 0.050 to 7.5 MeV (Figure 4.19), and 0.050 to 10.0 MeV (Figure 4.20) are shown for comparison; these are obtained using the best period and origin resulting from the analysis for the energy interval between 0.050 and 2.5 MeV. The respective reduced χ^2 and its probabilities associated with each of these light curves are tabulated together in Table 4.5. The contribution from the background reduces the significance of these light curves at higher energies as can be seen from the χ^2 values. The following summarises the reasons why the temporal analysis for search for pulsed emission was concentrated in the energy region from 0.050 to 2.5 MeV:

(1) The three line features observed were in the first quarter of the operational energy range of the detector (0.050 to 10.0 MeV).

(2) Insufficient statistics and domination by noise above 3 MeV made the analysis very difficult.

4.4.4 The Spectrum Of The Crab Pulsar -

For the spectral analysis, three separate light curves were generated by dividing the data according to the following energy intervals: 150-400 keV, 400-1000 keV, 1000-3000 keV. The phase of the light curve was divided

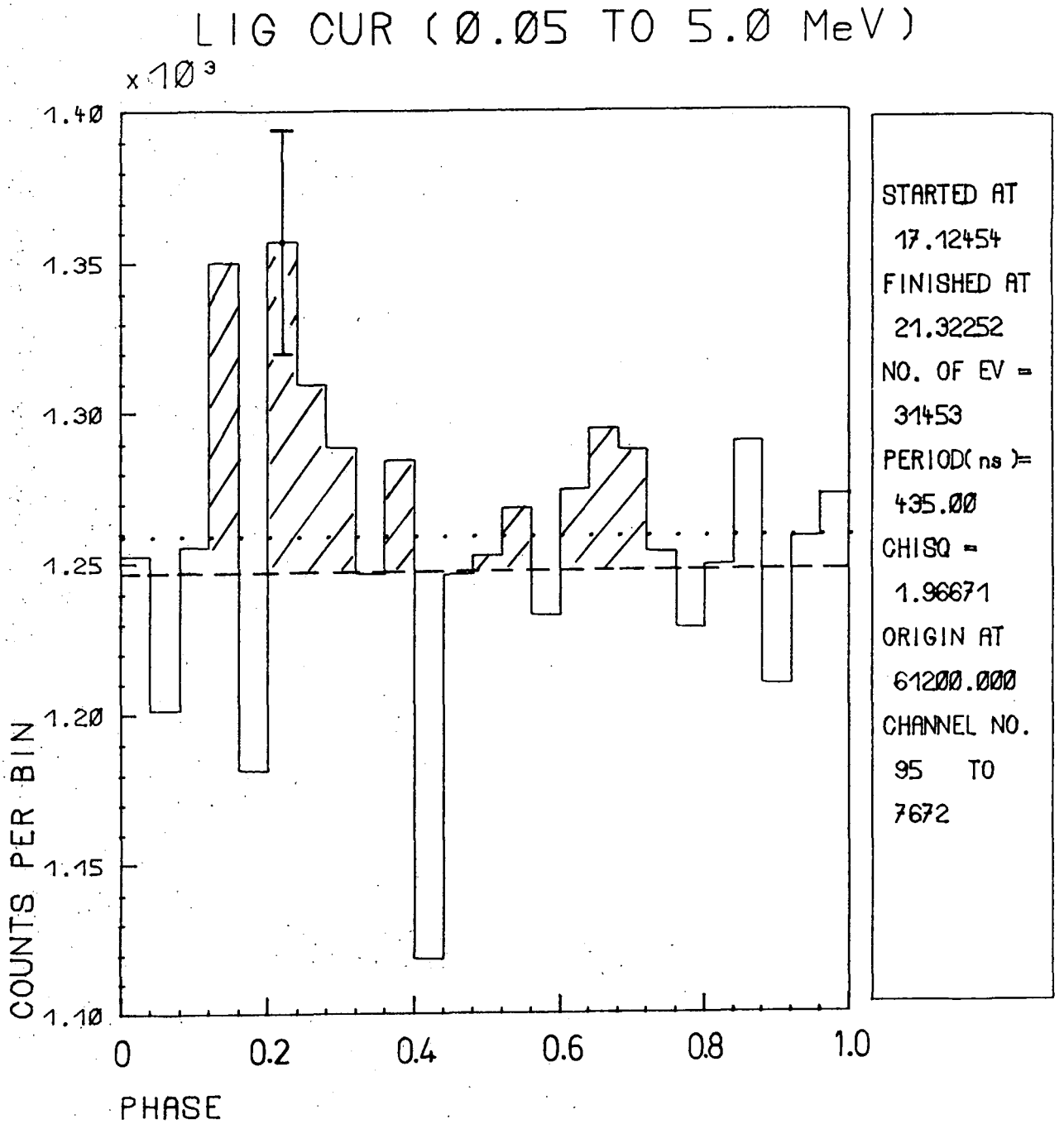

Key:- /// excess pulsed counts above background
..... mean number of counts per bin
---- mean background

Figure 4.18 Light curve in the energy range 50 keV to 5.0 MeV, error bar shown is $\pm\sigma$.

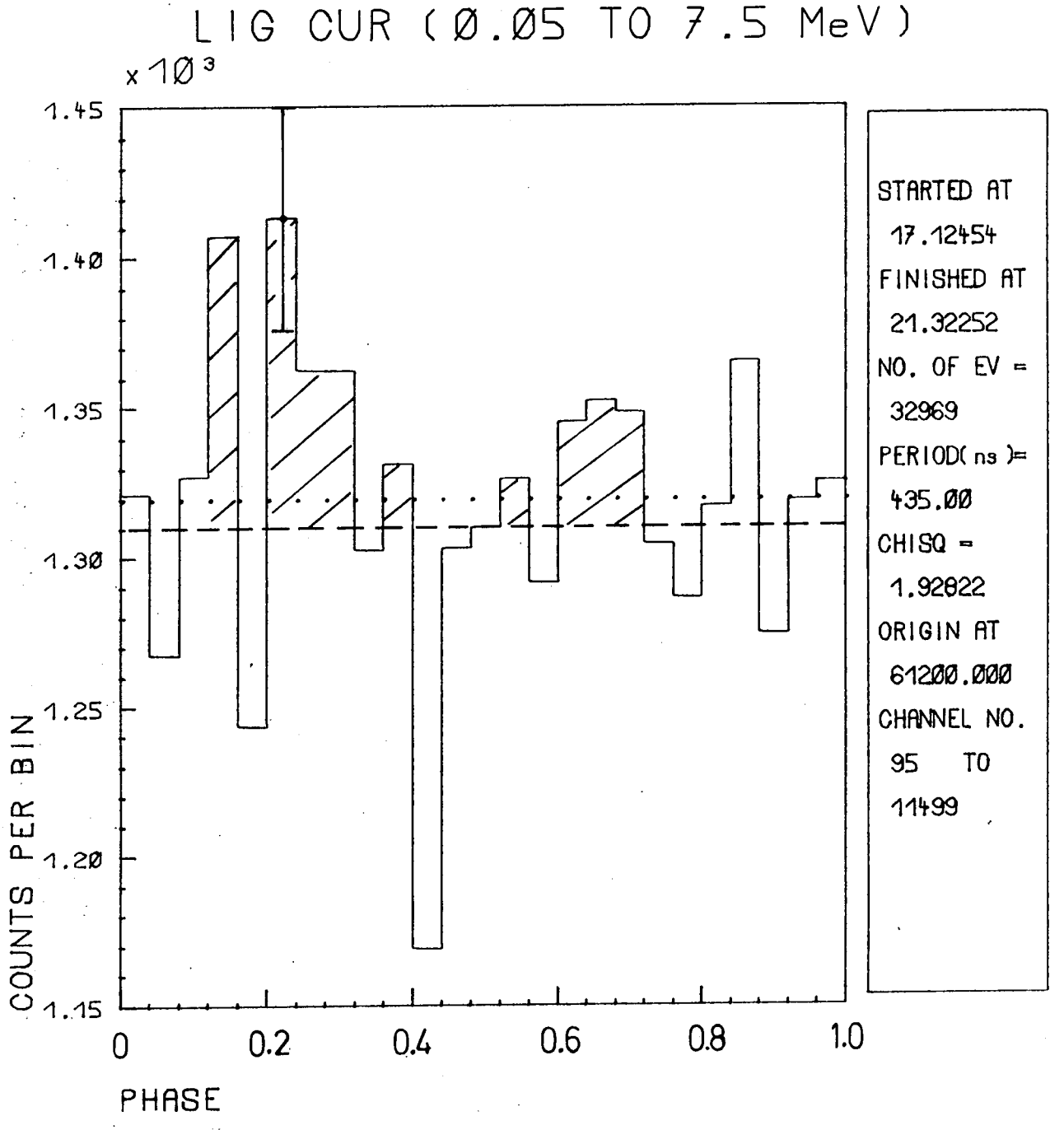

Key:- //// excess pulsed counts above background

. . . . . mean number of counts per bin

– – – – mean background

Figure 4.19 Light curve in the energy range 50 keV to 7.5 MeV, error bar shown is $\pm\sigma$.

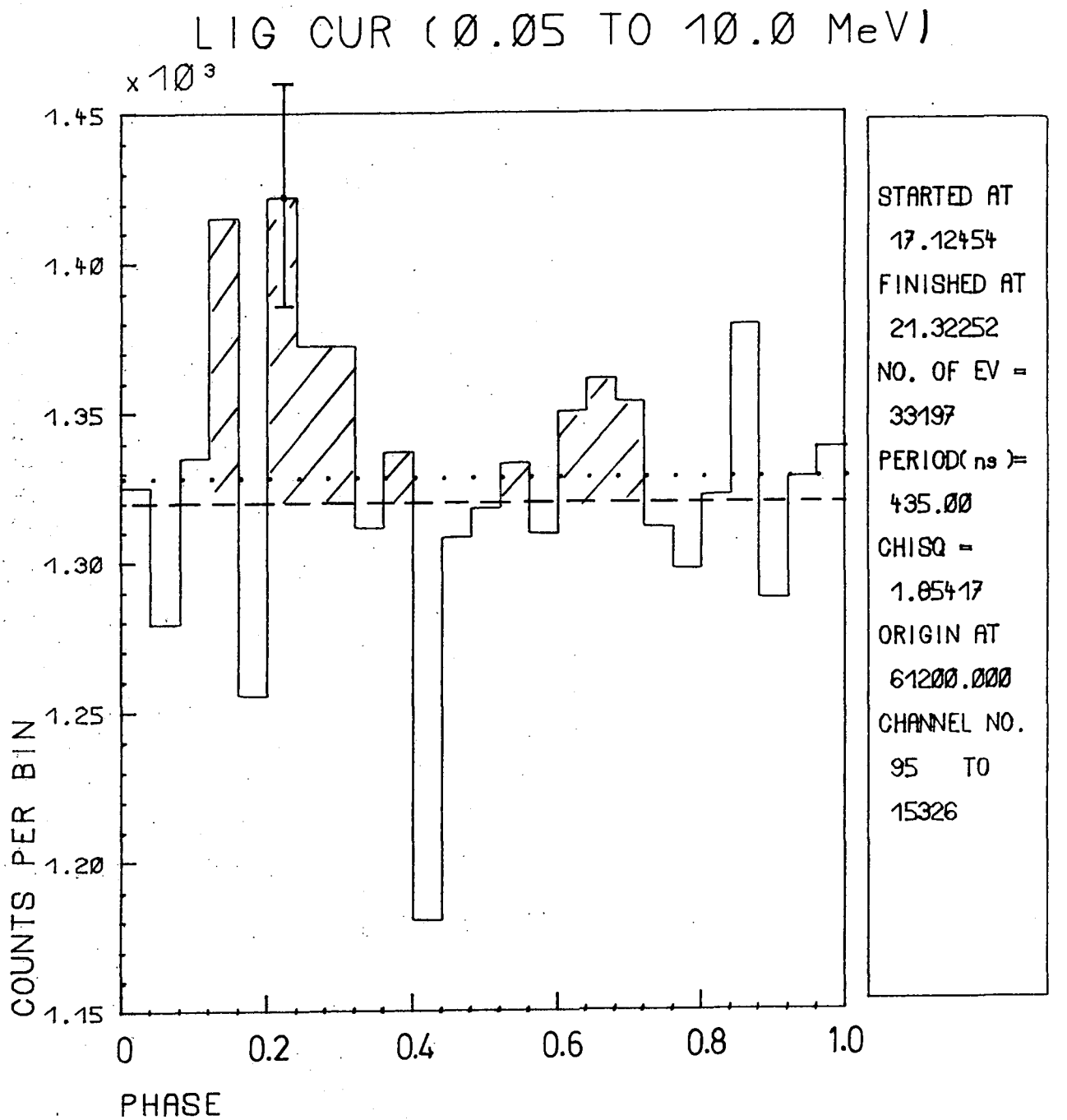

Key:- //// excess pulsed counts above background
. . . . . mean number of counts per bin
– – – – mean background

Figure 4.20 Light curve in the energy range 50 keV to 10.0 MeV, error bar shown is $\pm\sigma$.

TABLE 4.5 Values of Probability for the reduced χ^2

Energy MeV	Reduced χ^2 (24 d.o.f.)	Probability
0.05-2.5	2.07611	0.00152
0.05-5.0	1.96671	0.00328
0.05-7.5	1.92822	0.00417
0.05-10.0	1.85417	0.00683
78.9 keV	0.88169	0.62918
404.4 keV	1.27033	0.16964
1049.6 keV	0.78670	0.76816

into the pulsed and non-pulsed regions as indicated in Figure 4.17. The non-pulsed region was used as background in the subsequent step. The counting rate due to the pulsar was determined for each light curve, by subtracting the non-pulsed counts from the pulsed counts and corrections were applied for atmospheric attenuation, photopeak detector efficiency and system dead time to convert the rate to the equivalent fluxes at the top of the atmosphere. The resulting spectrum of the Crab pulsar is shown together with results of other experiments in Figure 4.21. The present result is in agreement with a power law $\sim E^{-2.2}$.

4.4.5 Search For Pulsed Line Emission -

A similar search was carried out on the three line features. The individual light curves for these three line features were obtained first. Then the non-pulsed counts were subtracted from the pulsed counts and the excess counts determined. In each case, no excess counts were obtained after subtraction. The whole data set was also divided into three subsets with the same time intervals as those used for the line feature search, again yielded null results. The light curves obtained for the 3 line features are shown in Figure 4.22, 4.23 and 4.24. The associated reduced χ^2 and probabilities are listed in Table 4.5. The 78.9 keV line feature is for the final period of the observation in accordance with the line feature search in section 4.2 above.

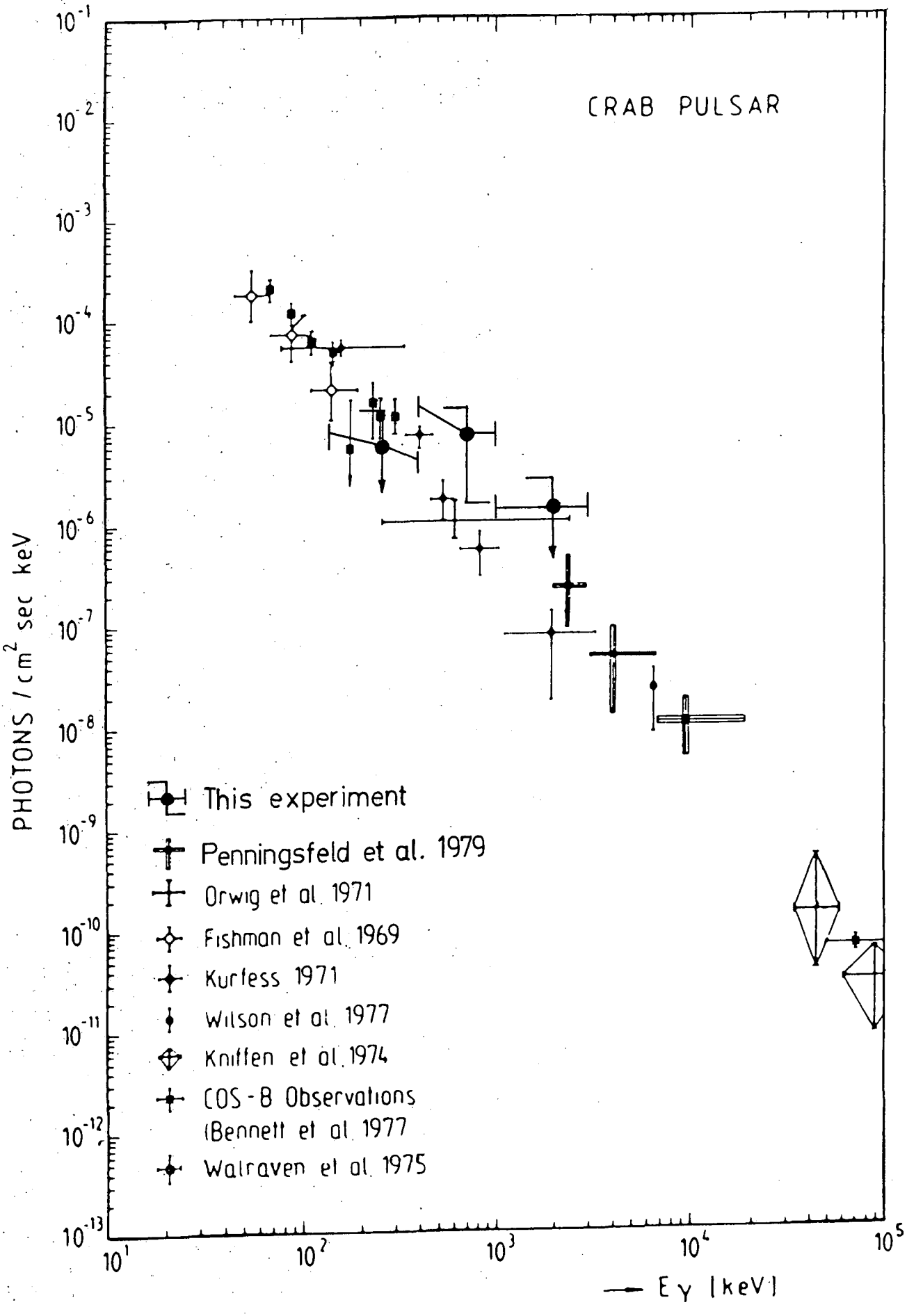

Figure 4.21 Energy spectrum of the pulsed emission from the Crab pulsar.

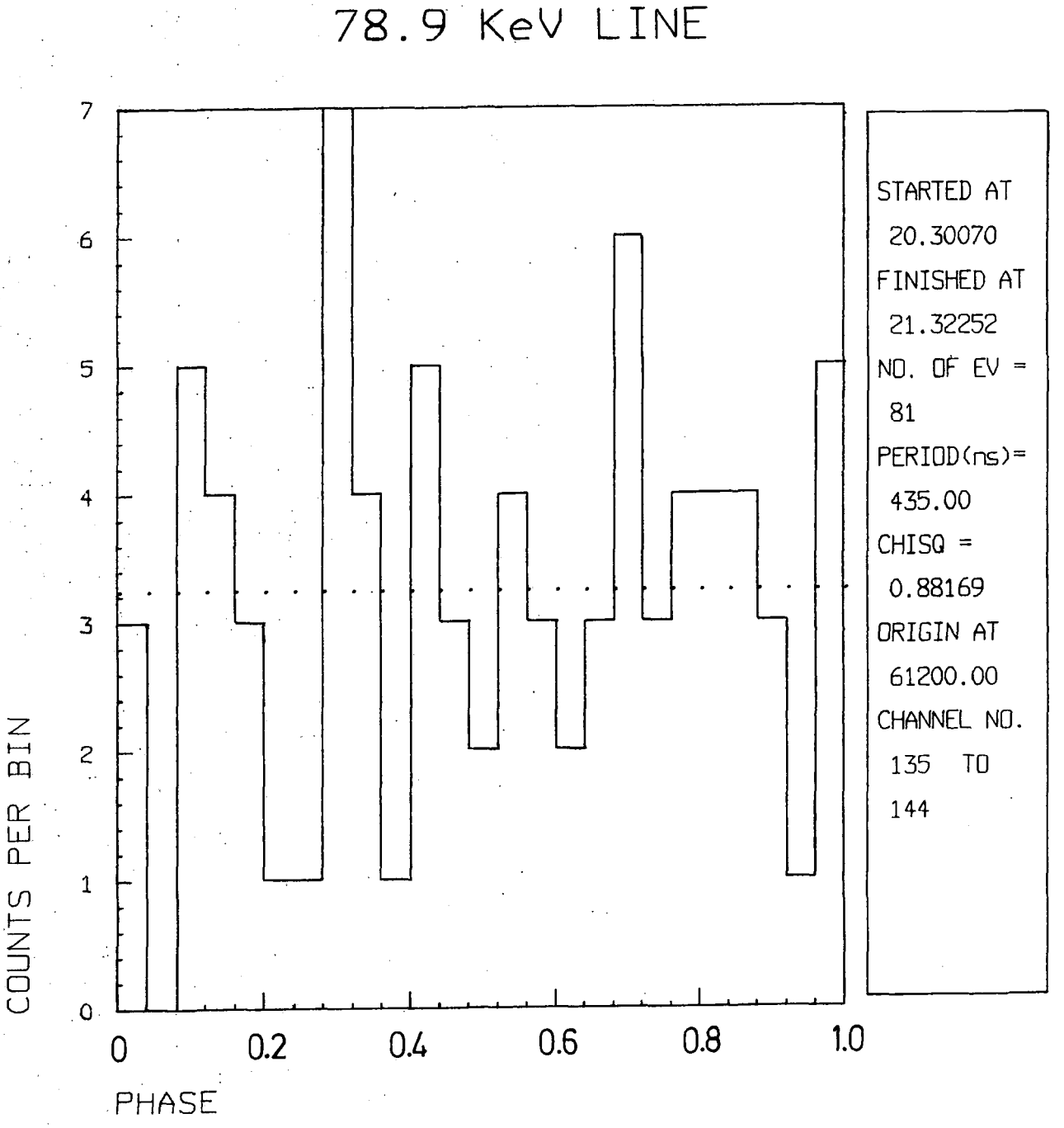

Figure 4.22 Light curve for the 78.9 keV line feature, ... is the mean number of counts per bin.

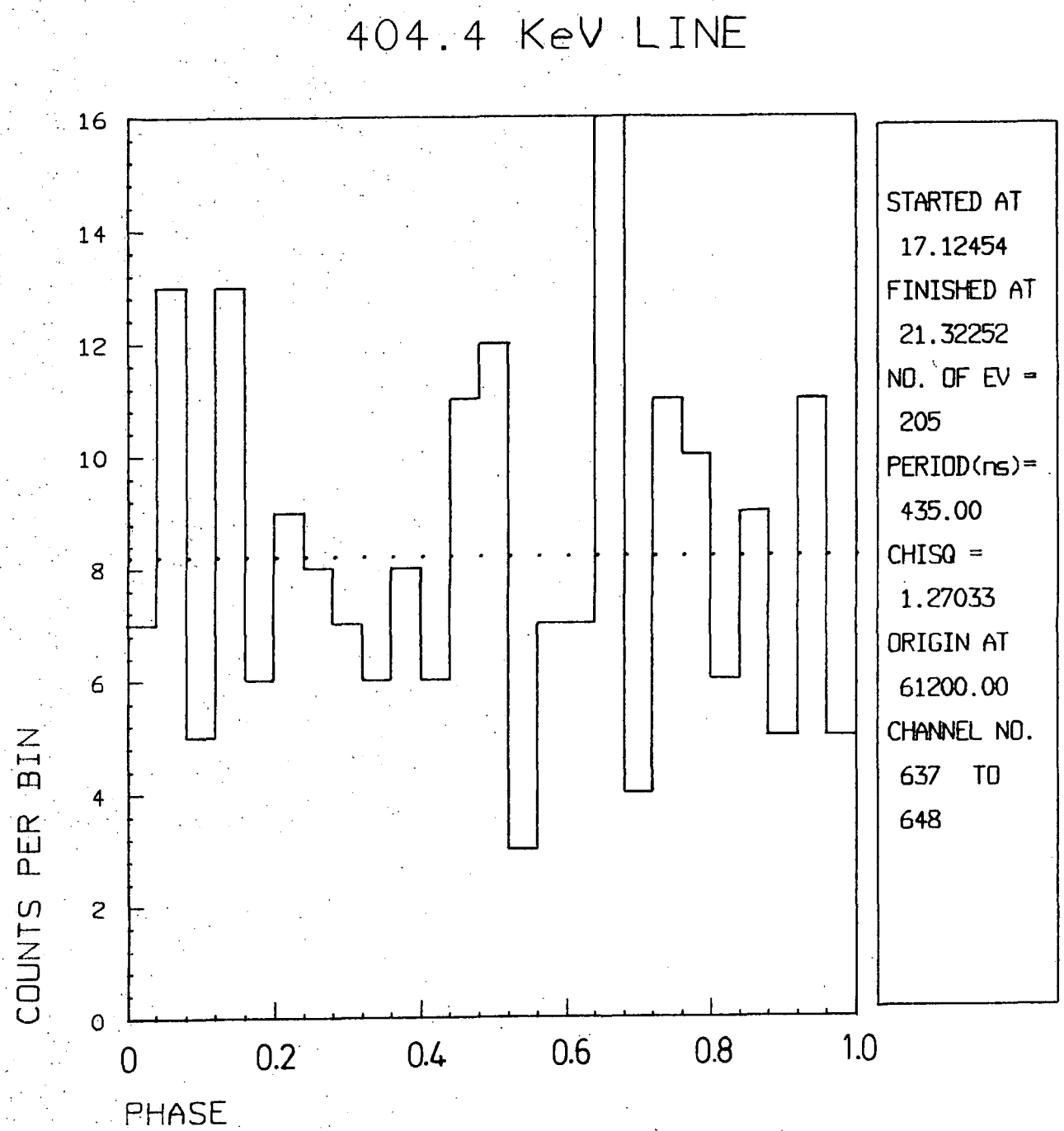

Figure 4.23 Light curve for the 404.4 keV line feature, ... is the mean number of counts per bin.

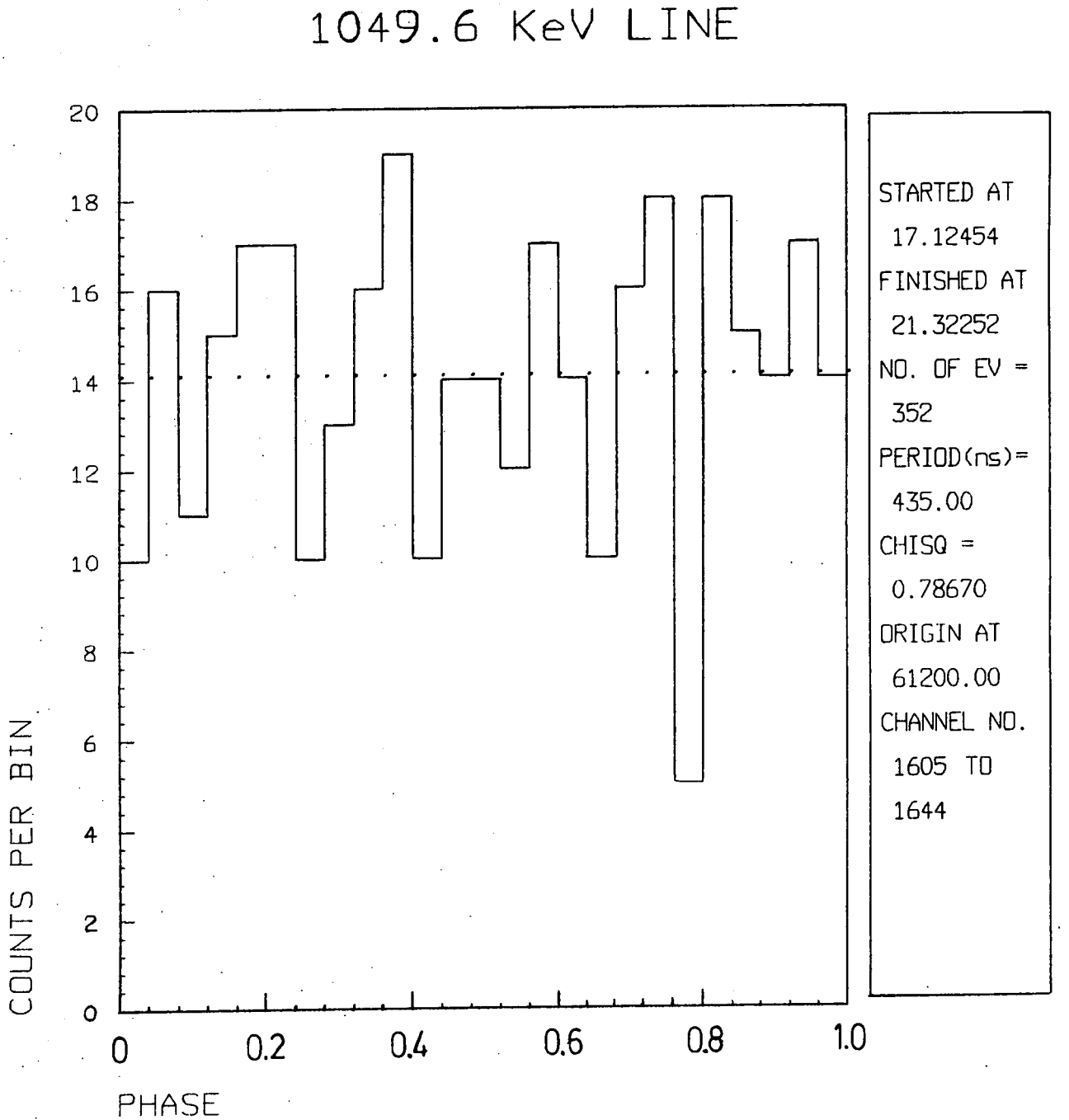

Figure 4.24 Light curve for the 1049.6 keV line feature, ... is the mean number of counts per bin.

The entire analysis on the data obtained from the Crab has been presented. The results of the analysis are, in general, in good agreement with previous measurements. The implications of these results and new findings are discussed in the next and last chapter.

CHAPTER 5

DISCUSSIONS

5.1 Possible Gamma-ray Line Features From The Crab Nebula Region

5.1.1 Line Features Observed -

Of the three gamma-ray line features seen in this experiment, the 78.9 keV line is observed as a transient effect. As mentioned in the foregoing chapters, similar line features in this energy region have already been observed by various experimenters. A feature at 73 keV was first observed by Ling et al. (1979) from the Crab Nebula region and subsequently confirmed by Manchanda et al. (1982). A similar feature at 77 keV which persisted only for about 25 minutes was shown by Strickman et al. (1982) to pulse with the Crab pulsar period. The most likely source of this line is cyclotron emission at the gyrofrequency of the intense (8×10^{12} G) magnetic field at the polar cap of the neutron star. Unfortunately, the line is not seen to pulse with the frequency of the pulsar in this experiment. The reason for the lack of identification is possibly the large atmospheric and detector background in this energy region.

The results for the line at 404.4 keV confirm earlier results of other experiments. The physical origin for the feature is uncertain, there have been several mechanisms proposed for generating positrons at or above the surface of the Crab neutron star e.g. the Polar Cap model of Sturrock (1971) mentioned earlier. Positron annihilation in dense gases and solids usually results in the emission of 511 keV photons. Should this occur near the stellar surface the photons would appear at the Earth to be gravitationally red-shifted. The present measurement then determines z = 0.26 (assuming no other sources of frequency shift). For this hypothesis to be correct, ~ 10^{41} positrons s^{-1} must be annihilating into 511 keV photons near the neutron star surface (assuming isotropic radiation) which then reach Earth without significant Compton scattering. Leventhal et al. (1977) oberved the line at (400 $\pm$ 1) keV which gives a gravitational red shift value of z = 0.28. The difference between the two results suggest there may be some variability in the value of the red shift over a period of 5 years. The discrepancy between the values of the energy obtained by Leventhal et al. and this experiment cannot be explained by any systematic effect, as monitoring of the background lines in both experiments enabled continuous checks on the energy calibrations of the detectors to be made.

The 1049.6 keV line feature has not been detected by other experiments in this energy range before. Although Baker et al. (1973) have suggested that the continuum flux in the few MeV regions is higher than that expected from an extrapolation of the low energy region from an analysis of their data from a balloon flight in September 1972. However, Schonfelder et al. (1975) or Carpenter et al. (1976) found excellent agreement for an extrapolation from the lower energy region. It is obvious that the existence of this line awaits confirmation of a separate experiment before its nature can be elucidated.

5.1.2 Validity Of The Search Technique -

The search technique involved calculating the significance of the lines based on the formula of Li and Ma. Their formula is an improved version of the formulae on relative likelihood methods derived earlier by Hearn (1969), O'Mongain (1973) and Cherry et al. (1980). A special feature in the formula of Li and Ma is that 'time on' and 'time off' measurements have been taken into account. A comparison of the resulting probabilities computed with Monte Carlo simulations are shown in the paper of Li and Ma. It seems their formula gives the best estimate of the probability.

Further justification of these lines can be obtained by showing the absence of negative line features. This is easily acquired, as the technique is symmetric with respect

to both positive and negative fluctuations. Only three negative line features in the total Crab spectrum were identified with significance more than 3.Ø σ, the greatest being 3.87 σ with a confidence level of Ø.85Ø for 2985 degrees of freedom.

5.2 Pulsed Emission From The Crab Pulsar

5.2.1 The χ^2 Vs Period Curve -

The χ^2 vs period graph (Figure 4.14) peaks at a period of 33.258435ms which is in excellent agreement with the interpolated period of 33.258436ms (±3 ns). The graph shows the characteristic behaviour as expected from a set of Monte Carlo simulations by Buccheri et al. (1977). It has a broad feature with a width w ~3Øns (the central maximum) and a few tangible side maxima. This gives a Q-factor of $\sim 1Ø^{10}$ ($2\pi/Pw$). This order of magnitude of the Q-factor eliminates the possibility that this effect is due to an artifact of the detector. The broad feature of the χ^2 curve would be more prominent if there were better statistics and a greater fraction of pulsed events. The χ^2 vs period graph would then be similar to that for optical diffraction, where the central maximum is positioned symmetrically around the expected period, with a half width corresponding to the number of scanning steps which produced in the light curve a shift of one period during the entire observation time. On either side of the main maximum, secondary maxima appear with decreasing amplitude. The maxima are structured,

depending on the shape of the light curve of the pulsar.

By lowering the fraction of pulsed events, the amplitude of the "χ^2 pattern" decreases and the "side maxima" tend progressively to disappear in the noise. With limited statistics and a low pulsed fraction (events), the central maximum becomes less and less prominent with an apparent reduction on its width, while the "side maxima" are no more detectable. This can be seen in Figure 5.1 when a search is conducted in the background (events outside the geometrical acceptance angle of 3.8°) where no pulsed events are expected to be present; indeed no appreciable maxima are seen. Figure 5.2 shows the accompanying light curve for the search on the Crab background. As expected no obvious structure is to be seen.

5.2.2 Implication Of The Light Curve -

The accurate timing capability of the Durham MK1B spectrometer has enabled the construction of gamma-ray light curves by folding the photon arrival times at the Solar System barycentre with the pulsation parameters obtained from interpolation of radio data. The measurement has produced a light curve for the energy range Ø.Ø5 to 2.5 MeV that has a pulsed duty cycle $\beta \sim 60 \pm 4\%$ (β is the fraction of the period with non-zero flux above background) showing two peaks separated by a phase of $Ø.44 \pm Ø.Ø4$. These are compared with the normally quoted values for the duty cycle of ~55% and the separation of the two peaks with a phase of ~Ø.4.

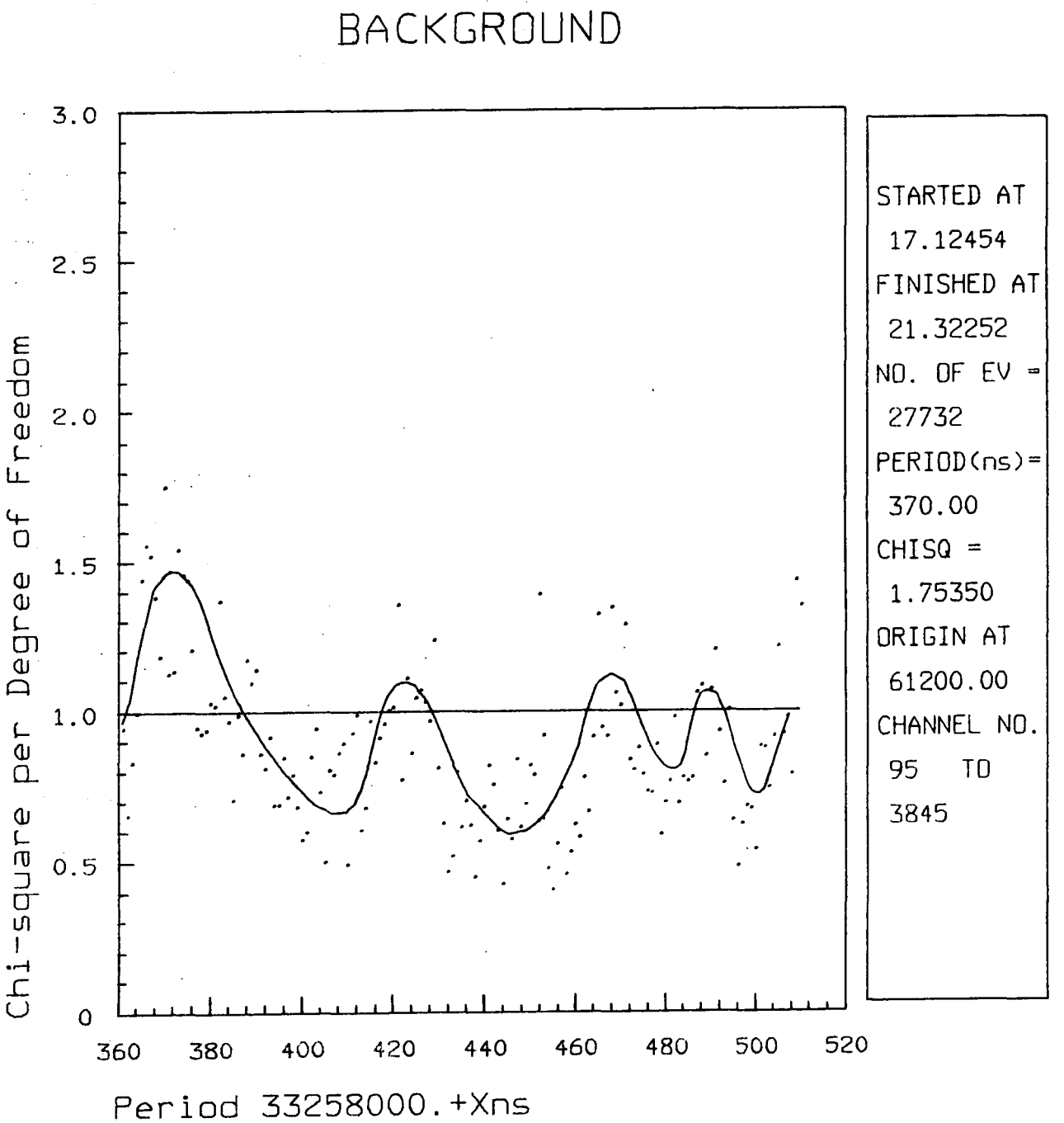

Figure 5.1 Reduced χ^2 vs period graph for the background.

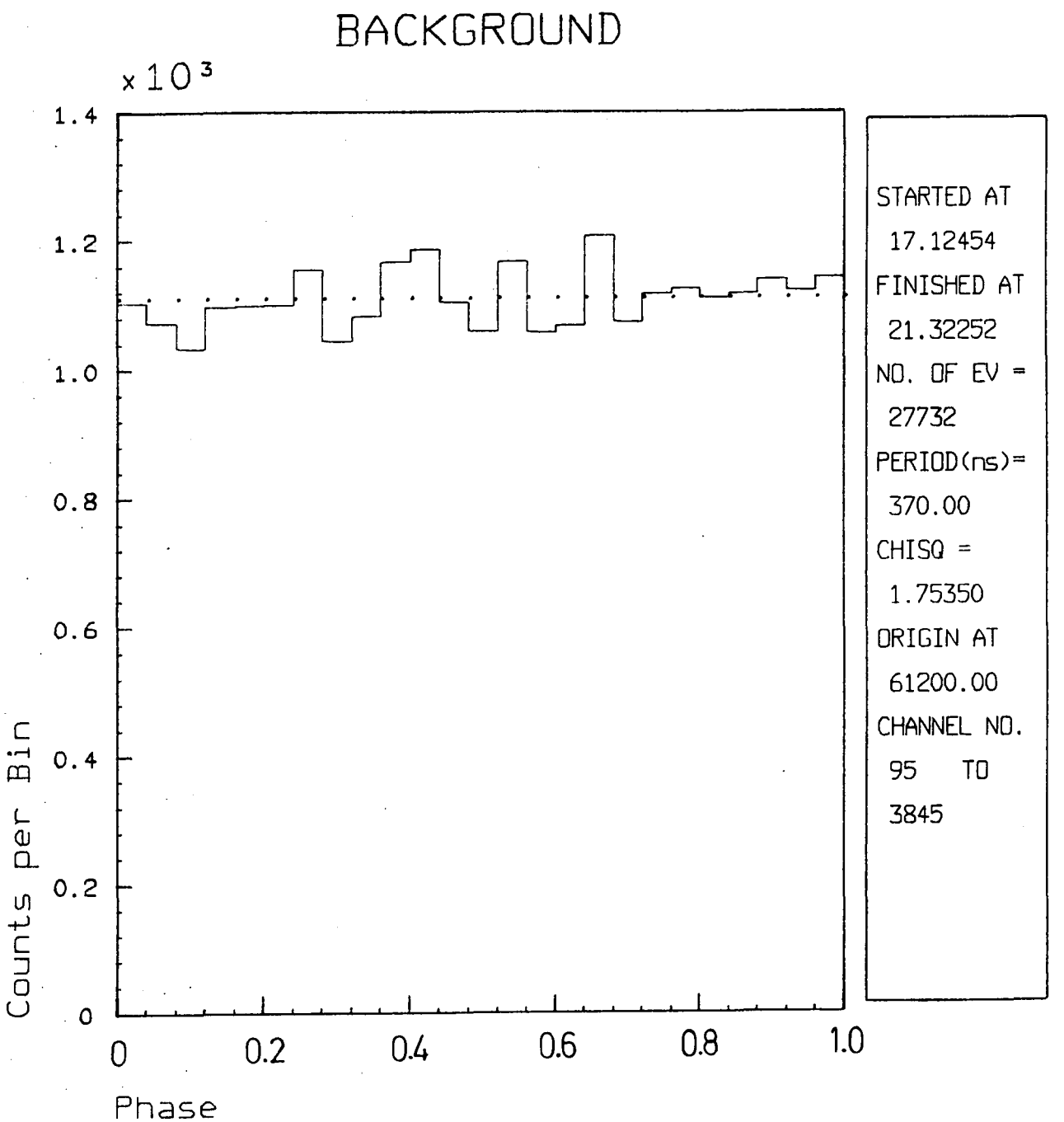

Figure 5.2 Light curve for the background, · · · · is the mean number of counts per bin.

The resulting light curves also give a clear indication of a variation with energy of the relative strength of the two peaks. No interpulse emission between the two main peaks can be seen in Figure 4.17.

There are two observed features of the light curve which are not compatible with other experiments in this energy range:

(1) The second peak is relatively weak.

(2) Two large dips are seen, one in the first peak and another in the interpulse region between the two peaks.

There are three possible explanations for these incompatibilities. Namely, they are (i) due to errors in the arrival time corrections; (ii) caused by detector hardware errors; (iii) caused by statistical fluctuations upon some structured background radiation.

Out of these three possibilities, (i) seems to be most unlikely, since any errors in the arrival time corrections will result in the wrong period for the Crab pulsar being obtained and consequently a flat light curve would be expected. There may be reasons to suspect that these are due to hardware errors. The most likely candidate for the cause is the Pulsar Clock. Negligible error arises because of a lack of clock stability as the internal crystal oscillator has a specification stability of better than 1 part in 10^8. Errors may arise in the recording and transmission of the data, but any errors (if there are any) are negligible as already been discussed in the section on

Pulsar Clock Calibration of Chapter 4. Hence, the only obvious cause is that due to statistical effects. This can be reduced somewhat by rebinning the light curve into smaller number of bins. The light curve in the energy range 50 keV to 2.5 MeV after rebinning is shown in Figure 5.3.

Although, the 'dips' have disappeared the 'weakness' of the second peak is more clearly seen. If this effect is real, then the cause may be attributed to the pulsar itself. The variation in the strength of the second peak has been seen in the X-ray region (Floyd et al. 1969, Kurfess 1971 and Ryckman et al. 1977) and at high-energy gamma-ray by COS B (Wills et al. 1982). In the low-energy gamma-ray region no reports have been found for the variation of the second peak of the light curve. If the result of this experiment is correct then this would be the first detection of a variation of the second peak. However, Graser and Schonfelder (1982) obtained asymmetric peaks in their light curve in the 1.1-20 MeV energy region and they ruled out time variability at MeV energies.

5.2.3 Sensitivity Of The Epoch Folding Technique -

The search for the Crab pulsar period for the epoch of the present observations was conducted using the epoch folding technique. The technique has been extensively used in both X-ray and gamma-ray astronomy. Although the fast Fourier transform method could be performed to examine the data for evidence of periodic pulsations. However, pulsar

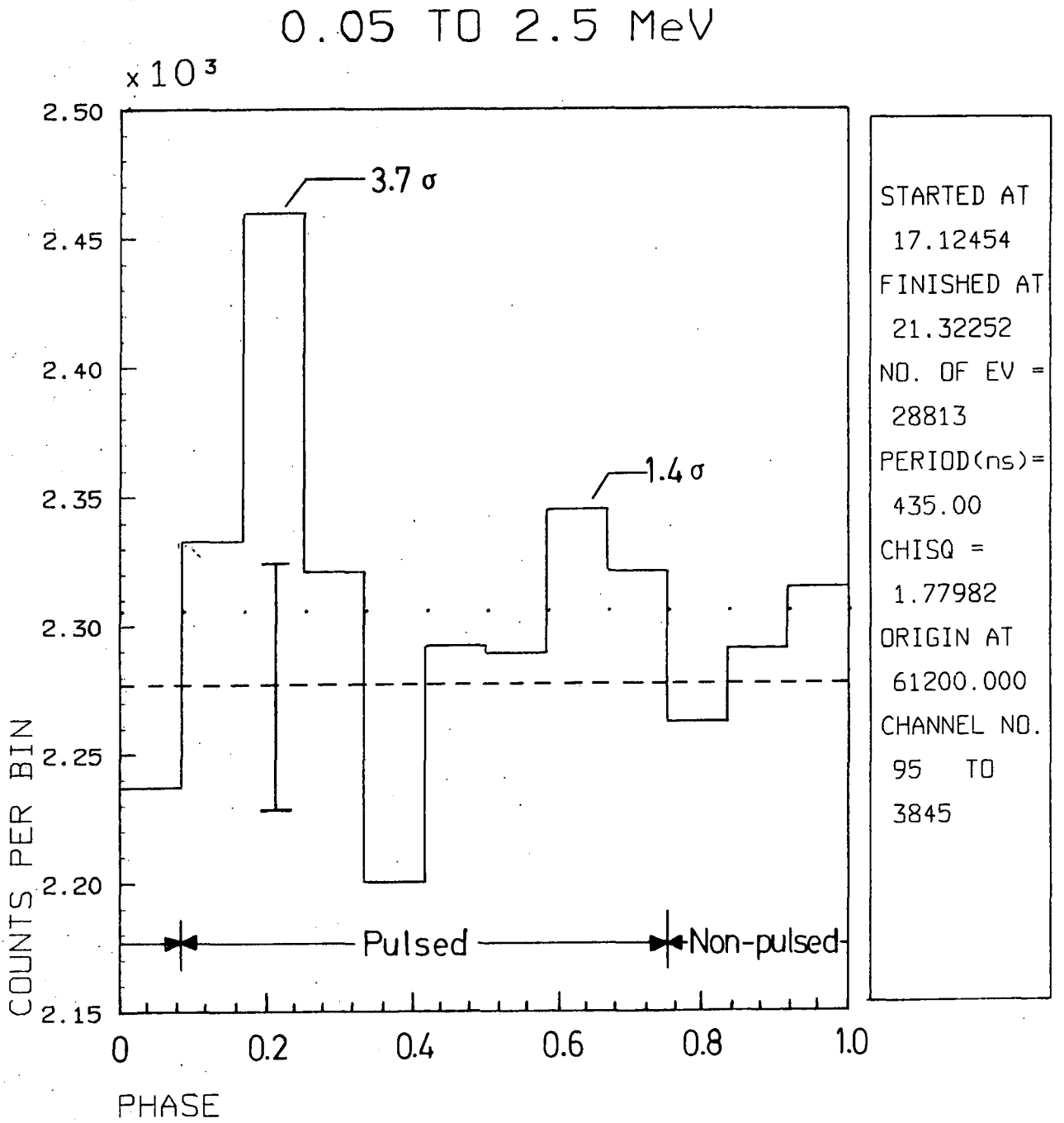

Key :-

. . . . mean number of counts per bin

– – – – mean background

Figure 5.3 Light curve in the energy range 50keV to 2.5 MeV with 12 bins.

frequency searches using Fourier analysis, which look at the power in the frequencies sampled, suffer from the fact that the signal-to-noise ratio increases as the fourth-root of the time rather than as the square-root. Also the pulsation period of radio pulsars is usually known to high precision (< 1 part in 10^9) and a search using the Fourier transforms is not needed. Further, the Fourier transform technique is difficult to interpret in the presence of gaps in the data. On the other hand, the epoch folding technique is relatively insensitive to randomly ocurring gaps in the data so long as the net pulse phase coverage is reasonably uniform. Moreover, it is more sensitive to the non-sinusoidal pulse shape characteristics of pulsars. Therefore the epoch folding technique is preferred for its simplicity and superiority.

Another test known as the Rayleigh test (Gibson et al. 1982) has been used to search for the presence of periodic pulsations in a series of photon arrival times. If the data were that of accreting, pulsing X-ray sources then this would have been the more appropriate test; as the Rayleigh test is more sensitive for searches for the broad, relatively smooth pulses characteristic of pulsing X-ray sources. The epoch folding technique, on the other hand, is more sensitive to the narrow pulses (relatively sharp peaks in the light curve) characteristic of radio pulsars. A fuller comparisons of these techniques are given in Leahy et al. (1983a, b).

5.2.4 Emission Models -

The pulsed emission from the Crab pulsar (PSRØ531+21) is unique among the known pulsars for its existence at almost all the frequencies of the electromagnetic spectrum. The doublely-peaked structure of the light curves observed from radio to high-energy gammma-rays is phase-aligned, but the two peaks vary in relative intensity, height and width at various energies.

The detailed structure of the emission region for the Crab pulsed radiation must be determined from intricate models, the general geometry of the emission region can be deduced from the gross behaviour of the light curve. The Crab peaks have widths of 15° and are separated by Ø.4 of the period. The form of the emission pattern is unknown, but beams originating near the magnetic polar caps (at $< Ø.1\ R_L$), hollow cones of emission hugging the last open field lines or beams from the radiation pattern of relativistic particles have been suggested. The intrinsic angular size of each of these is $< 1Ø^{\circ}$. It is plausible that the peaks could be produced by two peaks of such an emission pattern if the observer's line of sight was near the equatorial plane.

Although, four different families of model have been discussed in chapter 1 which tried to explain the emission mechanisms of pulsars. As has already been said, at the present time there is no single model that can fully explain the emission mechanisms. On a whole, most models can only

partially fulfil the criteria for emitting radiation from pulsars. However, there seems to be a general agreement on the basic energy source and timing mechanism for pulsars, but as yet no such agreement upon the detailed process which account for the observed properties. Future development in modelling can be most conveniently achieved from numerical simulation using computers. By combining the four families of model into one, it may be possible to obtain a more consistent model.

5.3 Sources Of Errors

The line feature search depend on two important criteria: (i) how the acceptance angle is defined and (ii) how the confidence level is calculated. Variation of the acceptance angle changes the periods of 'time on' and 'time off' and consequently changes the significance of the results. If one does not know in which energy interval a line is expected, the number of degrees of freedom associated with the search will be large and the confidence level significantly reduced. Alternatively, one may argue that the search should not have taken account of any known results if one is to produce an independent measurement. But the argument can be made that the search was specially designed to confirm results already known.

For the temporal analysis, errors due to event timing are negligible compared to the errors introduced by the corrections on event arrival times. The uncertainty in the

position of the barycentre can at most contribute a small systematic error which does not affect the calculations. It is fortunate that the present experimental observation period is only a few hours, because as a consequence errors due to long term causes, such as gravitational red shift and gravitational path delay offset, can be disregarded.

5.4 Conclusions

The observation of gamma-ray lines from processes of nucleosynthesis in supernovae and novae since the beginning of gamma-ray astronomy, has been adversely affected by the poor instrumental angular resolution and the low counting statistics. The only clearcut criterion remains the time structure of the detected signal. One is often limited to checking the signal for the period of a known radio pulsar lying within the acceptance cone. The low statistics available and the long observation time required make the pulsar search in the gamma-ray energy range critically dependent on the precise knowledge of the period and period derivative of the source at the epoch of observation. An analysis based on a scanning in P and $\dot{P}$, around approximate input values derived from radio data obtained at a close epoch is necessary.

A "gamma-ray pulsar search" cannot simply be dependent upon a simple single χ^2 test on a light curve obtained by folding event arrival times with extrapolated, or even contemporary, radio values of P and $\dot{P}$. Conclusions claiming

a "positive" result, need to be supported by the coherent behaviour of parameters ranging from the structure of the χ^2 curve as a function of the scanning steps in P and $\dot{P}$, its dependence from the acceptance angle at different energies, to the significance of the resulting χ^2 curve characteristic of a point source.

The main objective of this thesis has been to present the results of a search for gamma-ray periodic pulsed emission from the Crab pulsar. The search was successful, the period of the Crab pulsar was accurately determined and the light curve deconvolved. Also presented are the three gamma-ray line features from the Crab Nebula region observed by the Durham experiment. The observation of the Crab on June 6th 1981 has produced evidence for three gamma-ray line features, at 78.9 keV, 404.4 keV and 1049.6 keV. One of the line feature at 78.9 keV is seen only as a transient effect appearing in the final period of the observation on the Crab. But positive conclusions could not be drawn as the observation finished before the overall shape of the feature was seen. It might be possible that this feature was observed before it reached peak intensity. The 404.4 keV line feature provides confirmation of earlier results of other experimental groups. The line at 1049.6 keV has not been seen before and awaits confirmation. The temporal analysis of the Crab pulsar has failed to produce evidence that these lines pulse with the pulsar frequency.

The interpretation of results in this or other low-energy gamma-ray spectrometer experiments is somewhat limited by statistics. Obviously, life would have been much simpler if one could obtain results in a sufficiently large quantity and as Rutherford once said, "If your experiment needs statistics, you ought to have done a better experiment". However, had he been aware of the cost of such improvement, he might have thought otherwise. A significant increase in both exposure times and sensitivity is needed to detect the numerous weak gamma-ray lines that so far have escaped detection. Balloon-borne detectors have made pioneering observations in gamma-ray astronomy, but future progress will only be possible if additional flight opportunities are made available by instruments that are both more sensitive and have a greater resolving power than those flown so far. No doubt, future development in the field of low-energy gamma-ray astronomy will open up a new horizon to our understanding of this ever evolving Universe.

ACKNOWLEDGEMENTS

I would like to thank Professors A. W. Wolfendale and B. H. Bransden for allowing me to use the facilities of the Department. I am very grateful to my supervisor Dr M. G. Thompson for giving me the opportunity to work in the Low-energy Gamma-ray Experimental Group and providing continuous supervision throughout the year. I am greatly indebted to my colleague Mr R. M. Myers for all his help, ranging from programming advice, ideas, reading drafts and much more. I would also like to thank the following for their valuable help:

Dr C. A. Ayre for many helpful suggestions and discussions.

Dr F. R. Stephenson for reading a few sections of the draft and constant encouragement.

Mrs P. A. Russell for helping with some of the diagrams.

Mr A. P. Lotts for advices on computing.

Mr M. D. Mannion for collecting and filing the references.

Mr C. D. H. Williams for correcting a few sentences.

Lastly, I would like to thank all those who have directly or indirectly participated in the Durham MK1B Spectrometer experiment.

REFERENCES

"Astronomical Almanac", 1981, HMSO, London.

Aysali, S. and Ogelman, H., 1980, Ap.J., 237, 227-235.

Aysali, S., Ap.J., 1981, 249, 698-703.

Baker, R.M.L.,Jr. and Makemson, W., 1960, "An Introduction to Astrodynamics", Academic Press, New York and London.

Baker, R.E., Lovett, R.R., Orford, K.J., and Ramsden, D., 1973, Nature Phy.Sci., 245, 18-19.

Bennett, K. et al., 1977, Astron. Astrophys., 61, 279.

Bolt, E.A., Holt, S.S. and Serlemitsos, 1971, Ap.J., 164, L9-L13.

Buccheri, R., D'Amico, N., Scarsi, L., Kanbach, G. and Masnou, J.L., 1977, Proc. 12th ESLAB Symp. ESA SP-124, 309-316.

Carpenter, G.F., Coe, M.J. and Engel, A.R., 1976, Nature, 259, 99.

Cheng, A.F. and Ruderman, M.A., 1977, Ap.J., 216, 865-872.

Cherry, M.L., Chupp, E.L., Dunphy, P.P., Forrest, D.J. and Ryan, J.M., 1980, Ap.J., 242, 1257.

Cocke, W.J., Disney, M.J. and Taylor, D.J., 1969, Nature, 221, 525.

Cowsik, R. and Wills, R.D., 1980, "Non-Solar Gamma-Rays" (COSPAR), Pergamon Press, Oxford and New York.

Dolan, J.F., Crannell, C.J., Dennis, B.R., Frost, K.J., Maurer, G.S. and Orwig, L.E., 1977, Ap.J., 217, 809-14.

Elitzur, M., 1979, Ap.J., 229, 742-746.

Fawley, W.M., Arons, J. and Scharlemann, E.T., 1977, Ap.J., 217, 227-243.

Fishman, G.J., Harnden, F.R. and Haymes, R.C., 1969, Ap.J. Lett., 156, L107.

Floyd, F.W., Glass, I.S. and Schnopper, H.W., 1969, Nature, 224, 50-51.

Fritz, G., Henry, R.C., Meekins, J.F., Chubb, T.A. and Friedman, H., 1969, Science, 164, 709-711.

Gibson, A.I., Harrison, A.B., Kirkman, I.W., Lotts, A.P., Macrae, J.H., Orford, K.J., Turver, K.E. and Walmsley, M., 1982, Nature, 296, 833-835.

Goldreich, P. and Julian, W.H., 1969, Ap.J., 157, 869.

Graser, U. and Schonfelder, V., 1982, Ap.J., 263, 677-689.

Gruber, D.E. and Ling, J.C., 1977, Ap.J., 213, 802-14

Gullahorn, G.T., Isaacman, R., Rankin, J.M. and Payne, R.R., 1977, Astron.Astrophys.J., 82, 309-312.

Hameury, J.M., Boclet, D., Durouchoux, PH., Cline, T.L., Paciesas, W.S., Teegarden, B.J., Tueller, J. and Haymes, R.C., 1983, Ap.J., 270, 144.

Hardee, P.E., 1979, Ap.J., 227, 958-973.

Harding, A.K., Tademaru, E., and Esposito, L., 1978, Ap.J., 225, 226-236.

Harding, A.K., 1981, Ap.J., 245, 267-273.

Hearn, D., 1969, Nucl.Instr.Methods., 70, 200.

Henriksen, R.N. and Norton, J.A., 1975, Ap.J., 201, 719.

Hewish, A., Bell, S.J., Pilkington, J.D.H., Scott, P.F. and

Collins, R.A., 1968, Nature, 217, 709.

Hillier, R.R., Jackson, W.R., Murray, A., Redfern, R.M., and Sale, R.J., 1970, Ap.J.Lett., 162, L177.

Jacobson, A.S., Ling, J.C., Mahoney, W.A. and Willett, J.B., 1978, 'Gamma Ray Spectroscopy in Astrophys', ed. T.L. Cline and R. Ramaty, NASA Pub. 79619, 228-251.

Kniffen, D.A., et al., 1974, Nature, 251, 397.

Knight, F.K., 1981, PhD Thesis, " X-ray and Gamma-ray Observations of Pulsed Emission from Radio Pulsars", University of California, San Diego.

Knight, F.K., 1982, Ap.J., 260, 538.

Kundt, W. and Krotscheck, E., 1980, Astron.Astrophys., 83, 1-21.

Kurfess, J.D., 1971, Ap.J. Lett., 168, L39-42.

Laros, J.G., Matteson, J.L. and Pelling, R.M., 1973, Nature Phys. Sci., 246, 109-111.

Leahy, D.A., Darbro, W., Elsner, R.F. and Weisskopf M.C., 1983a, Ap.J., 266, 160-170.

Leahy, D.A., Elsner, R.F. and Weisskopf M.C., 1983b, Ap.J., 272, 256-258.

Leventhal, M., MacCallum, C. and Watts, A., 1977, Ap.J., 216, 491-502.

Li, T.P. and Ma, Y.Q., 1983, Ap.J., 272, 317-324.

Ling, J.C., Mahoney, W.A., Willett, J.B. and Jacobson, A.S., 1977, Nature, 270, 36.

Ling, J.C., Mahoney, W.A., Willett, J.B. and Jacobson, A.S., 1979, Ap.J., 231, 896.

Lingenfelter, R.E., Higdon, J.C. and Ramaty, R., 1978, "Gamma-ray Spectroscopy in Astrophysics", ed. T.L. Cline, R. Ramaty, p252, Greenbelt, Md:Goddard NASA.

Manchanda, R.K., Bazzano, A., La Padula, C.D., Polcaro, V.F. and Ubertini, P., 1982, Ap.J., 252, 172.

Manchester, R.N., 1971, Ap.J. Lett., 163, L61.

Manchester, R.N. and Taylor, J.H., 1977, "Pulsars", W.H.Freeman and Company, San Francisco.

Michel, F.C., 1973a, Ap.J., 180, 207.

Michel, F.C., 1973b, Ap.J. Lett., 180, L133.

Minkowski, R., 1968, "Nonthermal Galactic Radio Sources, Stars and Stellar Systems", 8. Edited by B.M. Middlehurst and L.H. Aller, University of Chicago Press, Chicago.

O'Mongain, E., 1973, Nature, 241, 376.

Oppenheimer, J.R. and Volkoff, G., 1939, Phys. Rev., 55, 374.

Orwig, L.E., Chupp, E.L. and Forrest, D.J., 1971, Nature Phys.Sci., 231, 171.

Pacini, F., 1967, Nature, 216, 567.

Pandharipande, V.R., Pines, D. and Smith, R.A., 1976, Ap.J., 208, 550.

Pearson, E.S. and Hartley, H.O., 1958, "Biometrika Tables for Statisticians Vol 1", Cambridge University Press.

Penningsfeld, F.P., Graml, U. and Schonfelder, V., 1979, Proc. 16th Internat. Cosmic Ray Conf., Kyoto, 1, 101.

Rhoades, C.E. and Ruffini, R., 1974, Phys. Rev. Lett., 32, 324.

Ruderman, M.A. and Sutherland, P.G., 1973, Nature Phys.Sci., 246, 93.

Ruderman, M.A. and Sutherland, P.G., 1975, Ap.J., 196, 51-72.

Ryckman, S.G., Ricker, G.R., Scheepmaker, A., Ballintine, J.E., Doty, J.P., Downey, R.M. and Lewin, W.H.G., 1977, Nature, 266, 431-433.

Schonfelder, V., Lichti, G., and Moyano, C., 1975, Nature, 257, 375.

Smith, F.G., 1977, "Pulsars", Cambridge University Press.

Staelin, D.H. and Reifenstein, E.C., 1968, Science, 162, 1481.

Strickman, M.S., Kurfess, J.D. and Johnson, W.N., 1982, Ap.J. Lett., 253, L23.

Stumpff, P., 1979, Astron. Astrophys., 78, 229-238.

Stumpff, P., 1980, Astron. Astrophys. Suppl. Ser., 41, 1-8.

Sturrock, P.A., 1971, Ap.J., 164, 529-556.

Teegarden, B.J. and Cline, T.L., 1980, Ap.J. Lett., 236, L67.

Walraven, G.D., Hall, R.D., Meegan, C.A., Coleman, P.G., Shelton, D.H. and Haymes, R.C., 1975, Ap.J., 202, 502.

Warner, B., Nather, R.E. and MacFarlane, M., 1969, Nature, 222, 233.

Wheeler, J.A., 1966, Ann. Rev. Astron. Astrophys., 4, 393.

White, et al., 1980, Nature, 284, 608.

Wills, R.D., Bennett, K., Bignami, G.F., Buccheri, R.,

Caraveo, P.A., Hermsen, W., Kanbach, G., Masnou, J.L., Mayer-Hasselwander, H.A., Paul, J.A., Sacco, B., 1982, Nature, 296, 723-726.

Wilson, R.B., Dayton, B., Moon, S.H., Ryan, J.M., Zych, A.D. and White, R.S., 1977, Proc.15th Internat.Cosmic Ray Conf., Plovdiv, 1, 24.

Yoshimori et al., 1979, Aust.J. Phys., 32, 375-382.